7-1-1999

Design of High Strength Spiral Reinforcement for Prestressed Concrete Piles

Stephen P. Pessiki

Michael Mudlock

LEHIGH
University

DESIGN OF HIGH STRENGTH SPIRAL REINFORCEMENT FOR PRESTRESSED CONCRETE PILES

by

Michael Mudlock

Stephen Pessiki

ATLSS Report No. 99-12

July 1999

ATLSS is a National Center for Engineering Research on Advanced Technology for Large Structural Systems

117 ATLSS Drive
Bethlehem, PA 18015-4729

Phone: (610)758-3525
Fax: (610)758-5553

www.lehigh.edu/~inatl/inatl.html
Email: inatl@lehigh.edu

DESIGN OF HIGH STRENGTH SPIRAL REINFORCEMENT FOR PRESTRESSED CONCRETE PILES

by

Michael Mudlock
Graduate Research Assistant
Civil and Evironmental Engineering

Stephen Pessiki
Associate Professor
Civil and Environmental Engineering

ATLSS Report No. 99-12

July 1999

ATLSS is a National Center for Engineering Research on Advanced Technology for Large Structural Systems

117 ATLSS Drive
Bethlehem, PA 18015-4729

Phone: (610)758-3525
Fax: (610)758-5553

www.lehigh.edu/~inatl/inatl.html
Email: inatl@lehigh.edu

ACKNOWLEDGMENTS

The following organizations and companies provided financial and/or material support for this research: Precast / Prestressed Concrete Institute, Concrete Technology Corporation, Sumiden Wire Products Corporation, Florida Wire and Cable, Inc., and Neturen Co., Ltd. Support from the sponsors is gratefully acknowledged. The findings and conclusions presented in this report are those of the authors, and do not necessarily reflect the views of the sponsors.

TABLE OF CONTENTS

LIST OF TABLES

LIST OF FIGURES

CHAPTER 4

CHAPTER 5

ABSTRACT

The use of high strength spiral reinforcement in prestressed concrete piles enables a reduction in the amount of spiral steel required and eases congestion problems during fabrication and concrete placement. However, current code provisions limit the nominal yield stress of the spiral reinforcement to 60 ksi (414 MPa). A procedure for the design of high strength spiral reinforcement for prestressed concrete piles, which utilizes useable stress values, rather than nominal yield stress values, is evaluated in this research.

This research included large-scale axial load tests on six spirally reinforced concrete piles, along with experimental and analytical investigations of the spiral reinforcement properties. The test matrix included six steels of different yield and useable stresses, all in excess of 60 ksi (414 MPa). Useable stress values ranged from 79 ksi (545 MPa) to 164 ksi (1131 MPa).

It was found that, for the pile geometry and material properties treated in this study, the proposed design procedure satisfactorily predicted the behavior of the piles made from spirals with useable stress values up to 110 ksi (758 MPa). However, the design procedure failed to predict the behavior of the piles made with spirals with higher useable stresses. For these piles, the concrete core did not achieve its desired strength. This may be due to a number of factors, including the difference in tensile stress-strain behavior between unspiraled and spiraled wires, the stiffness of the spirals, and the variability of spiral confinement.

CHAPTER 1
INTRODUCTION

1.1 INTRODUCTION

Transverse reinforcement is used in concrete compression members to create a state of triaxial compression in the confined concrete core by restraining the transverse expansion of the core as the member is compressed axially. The use of continuous lateral reinforcement, such as spirals, has proven to be very effective in increasing both the strength and deformation capacity of the concrete.

In current U. S. practice, the required amount of spiral reinforcement is based in part upon the concrete compressive strength. Basically, spiral reinforcement is designed so that, should the pile be overloaded, the spirals would provide enough strength enhancement to the concrete core to replace the strength lost by the spalling of the concrete cover. For a given pile cross-section, a higher strength concrete requires a greater volume of spiral reinforcement. As concrete strengths have increased over the years, the quantity of required spiral reinforcement has also increased. To satisfy the need for a greater amount of spiral reinforcement, either the use of larger diameter spiral wires or decreased pitch can be employed. However, fabrication problems based on practical spacing and code requirements may result.

One alternative to the above practices would be to use higher strength spiral reinforcement. In theory, a smaller proportion of higher strength spiral steel could be utilized to provide a given required amount of confining pressure to the concrete. Currently, code provisions do not permit spiral reinforcement with yield strengths in excess of 60 ksi (414 MPa).

Graybeal and Pessiki (1998) have proposed that higher strength steel could be effectively used as spiral reinforcement in concrete piles. In that work, a new design approach which would permit spiral stresses in excess of 60 ksi (414 MPa) was proposed. In short, according to the proposed design procedure, spiral reinforcement design is based upon a *useable stress* as opposed to a nominal yield. Useable stress is defined as the stress in the spiral reinforcement at the second peak in the load-shortening response of the spirally reinforced concrete piles. This second peak is the peak strength of the spirally-confined core, after the loss of the cover concrete.

1.2 OBJECTIVE

This research is a follow-up to the work conducted by Graybeal et al. on the confinement effectiveness of high strength spiral reinforcement in prestressed concrete piles. The primary objective of this research was to evaluate the validity of the design procedure proposed by Graybeal et al. for the design of spiral reinforcement for prestressed concrete piles under concentric axial compression.

1.3 SUMMARY OF APPROACH

This research included two phases of work. The first phase involved the design and testing of six 14 in. (356 mm) diameter spirally reinforced concrete piles in concentric axial compression. The

piles were designed according to the procedure proposed by Graybeal et al. Each specimen was designed using an unconfined concrete compressive strength of 8.0 ksi (55.2 MPa). The nominal yield stresses of the spiral reinforcement varied from 78 ksi (538 MPa) to 195 ksi (1345 MPa), while the useable stresses of the spiral reinforcement varied from 79 ksi (545 MPa) to 164 ksi (1131 MPa).

The second phase of this research focused on a study of the stress-strain properties of the spiral reinforcement. Tension tests were performed on unspiraled specimens of spiral reinforcement in order to obtain stress-strain relationships. Then, fiber model analyses were performed to evaluate the effects of spiraling on the tension stress-strain behavior of the spiral reinforcement.

1.4 SUMMARY OF FINDINGS

From the results of this research, it is concluded that the proposed design procedure provides satisfactory spiral designs for the piles made of the steels studied by Graybeal et al. (1998). The useable stresses of these steels ranged from 79 ksi (545 MPa) to 110 ksi (758 MPa). This conclusion is applicable to the pile geometries (i.e. including the 24 in. (610mm) diameter piles) and material strengths treated in this study and in the earlier study by Graybeal et al.

Three key relationships used in the design procedure were demonstrated to provide acceptable results for design purposes for spiral steels with useable stress values up to 110 ksi (758 MPa). First, the Richart et al. (1928, 1929, 1934) estimate of longitudinal strain (Equation 2.9) provides reasonable to conservative estimates of longitudinal strain at Δ_2, with the more conservative estimates made for the higher useable stress spirals. Second, the tangent dilation ratio relationship proposed by Graybeal et al. (Equation 2.10) was found to slightly underestimate the value of transverse strain at peak concrete core strength. The result of these first two relationships is that the proposed design procedure provides conservative estimates of the strains and stresses in the spiral reinforcement at Δ_2, and thus conservative estimates of the confining stress on the core concrete at Δ_2. Finally, the Richart et al. estimate of increase in concrete core strength due to spiral confinement (Equation 6.7) was found to be valid for the piles made with useable stress values up to 110 ksi (758 MPa). Further research is needed to fully explain the behavior of Specimens 14-E' and 14-F', where the observed increases in core strength were below the strength increases that were expected based on the level of lateral confining pressure that was developed. This future work may focus on the role of spiral stiffness and variable confining pressures throughout the response of a pile on the resulting strength enhancement of the concrete core.

The results of the fiber model study of the effects of the spiraling process on the two wires with the highest strengths (E', F') show that a rounding or softening of the original unspiraled tensile stress-strain curve takes place, producing a curve that provides lower values of stress for given values of strain up to full yielding of the wire cross-section. Designing spirals based on the unspiraled stress-strain curve as opposed to the in-situ stress-strain curve overestimates the actual useable stress and can lead to an unconservative design for the pile. Given that this situation exists, further research is needed to quantify the effect of the spiraling process on the in-situ stress-strain behavior of high strength spiral reinforcement.

1.5 OUTLINE OF REPORT

The remainder of this report is separated into five chapters. Chapter 2 presents relevant background information, including the design procedure by developed by Graybeal et al., which was the focus of this research. Chapter 3 describes the experimental program, which includes the test matrix, specimen details, and material properties. The experimental results are presented in Chapter 4. Chapter 5 discusses the findings of the fiber model analyses conducted on the high strength spiral wires. Chapter 6 contains a detailed analysis of the experimental results, including discussions of spiral behavior and concrete core behavior, and an evaluation of the design procedure. Finally, Chapter 7 presents the conclusions of this research along with several recommendations for future research.

1.6 NOTATION

The following notation is used in this report:

$A_{c,o\text{-}o}$ = core concrete area of pile measured to outside diameter of spiral
$A_{c,total}$ = total cross-sectional area of concrete in the pile
A_g = gross cross-sectional area of pile
A_{lg} = total area of longitudinal reinforcement
A_{sp} = total cross-sectional area of bundled spiral wires
$A_{\eta tan2}$ = area under the tangent dilation ratio curve between $\epsilon_c = 0$ and ϵ_{c2}
$\bar{A}_{\eta_{tan2}}$ = area under the tangent dilation ratio curve between normalized values of $\epsilon_c = 0$ and ϵ_{c2}
d_{sp} = diameter of spiral measured out-to-out of wire
d_{sw} = diameter of an individual spiral wire
f_2 = lateral confining stress exerted on confined concrete
$f_{2\text{-}1}$ = lateral confining stress exerted on confined concrete at Δ_1
$f_{2\text{-}2}$ = lateral confining stress exerted on confined concrete at Δ_2
$f_{2\text{-}c}$ = lateral confining stress exerted on confined concrete at the confined concrete peak strength
$f_{2\text{-}spall}$ = lateral confining stress exerted on confined concrete at Δ_{spall}
f_c = axial compressive stress in concrete
f_c' = compressive strength of prepared cylinders
f_{c1} = compressive strength of confined concrete at Δ_1
f_{c2} = compressive strength of confined concrete at Δ_2
f_{cc} = peak confined concrete compressive strength
f_{co} = compressive strength of unconfined concrete
f_{lg} = stress in longitudinal reinforcement
f_{ly} = yield stress of longitudinal reinforcement
f_{pc} = concrete compressive stress due to effective prestress
f_{sp} = stress in the spiral reinforcement
$f_{sp,spall}$ = stress in the spiral reinforcement at Δ_{spall}
f_{sp1} = stress in the spiral reinforcement at Δ_1
f_{sp2} = stress in the spiral reinforcement at Δ_2

f_{su} = ultimate strength of spiral reinforcement

f_{sy} = yield stress of spiral reinforcement

$f_{sy,nom}$ = nominal yield stress of spiral reinforcement as reported by spiral manufacturer

f_y = yield stress of reinforcement

m = ϵ_{c2} normalized by ϵ_{co}

n_{fibers} = number of fibers in fiber model of wire cross-section

n_{lg} = number of longitudinal reinforcing bars in section

n_{sp} = number of spiral wires bundled to form a single turn of spiral

P = load on pile

P_1 = load on pile just prior to cover spalling

P_2 = load on pile at Δ_2

P_{drop} = load on pile immediately after ΔP_{drop}

$P_{failure}$ = load on pile at failure

P_o = nominal pile capacity

P_{spall} = lowest load on pile between Δ_1 and Δ_2

$R(f_{sp2})_{exp/dsgn}$ = ratio of experimental to design spiral stress at Δ_2

$R_{fsp2/fsy,nom}$ = ratio of spiral stress at Δ_2 to nominal design spiral yield stress

$R(\Delta f_{c12})_{exp/dsgn}$ = ratio of experimental to design increase in concrete stress from Δ_1 to Δ_2

$R(\Delta f_{c12})_{exp/rich}$ = ratio of experimental to Richart et al. predicted increase in concrete stress from Δ_1 to Δ_2

$R(\epsilon_{c2})_{exp/cus}$ = ratio of experimental to Cusson and Paultre predicted longitudinal strain at Δ_2

$R(\epsilon_{c2})_{exp/dsgn}$ = ratio of experimental to design value of longitudinal strain at Δ_2

$R(\epsilon_{c2})_{exp/rich}$ = ratio of experimental to Richart et al. predicted longitudinal strain at Δ_2

$R(\rho_{sp})_{nom/60}$ = ratio of volumetric ratio from nominal design yield stress to volumetric ratio from 60 ksi (414 MPa) yield stress spiral steel

$R(\rho_{sp})_{redesign/60}$ = ratio of volumetric ratio from redesign f_{sp2} to volumetric ratio from 60 ksi (414 MPa) yield stress spiral steel

s = spiral pitch

α = percentage of ϵ_{co} at which tangent dilation ratio beings to increase

β = percentage of ϵ_{c2} at which tangent dilation ratio stops increasing

Δf_{c12} = change in confined core stress between Δ_1 and Δ_2

Δ_1 = pile axial shortening corresponding to P_1

Δ_2 = pile axial shortening corresponding to P_2

Δ_{spall} = pile axial shortening corresponding to P_{spall}

$\Delta_{failure}$ = pile axial shortening corresponding to $P_{failure}$

ϵ_c = axial strain in concrete

ϵ_{c1} = axial strain in concrete corresponding to f_{c1}

ϵ_{c2} = axial strain in concrete corresponding to f_{c2}

ϵ_{cc} = axial strain in concrete corresponding to f_{cc}

ϵ_{co} = axial strain in concrete corresponding to f_{co}

ϵ_{ct} = transverse strain in the concrete core

ϵ_{ct2} = transverse strain in concrete core at Δ_2
ϵ_{ly} = strain in longitudinal reinforcement at f_{ly}
ϵ_{sp} = strain in the spiral reinforcement
ϵ_{sp1} = strain in the spiral reinforcement at Δ_1
$\epsilon_{sp,spall}$ = strain in the spiral reinforcement at Δ_{spall}
ϵ_{sp2} = strain in the spiral reinforcement at Δ_2
$\epsilon_{sp2,dsgn}$ = design value of strain in the spiral reinforcement at Δ_2
ϵ_{su} = strain in the spiral reinforcement corresponding to f_{su}
ϵ_y = strain in reinforcement corresponding to f_y
η_{sec} = secant dilation ratio
η_{sec2} = secant dilation ratio at Δ_2
η_{tan} = tangent dilation ratio
$\eta_{tan,ini}$ = proposed initial tangent dilation ratio
$\eta_{tan,lim}$ = proposed limiting tangent dilation ratio
ρ_{lg} = longitudinal reinforcement ratio, computed as the ratio of the area of longitudinal reinforcement to the total area of concrete in section ($A_{c,total}$)
ρ_{sp} = volumetric steel ratio, computed as the ratio of the volume of spiral reinforcement to total volume of the core ($A_{c,o-o}$)

1.7 UNIT CONVERSION FACTORS

The following unit conversions are used in this report:

1 in. = 25.4 mm
1 in.^{2} = 645 mm^2
1 kip = 4.448 kN
1 ksi = 6.895 MPa
1 ft^3 = 0.02837 m^3

CHAPTER 2
BACKGROUND

2.1 INTRODUCTION

This chapter presents background information relevant to this research. Section 2.2 reviews current design code requirements for spirally reinforced compression members. Section 2.3 presents a comprehensive review of the work conducted by Graybeal et al. (1998) and the major results that were obtained. Included in this section is a summary of the experimental tests and analytical studies that were performed. The major findings of the work are discussed. Also presented is a description of the proposed design procedure for high strength spiral reinforcement in prestressed concrete piles developed by Graybeal et al. A brief discussion is given of the stress-strain properties of spiral steel obtained through a fiber model study. Finally, a description is given of the proposed tangent dilation ratio relationship, which is a key element in the proposed design procedure.

The reader is assumed to have an understanding of the basic behavior of spirally reinforced concrete piles under concentric axial load. A brief discussion can be found in Graybeal et al., as well as in many of the references cited in this report.

Figure 2.1 illustrates the basic behavior of spirally reinforced concrete piles under concentric axial compression. Included in this figure is notation that will be used throughout the remainder of the text. All notation pertaining to the figure has been previously defined in Section 1.6.

2.2 DESIGN CODE REQUIREMENTS

Currently, there are two documents which govern the design of spirally reinforced columns and piles. They are: (1) the ACI 318 Building Code Requirements for Structural Concrete (1995) (hereafter referred to as the ACI 318 Code); and, (2) the American Association of State Highway and Transportation Officials LRFD Bridge Design Specifications (1994) (hereafter referred to as the AASHTO Design Specifications). Furthermore, the Precast/Prestressed Concrete Institute Design Handbook (1992) (hereafter referred to as the PCI Handbook) outlines provisions for the design of prestressed piles.

The ACI 318 Code and the AASHTO Design Specifications both state the nominal concentric axial load capacity, P_o, of an axially load non-prestressed member is given by

$$P_o = 0.85f_{co}\left(A_g - A_{lg}\right) + f_{ly}A_{lg} \tag{2.1}$$

where A_g is the gross cross-sectional area of the pile, A_{lg} is the area of longitudinal reinforcement, and f_{ly} is the yield stress of the longitudinal reinforcement. The PCI Handbook gives a similar equation, except that it takes into account the prestress force present within a prestressed member through the equation

$$P_o = \left(0.85f_{co} - 0.60f_{pc}\right)A_{c,total} \tag{2.2}$$

where f_{pc} is the concrete compressive stress due to effective prestress and $A_{c,total}$ is the total area of concrete in the cross-section. The PCI Handbook assumes the prestressed pile contains no non-prestressed longitudinal reinforcement. Therefore those terms relating to the longitudinal reinforcement do not appear in the equation.

For general design purposes, the ACI 318 Code includes a strength reduction factor of $\varphi = 0.85$ for nonprestressed spirally reinforced compression members to account for small eccentricities. A reduction factor of $\alpha = 0.75$ is also applied to account for member behavior and criticality to the structural system. The PCI Handbook takes a different approach. A safety factor is applied to the nominal strength capacity given by Equation 2.2. Equation 2.3 expresses this safety factor as

$$N = \left(0.33f_{co} - 0.27f_{pc}\right)A_{c,total} \tag{2.3}$$

where N is the safety factor. The PCI Handbook suggests that a safety factor between 2.0 and 3.0 is usually adequate.

A pile is defined as any axially loaded member embedded in the ground and has sufficient lateral pressure surrounding it throughout its length to prevent lateral buckling from occurring. If sufficient lateral ground pressure can be assured at all times, then the member can be designed as a pile as defined by the AASHTO Design Specification and the PCI Handbook. From observation of Equation 2.2, the equation given by the PCI Handbook shows that the quantity of spiral reinforcement required is based solely on the position of the spiral within the length of the pile and is not dependent on the concrete cover, the strength of the reinforcement, or the strength of the concrete.

Members which serve as piles but do not completely comply with the definition of piles as stated above, are to be designed through the specifications for non-pile compression members. A primary reason for doing this is because it is difficult to assure that there will be sufficient surrounding ground pressure to prevent lateral buckling throughout the entire height of the pile. Also, piles often protrude from the ground and thus are required to be designed as columns.

As a spirally reinforced pile is compressed axially, the concrete core expands laterally due to the Poisson effect. As a result of the core expansion, a lateral pressure is exerted by the core concrete on the spiral reinforcement, resulting in hoop tension in the spiral steel. In maintaining force equilibrium, a confining pressure (compressive force) is applied to the concrete core by the spirals, which serve to reduce the lateral expansion and increase the strength of the concrete core. This confining pressure can be calculated from Equation 2.4.

$$f_2 = \tfrac{1}{2}\rho_{sp} f_{sp} \tag{2.4}$$

This equation is derived from statics considering a free body diagram of a section of the core concrete. The volumetric ratio of spiral reinforcement is denoted by ρ_{sp}. f_{sp} is the stress in the spiral reinforcement.

The volumetric ratio of spiral steel required to provide sufficient confinement for the core concrete in a non-pile member is given as

$$\rho_{sp} \geq 0.45\left(\frac{A_g}{A_{c,o-o}} - 1\right)\left(\frac{f_{co}}{f_{sy}}\right) \tag{2.5}$$

where $A_{c,o-o}$ is the area of core concrete, measured to the outside diameter of the spiral, and f_{sy} is the yield stress of the spiral reinforcement. This equation is based on the objective that the load-carrying capacity which was lost by spalling of the concrete cover should be replaced by increased load-carrying capacity of the concrete core. In this formulation, the spiral reinforcing steel is assumed to reach its yield stress. As noted earlier, in current practice, there is an upper limit of f_{sy} = 60 ksi (414 MPa) placed on the yield stress of the spiral reinforcement. Through this means, the volumetric ratio of transverse reinforcement remains high and the confining pressure at the second peak is very likely at or above the expected level.

The volumetric ratio of spiral reinforcement in a pile is computed through the use of Equation 2.6,

$$\rho_{sp} = \frac{4A_{sp}}{d_{sp}s} \tag{2.6}$$

where d_{sp} denotes the out-to-out diameter of the spiral reinforcement, and A_{sp} is the cross-sectional area of the spiral wire.

There are also provisions in the design codes relating to the spiral reinforcement bar size, the clear spacing between bars, the cover concrete required, splicing of spiral wires, as well as the required amount of longitudinal reinforcement. The purpose of the bar size and clear spacing requirements is to ensure that the confining pressure will be distributed throughout the height of the member without hampering the placement of concrete within the formwork. For example, the ACI 318 Code specifies that the minimum bar size is a #3 bar (0.375 in. (9.53 mm) diameter), the minimum clear spacing between bars is the larger of 1 in. (25.4 mm) or 4/3 times the largest aggregate size, and the maximum clear spacing between bars is 3 in. (76.2 mm). The AASHTO Design Specification contains similar requirements.

The clear cover requirements for concrete compression members are clearly defined in both the ACI 318 Code and the AASHTO Design Specification. In general, for piles, the clear cover is to be 2 in. (50.8 mm) due to direct contact between the member and the earth. However, in special cases such as exposure to harsh environment, a cover of 3 in. (76.2 mm) may be specified. Additionally, prestressed members cast under factory controlled conditions are sometimes allowed reductions in the amount of cover required.

2.3 SUMMARY OF WORK OF GRAYBEAL ET AL.

As noted earlier, this research is based in large part on previous research at Lehigh University by Graybeal et al. Therefore, a brief discussion of that earlier work is provided below. Section 2.3.1

describes the objective of the work of Graybeal et al. and the approach taken in their research. Section 2.3.2 presents the major findings of their study. The proposed design procedure for high strength spiral reinforcement in prestressed concrete piles is presented and explained in Section 2.3.3. Section 2.3.4 discusses the fiber model study conducted by Graybeal et al. to investigate the effects of the spiraling process on the stress-strain behavior of spiral wires. Finally, Section 2.3.5 describes the dilation ratio model developed by Graybeal et al. which provides a means to relate the transverse and longitudinal strains present in a spirally reinforced pile at various stages of loading.

2.3.1 Overview of the Work Conducted by Graybeal et al.

The objective of the work of Graybeal et al. was to evaluate the confinement effectiveness of high strength spiral reinforcement in precast, prestressed concrete piles. The research included large-scale axial load tests of high strength spirally reinforced concrete piles, an experimental and analytical investigation of the properties of the spiral reinforcement, and the development of a proposed method for the design of high strength spiral reinforcement in piles.

Eight spirally reinforced specimens were tested in concentric axial compression in a 5000 kip (22.2 MN) capacity universal testing machine. Table 2.1 presents the design parameters for the work conducted by Graybeal et al. The test matrix was assembled to study the effects of pile diameter and nominal spiral yield stress on the performance of the member under concentric axial compression.

Two different diameter piles, 14 in. (356 mm) and 24 in. (610 mm), were tested. Each pile had a 4-to-1 height-to-diameter ratio, as well as a 2 in. (50.8 mm) concrete cover. A concrete strength of 8.0 ksi (55.2 MPa) was used in the design of each pile specimen. The nominal yield stress values of the spiral steels (78, 107, 121, and 140 ksi), (538, 738, 834, and 965 MPa), were denoted A, B, C, and D, respectively. In design and fabrication of the piles, additional spiral confinement was provided within one diameter of height from each end. This was done to ensure failure in the middle half of the specimen height, also referred to as the test region.

The spiral reinforcement for the test regions of the pile specimens was designed according to the equations in the ACI 318 Code and AASHTO Design Specifications with the primary exception being the limit on the yield stress of the spirals. All spiral steels exceeded the yield stress limitation of 60 ksi (414 MPa) as specified by the codes. Table 2.2 presents the details of the reinforcement used in each specimen. All spiral wires were 0.35 in. (8.89 mm) in diameter, slightly less than the code requirement of 0.375 in. (9.53 mm). In order to satisfy spiral pitch requirements in the codes and ensure adequate strength, two wires were bundled together in the test regions of the piles designed with the A and B wires. The volumetric ratio of the non-prestressed longitudinal reinforcing steel was 0.51 percent, which was below the minimum requirement of 1 percent stated in the codes. The dual purpose of the longitudinal steel in these tests was to hold the spiral wires to the correct pitch during fabrication and concrete placement and to provide a location where strain gages could be attached to monitor the axial strains in the piles during testing.

Table 2.3 presents a summary of loading and spiral stress values at key points during the testing. This data corresponds to the first peaks (P_1) in the load-shortening responses, concrete cover failures (P_{spall}), and the second peaks (P_2) in the load-shortening responses of the spirally reinforced pile specimens. Strain values were obtained from the strain gage readings, and the stress values in the spiral reinforcement as shown in the table were derived through the use of stress-strain curves from tension tests on straightened segments of spiral wires. The reasons for using these particular stress-strain curves and the validity of the final results are discussed in Section 2.3.4.

In Table 2.3, the quantity $R_{fsp2/fsy,nom}$ is the ratio of the stress in the spiral reinforcement at P_2 to the nominal yield stress of the spiral. It is noted that, with one exception, the spiral reinforcement did not reach its nominal yield stress, which was assumed would occur when designing the piles.

In none of the cases did the strength value at P_2 reach or exceed the value of P_1 (i.e. $R_{P1/P2} < 1.0$ in Table 2.3), which it should, according to the codes. It is also noted that the unconfined concrete compressive strength tested at 8.5 ksi (58.6 MPa), which was higher than the design concrete strength of 8.0 ksi (55.2 MPa). This resulted in a P_1 value that was higher than expected and in a larger loss of load-carrying capacity at cover failure. Therefore, the strength of the confined concrete core would have had to be enhanced to a greater degree than that which the spiral reinforcement was designed; thus the value of P_2 would be less than the value of P_1. However, the difference between P_1 and P_2 tended to increase as the nominal yield stress of the spiral increased, leading to the conclusion that the equations used in the design are not applicable to high strength steels.

Graybeal et al. also investigated the relationship between spiral stress and the increased strength of the concrete core. In order to evaluate this relationship, Equation 2.8 (Richart, Brandtzaeg, and Brown (1928, 1929, 1934)), was utilized. This equation is presented in Section 2.3.3. It was found that, for the most part, the observed strength enhancement of the core was consistent with the observed spiral stress.

Graybeal et al. also studied the relationship between longitudinal (axial) strain and transverse strain. The secant dilation ratio, defined as the ratio of transverse to longitudinal strain at any point in the response of the core, and the tangent dilation ratio, defined as the slope of the transverse strain versus longitudinal strain curve at any point, were evaluated. Upon comparison between experimentally determined secant and tangent dilation ratios and experimental and predicted values of transverse strain at Δ_2, it was found that the tangent dilation ratios were more consistent with the data. Therefore, a tangent dilation ratio relationship was proposed, based upon the pile behavior observed in the experimental testing as well as a knowledge of the results from previous researchers, and it is used in the proposed design procedure for high strength spiral reinforcement in concrete piles.

Along with experimental work, a fiber model analysis was performed to study the effects of the spiraling process on the mechanical properties of spiral wires. One of the wires modeled in this study was a 60 ksi (414 MPa) nominal yield stress wire with an idealized elastic-plastic stress-

strain behavior. The other wire analyzed was spiral wire D, which had a nominal yield stress value of 140 ksi (965 MPa). In order to study the effects of spiraling on the stress-strain behavior of the wires, an analysis was performed on each wire in three states: *unspiraled*, *spiraled*, and *spiraled-straightened*. For purposes of discussion, an *unspiraled* wire is a wire that has never been spiraled. A *spiraled* wire is a wire that has been bent to a certain curvature. A *spiraled-straightened* wire is a wire that has been spiraled and then straightened to its original shape. Section 2.3.4 discusses the details and findings of the fiber model study.

2.3.2 Summary of Findings by Graybeal et al.

From the experimental testing and fiber model analyses performed, Graybeal et al. formulated a number of conclusions - many of which have direct bearing on this work. While the reader is prompted to review their work to develop a clear understanding of what was accomplished, several of the major findings will be discussed below.

Graybeal et al. found that for the pile geometries and material strengths treated in their study, design procedures which limit spiral steel yield stresses to 60 ksi (414 MPa) are overly conservative. Spirally reinforced piles can be effectively designed using higher strength spiral reinforcement if they are designed according to the procedure developed by Graybeal et al., which takes into account concrete strength, pile diameter, cover distance, and the in-situ spiral stress-strain curve. Instead of using a fixed, nominal yield stress value as a design basis, a useable stress can be obtained for a specific combination of pile geometric parameters and material properties. As previously mentioned, useable stress is the stress in the spiral reinforcement at the peak core strength. Graybeal et al, suggest that the applicability of the design procedure be limited to similar pile geometries and material properties used in their study. The proposed design procedure is presented in Section 2.3.3.

Graybeal et al. concluded that a significant reduction in the volumetric spiral steel ratio is possible with the use of high strength spiral wires as opposed to 60 ksi (414 MPa) spirals. Based upon their experimental data, the researchers determined that these reductions can be achieved to a greater degree in the smaller diameter piles because their tests results showed that higher strains were realized in them, which means a greater useable stress can be mobilized in them than in the larger diameter piles.

Graybeal et al. found that for the pile geometries and material properties treated in their study, failure of each pile was precipitated by the failure of the concrete and not of the spiral reinforcement. Evidence to support this conclusion included the observation that all spiral steel strains were well below the ultimate strains for the spirals when the pile failures occurred. For the larger diameter piles, failure occurred through the formation of a well defined inclined failure plane. The angle of the failure plane from the horizontal was approximately 60 to 65 degrees in all four specimens. For the smaller diameter piles, the failure occurred through either the formation of a poorly defined inclined failure plane or through a sudden bulging failure mechanism.

From experimental tension tests, as well as fiber modeling analyses on unspiraled, spiraled-

straightened, and spiraled wires, Graybeal et al. determined that the spiraling process introduces residual stresses into the cross-section of a wire with the magnitude of residual stresses dependent on such factors as the diameter of the spiral coil, the wire diameter, and the stress-strain relationship of the wire. The residual stresses impact the proposed design of spirally reinforced piles by causing a rounding of the stress-strain curve of an unspiraled or spiraled-straightened wire. When determining the useable stress from a stress-strain curve of an unspiraled or spiraled-straightened wire, it is important to understand that, due to residual stresses, the actual stress at a particular strain may be significantly less than the value found on the curve from an unsprialed wire. Therefore, the designer may be in danger of under designing the spiral reinforcement for the pile. Further discussion of the fiber modeling is included in Section 2.3.4.

The major development by Graybeal et al. was the formulation of a proposed design procedure for high strength spiral reinforcement in prestressed concrete piles. This proposed design procedure incorporates equations developed by Richart et al. (1928, 1929, 1934) which conservatively predict the confined concrete compressive strength, f_{c2}, and the longitudinal strain at the peak compressive stress in the confined concrete ε_{c2}. Also included in the proposed design procedure is a proposed tangent dilation ratio relationship, which relates the axial strain to the transverse strain in the confined core. These relationships, as well as the use of basic mechanics principles, comprise the design procedure for high strength spiral reinforcement for prestressed concrete piles which should conservatively predict member behavior.

2.3.3 Design Procedure Proposed by Graybeal et al.

This section describes the proposed design procedure developed by Graybeal et al. for high strength spiral reinforcement in prestressed concrete piles. Each step in the procedure is explained below in sufficient detail to allow the reader to obtain a general understanding of how the procedure was developed. The design procedure is based upon a number of relationships studied by Graybeal et al., both from their experimental program and also from past research.

The proposed design procedure is outlined in Figure 2.2. Step 1 in the procedure is to determine the level of confined compressive strength which is desired for the core concrete in the pile. This is the concrete core strength at the second peak in the axial load-axial shortening response of the member, and it is denoted as f_{c2}. In the usual design of a pile (Section 2.2), this core strength is sufficient to allow the member to carry the same axial load after the loss of the concrete cover that it carried prior to concrete cover failure. Taking this approach, f_{c2} can be calculated from Equation 2.7

$$f_{c2} = \frac{f_{co} A_{c,total}}{A_{c,o-o}} \tag{2.7}$$

where f_{co} is the unconfined concrete compressive strength, $A_{c,total}$ is the total area of concrete in the cross-section, and $A_{c,o-o}$ is the area of the core concrete, measured to the outside diameter of the spiral reinforcement. While setting f_{c2} equal to this value is consistent with the ACI 318 Code and the AASHTO Design Specifications, the proposed design method does not restrict f_{c2} to be

computed in this manner. Therefore, the desired core strength can be set to any desired value.

After f_{c2} has been determined, Step 2 is to calculate the confining pressure, $f_{2\text{-}2}$, which is required in order for the core concrete to reach its desired strength. Equation 2.8 provides the means to calculate $f_{2\text{-}2}$ as follows:

$$f_{2-2} = \frac{1}{4.1}\left(f_{c2} - f_{co}\right) \tag{2.8}$$

where f_{co} is the unconfined concrete compressive strength. Richart, Brandtzaeg, and Brown (1928, 1929, 1934) developed this equation, generally seen in different form. As noted earlier, Graybeal et al. evaluated this relationship in their analysis and found it to be applicable to the piles treated in their study.

The third step in the proposed design procedure is to determine the longitudinal strain in the member at the peak core strength. This strain, denoted as ε_{c2}, is estimated through Equation 2.9.

$$\varepsilon_{c2} = \varepsilon_{co}\left(5\frac{f_{c2}}{f_{co}} - 4\right) \tag{2.9}$$

ε_{co} is the longitudinal strain at the peak strength of unconfined concrete. Richart et al. (1928, 1929, 1934) also developed this equation, which provides a conservative estimate of the longitudinal strain at the peak core strength. Richart et al. found that the presence of spiral reinforcement in an axially loaded member permitted increased concrete compressive strength and increased member ductility.

Step 4 in the proposed design procedure is to determine the transverse core concrete strain, ε_{ct2}, which occurs at the peak confined concrete compressive strength, f_{c2}. ε_{ct2} can be calculated by Equation 2.10 as follows:

$$\varepsilon_{ct2} = 0.41\varepsilon_{c2} - 0.105\varepsilon_{co} \tag{2.10}$$

where the value of ε_{c2} is evaluated from Equation 2.9. This equation was developed by Graybeal et al. based on their proposed tangent dilation ratio relationship, which is discussed in Section 2.3.5. Compared to their experimental data, Equation 2.10 generally provided a conservative estimate of ε_{ct2}.

In Step 5, assuming strain compatibility, the strain in the spiral reinforcement is the same as the transverse strain in the concrete core. This relationship applies at all strains, including those at the second peak in the load-shortening response of the member. This relationship is expressed by Equation 2.11 as

$$\varepsilon_{sp2} = \varepsilon_{ct2} \tag{2.11}$$

where ε_{sp2} is the strain in the spiral reinforcement at the second peak in the load-shortening

response of the member. This represents the *useable strain* in the spiral reinforcement. The value of useable strain will be unique for the combination of pile geometry and concrete compressive strength selected for the design of a spirally reinforced pile. The useable strain is not dependent upon the stress-strain curve of the spiral reinforcement.

Once the useable strain is known, Step 6 in the proposed design method is to determine the *useable stress* for which the pile should be designed. The useable stress, defined as the stress in the spiral reinforcement corresponding to the peak core strength and denoted as f_{sp2}, is obtained through the use of an appropriate stress-strain curve for the spiral wire. Thus, while the useable strain is independent of the stress-strain curve of the spiral, the useable stress does depend upon the stress-strain curve. The ideal situation is to utilize the stress-strain curve of the spiral in its in-situ, or spiraled, state. However, it is more probable that only a stress-strain curve from a tension test of an unspiraled wire will be available, which does not accurately represent the behavior of the spiraled wire. In this case, the value obtained may need to be modified in order to ensure a proper design. Section 2.3.4 presents a discussion of why a modification of the obtained value might be necessary.

In Step 7, the required volumetric ratio of the spiral steel is determined through Equation 2.12.

$$\rho_{sp} = \frac{2f_{2-2}}{f_{sp2}} \tag{2.12}$$

This equation is a revised form of Equation 2.4.

Finally, Step 8 in the proposed design procedure is to compute the required pitch from statics using the previously calculated spiral steel ratio and a given wire diameter. Equation 2.13 is a revised form of Equation 2.6 and is written as follows:

$$s = \frac{4A_{sp}}{d_{sp}\rho_{sp}} \tag{2.13}$$

It is noted that Equations 2.9 and 2.10 provide conservative estimates of ε_{c2} and ε_{ct2}. As a result, the design procedure proposed by Graybeal et al. should lead to a conservative value of useable stress, f_{sp2}, provided the proper stress-strain curve and/or appropriate modification factor is used, and, therefore, to a conservative design of the spiral reinforcement for the pile.

2.3.4 Spiral Steel Stress-Strain Properties

The design procedure for high strength spiral reinforcement in prestressed concrete piles developed by Graybeal et al., as just discussed in the previous section, involves the use of stress-strain curves for the spiral steel. The design method will be most accurate if the in-situ stress-strain curve of the spiral reinforcement is utilized. However, this curve is not readily obtainable. Therefore, stress-strain curves of the spiral steel in its unspiraled condition or in a spiraled-straightened state would be used instead. As previously mentioned in Section 2.3.1, an unspiraled wire is a wire that has

never been spiraled, a spiraled wire is a wire that has been bent to a certain curvature, and a spiraled-straightened wire is a wire that has been spiraled and then straightened to its original shape. While the stress-strain curve from the in-situ (spiraled) condition is more desirable, obtaining the relationship for unspiraled or spiraled-straightened cases is more practical. Thus, the differences in the curves must be understood by the designer.

Graybeal et al. provide a detailed discussion on how the spiraling and straightening processes affect both the stress distribution across the cross-section of a wire and the tension stress-strain properties of the wire. A brief synopsis of that material and the findings obtained through their fiber model study is presented below.

The spiraling process is a physical process of transforming a straight length of wire into a helical shape. Conceptually, the spiraling process can be thought of as applying a constant bending moment along the length of the wire. After the spiraling process is completed and all applied forces (moments) are removed, a permanent deformed shape results. The permanent deformation results from the fact that a portion of the wire cross-section has yielded, or undergone plastic deformation. The deformed shape is a function of the residual strain distribution across the cross-section of the wire. These residual strains result in residual stresses on the cross-section. If a straightening process is now invoked, which conceptually can be thought of as applying a bending moment opposite in sense to the spiraling moment, the permanent set will physically disappear (residual strains will be zero). However, there will still be residual stresses remaining on the wire cross-section even though the final strains will be zero.

The impact of these residual stresses is as follows. As previously stated, these residual stresses imply prior yielding of parts of the cross-section. As tension is applied to a wire without any residual stresses, a uniform distribution of tensile strain and tensile stress is produced across the wire cross-section. Eventually, as the loading continues on the wire, theoretically, the entire cross-section will begin to yield at once. However, in the case of a spiraled or spiraled-straightened wire, the superposition of uniform tensile stresses onto the residual stress distribution causes parts of the cross-section (i.e. the parts in residual tension) to reach their yield values before other parts of the cross-section (i.e. the parts in residual compression). Early yielding of the portions of the cross-section in residual tension effectively reduces the percentage of the cross-section that can elastically resist load. Figure 2.3 illustrates this effect for an idealized mild (elastic-plastic) steel after the spiraling process, and Figure 2.4 illustrates this for a spiraled-straightened wire of mild steel.

Graybeal et al. performed fiber model analyses of a wire of physical properties and stress-strain behavior similar to the spiral wires used in the spirally reinforced piles. The analyses were performed using the DRAIN-2DX program (Prakash and Powell, 1993). Details of the fiber model are given in Graybeal et al. Analyses were performed on unspiraled, spiraled, and spiraled-straightened wires. A stress-strain curve obtained from experimental tension tests on an unspiraled spiral wire was modeled as a 5-piece multi-linear curve, which set the stress-strain properties for the steel. In the case of the spiraled wire, a constant bending moment was first applied to the straight wire to bend it into a spiral of diameter smaller than the desired 20 in. (508 mm) or 10 in.

(254 mm) outside diameters, corresponding to the diameters of the spirals used in the piles. This moment was then removed by application of an equal and opposite moment. By a trial and error approach, the correct spiraling moment was found to cause the wire to deform to the desired curvature when all moments were released. For the straightening process, a moment opposite in sense and slightly smaller in magnitude than the spiraling moment was first applied to the spiraled wire. Then, the straightening moment was removed by application of an equal and opposite bending moment. Once again, through a trial and error approach, the correct straightening moment was found to cause all strains in the cross-section to equal zero when all moments were released. Finally, the unspiraled, spiraled, and spiraled-straightened wires were loaded in tension to obtain a monotonic uniaxial stress-strain curve for the wire in each state. The results of the fiber model analyses are shown in Figure 2.5.

Graybeal et al. made several important observations from Figure 2.5. First, the curve for the unspiraled wire resembles the multi-linear approximation to the actual stress-strain curve of the unspiraled wire, as expected. Next, it is seen that the spiraling process leads to a rounding of the original stress-strain curve. Also, while the straightening process helps reduce the overall magnitude of the residual stress, all stresses are not removed. Thus the stress-strain curve for the spiraled-straightened wire falls between the curves for the unspiraled and spiraled wires. Furthermore, rounding of the stress-strain curves is more severe in the case of the smaller spiral diameter. This occurs because it takes a greater applied moment to create a greater curvature, causing more of the cross-section to become inelastic. Effectively, this results in greater residual stresses and leaves less area of the cross-section remaining free from residual stresses. Figure 2.6 illustrates these concepts for 60 ksi (414 MPa) elastic-plastic steel wires which were coiled into two different diameter spirals. Figure 2.7 shows the residual stresses on the cross-section of the steel spiral wires after undergoing both the spiraling and straightening processes.

The importance of this discussion to the design procedure developed by Graybeal et al. is as follows. In the design procedure, a useable stress value is obtained from a known useable strain through the stress-strain relationship of the spiral wire. This concept is illustrated in Figure 2.8 for a typical high strength spiral reinforcing steel. This figure shows two tensile stress-strain curves: one representing the steel tested in its spiraled state, and the other representing the steel in its unspiraled state. Had a curve been shown representing the spiraled-straightened state, it would have fallen between the two curves shown. The desired stress-strain relationship is that of the wire in its spiraled state because that is the stress-strain relationship exhibited by the wire in place in the pile. However, stress-strain relationships are not normally developed for spiraled wires; instead, tension tests are performed on unspiraled or spiraled-straightened wires. In Figure 2.8, the useable strain value lies within the range of where the rounding takes place (which the experimental work showed to be a good assumption). Therefore, by utilizing the unspiraled curve to locate the useable stress at ε_{sp2}, the value obtained is an overestimate of the true value. Depending upon the value of the useable strain as well as the shape of the unspiraled stress-strain curve, the error in this process, expressed as the difference in stress values between the unspiraled and spiraled states ($f_{sp2,US} - f_{sp2,S}$) divided by the true useable stress in the spiraled condition ($f_{sp2,S}$), can be significant. The overestimate in useable stress results in an overestimate of the confining pressure applied to the

concrete core and results in a value of P_2 which is lower than expected. If the spiral reinforcement for pile was designed so that P_2 matched P_1, the spirals for the pile will actually be underdesigned, and P_2 will be less than P_1.

2.3.5 Tangent Dilation Ratio Relationship Proposed by Graybeal et al.

A key component of the proposed design procedure for the design of high strength spiral reinforcement for prestressed concrete piles is the proposed tangent dilation ratio relationship. From given concrete material properties and a desired core strength, the longitudinal strain in the pile, ε_{c2}, is calculated from Equation 2.9. The proposed dilation ratio relationship provides the means to estimate the transverse strain in the concrete pile from the longitudinal strain. Once the transverse strain is known, the useable spiral strain and useable spiral stress are computed. The remainder of this section explains the development of the proposed tangent dilation ratio relationship, which was given as Equation 2.10.

$$\varepsilon_{ct2} = 0.41\varepsilon_{c2} - 0.105\varepsilon_{co} \tag{2.10}$$

The dilation ratio is a quantity which describes the relationship between transverse strain and longitudinal strain of the concrete core. In the work of Graybeal et al., this relationship was defined in two ways. Figure 2.9(a) shows an idealized plot of transverse strain versus longitudinal strain for a pile. Figures 2.9(b) and 2.9(c) are plots of the secant and tangent dilation ratios, respectively, both of which are obtained from Figure 2.9(a).

The secant dilation ratio, η_{sec}, was defined as the ratio of transverse to longitudinal strain at any point in the response of the core. This is represented by Equation 2.14.

$$\eta_{sec} = \frac{\varepsilon_{ct}}{\varepsilon_c} \tag{2.14}$$

If known, the secant dilation ratio can be used to compute the transverse strain at any point based on the value of the longitudinal strain. Basically, Figure 2.9(b) represents the slope of a line drawn from the origin of Figure 2.9(a) to any point on the curve. This line is a secant to the curve, hence the slope of this line is called the secant dilation ratio. If η_{sec} and the longitudinal strain are known at a point, the transverse strain is calculated directly.

The tangent dilation ratio, η_{tan}, was defined as the slope of the curve of transverse strain versus longitudinal strain at any point along the curve. Equation 2.15 defines the tangent dilation ratio at any point.

$$\eta_{tan} = \frac{d\varepsilon_{ct}}{d\varepsilon_c} \tag{2.15}$$

Both secant and tangent dilation ratio relationships were evaluated for each pile using the available strain gage data and were plotted against the average of the longitudinal strain gage strains. The secant dilation ratio for each spiral gage was calculated as the spiral strain divided by the average longitudinal strain gage strain. The approximated secant dilation ratio at the second peak, η_{sec2}, was

identified for each pile based on the average of the trends observed in the individual η_{sec} curves. This is the value which directly relates ε_{c2} to ε_{ct2} as is shown in Equation 2.16.

$$\varepsilon_{ct2} = \eta_{sec2}\varepsilon_{c2} \tag{2.16}$$

In calculation of the tangent dilation ratio, the increment of increased transverse strain was calculated for each increment of increased longitudinal strain throughout the response of the pile up to P_2. This calculation was performed for each of the spiral strain gages for each increment of longitudinal strain. The resulting curves are the tangent dilation ratio relationship for the spiral gages. These curves were then averaged and smoothed by taking a moving average of the ten values of η_{tan} closest to each value of η_{tan} for each longitudinal strain increment. As was previously described, the area under the η_{tan} curve up to any longitudinal strain is equal to the transverse strain at that longitudinal strain. Thus, the area under smoothed η_{tan} curve between $\varepsilon_c = 0$ and ε_{c2}, denoted as $A_{\eta tan2}$ is equal to the transverse strain ε_{ct2}. This is shown in equation form in Equation 2.17.

$$\varepsilon_{ct2} = A_{\eta tan2} \tag{2.17}$$

In general, the results acquired by Graybeal et al. showed that the secant dilation behavior of the pile was constant or decreasing until ε_{c1} was neared. Between ε_{c1} and ε_{c2}, the results showed that the general trend was for a slight increase in η_{sec}. In the 24 in. (610 mm) diameter piles, the approximated values of η_{sec2} ranged from 0.45 to 0.5 while in the 14 in. (356 mm) diameter piles, the approximated values ranged from 0.35 to 0.45.

The results of the tangent dilation ratio computations and plots (see Graybeal et al. (1998)) showed that η_{tan} was approximately constant from $\varepsilon_c = 0$ to nearly ε_{c1}. The plots also showed that the concrete exhibited a higher dilation ratio after cover spalling. In the 24 in. (610 mm) specimens, η_{tan} increased as ε_{c2} was neared. This was in contrast to the behavior exhibited by the 14 in. (356 mm) diameter piles where the tangent dilation ratio was constant near ε_{c2}. It was speculated that the higher confining stresses on the smaller diameter piles did not allow the dilation ratio to continue increasing above a certain limit.

Graybeal et al. compared the experimentally determined values of transverse strain at Δ_2 with the values of transverse strain obtained using the experimentally determined secant and tangent dilation ratios. The secant dilation ratio approximation of ε_{ct2} was computed from Equation 2.16 and the experimental value of ε_{c2}. In every case the prediction of the transverse strain was within 25 percent of the experimentally obtained value. The tangent dilation ratio approximation of ε_{ct2} was computed from Equation 2.17. In every case, the predicted values of the transverse strain were within 12 percent of the experimentally obtained values. As stated earlier, this proposed tangent dilation ratio relationship is used to estimate the value of ε_{ct2} from the value of ε_{c2} as part of the procedure for the design of high strength spirals.

The basic shape of the proposed tangent dilation ratio relationship between $\varepsilon_c = 0$ and ε_{c2} is shown in Figure 2.10(a). This figure shows that the tangent dilation ratio has an initial constant value, $\eta_{tan,ini}$, up to a longitudinal strain of $\alpha\varepsilon_{co}$. At this point the tangent dilation ratio increases in a linear

manner to a second constant value of $\eta_{tan,lim}$. This limiting value is reached at a longitudinal strain of $\beta\varepsilon_{c2}$.

Figure 2.10(b) shows the same plot with the longitudinal strain normalized by the unconfined concrete strain, ε_{co}. Accordingly, the variable m is defined as Equation 2.18.

$$m = \frac{\varepsilon_{c2}}{\varepsilon_{co}} \tag{2.18}$$

As was shown in Equation 2.16, the area under the tangent dilation ratio curve between $\varepsilon_c = 0$ and ϵ_{c2}, denoted as $A_{\eta tan2}$, is equivalent to ϵ_{ct2}. Calculating the area shown in Figure 2.10(a) provides the area $A_{\eta tan2}$ shown in Equation 2.19.

$$A_{\eta\tan 2} = \varepsilon_{co}\left(\frac{1}{2}\alpha\left(\eta_{\tan,ini} - \eta_{\tan,lim}\right) + m\left(\frac{1}{2}\eta_{\tan,ini}\beta - \frac{1}{2}\eta_{\tan,lim}\beta + \eta_{\tan,lim}\right)\right) \tag{2.19}$$

Dividing Equation 2.19 by the normalizing factor, ε_{co}, provides the normalized value of the area, $\bar{A}_{\eta tan2}$. This is shown in Equation 2.20.

$$\bar{A}_{\eta\tan 2} = \frac{1}{2}\alpha\left(\eta_{\tan,ini} - \eta_{\tan,lim}\right) + m\left(\frac{1}{2}\eta_{\tan,ini}\beta - \eta_{\tan,lim}\beta + \eta_{\tan,lim}\right) \tag{2.20}$$

Graybeal et al. proposed the following values for the variables α, β, $\eta_{tan,ini}$, $\eta_{tan,lim}$: $\alpha = 0.7$; $\beta = 0.6$; $\eta_{tan,ini} = 0.2$; and $\eta_{tan,lim} = 0.5$. Inserting these proposed values into Equation 2.19 provides Equation 2.21.

$$A_{\eta\tan 2} = \varepsilon_{co}\left(m(0.41) - 0.105\right) \tag{2.21}$$

Again, noting that $A_{\eta tan2}$ equals ϵ_{ct2}, this equation can be rewritten as Equation 2.10, presented earlier.

$$\varepsilon_{ct2} = 0.41\varepsilon_{c2} - 0.105\varepsilon_{co} \tag{2.10}$$

A comparison of the proposed and experimental tangent dilation ratio curves revealed the following. First, the initial constant portion of the proposed curve modeled well the behavior observed in the 14 in. (356 mm) diameter piles. For the 24 in. (610 mm) piles, this portion of the proposed curve tended to underestimate the experimental behavior. Next, for both diameter piles, the increasing portion of the proposed curve tended to model the experimental findings relatively well. Finally, in general, for the 14 in. (356 mm) diameter piles, the constant portion of the proposed curve modeled well the tangent dilation ratio behavior near ε_{c2}. The 24 in. (610 mm) diameter piles tended to exhibit an increased η_{tan} near ϵ_{c2}. Thus, the model provided a conservative estimate of the tangent dilation ratio for these piles.

Pile	Diam. (in.)	Cover (in.)	Height (in.)	f_{co} (ksi)	f_{sy} (ksi)	ρ_{sp} %	f_{ly} (ksi)	ρ_{lg} %
24-A	24	2	96	8.0	78	2.04	60	0.26
24-B	24	2	96	8.0	107	1.49	60	0.26
24-C	24	2	96	8.0	121	1.31	60	0.26
24-D	24	2	96	8.0	140	1.13	60	0.26
14-A	14	2	56	8.0	78	4.47	60	0.51
14-B	14	2	56	8.0	107	3.26	60	0.51
14-C	14	2	56	8.0	121	2.88	60	0.51
14-D	14	2	56	8.0	140	2.49	60	0.51

1 ksi = 6.895 MPa
1 in. = 25.4 mm

Table 2.1 Summary of design parameters used by Graybeal et al. (1998).

Pile	Spiral Reinforcement					Longitudinal Reinforcement			
	d_{sw} (in.)	n_{sp}	A_{sp} (in.^{2})	s (in.)	ρ_{sp} %	Bar Size	n_{lg}	A_{lg} (in.^{2})	ρ_{lg} %
24-A	0.35	2	0.1924	1.875	2.05	#4	6	1.18	0.26
24-B	0.35	2	0.1924	2.500	1.54	#4	6	1.18	0.26
24-C	0.35	1	0.0962	1.500	1.28	#4	6	1.18	0.26
24-D	0.35	1	0.0962	1.750	1.10	#4	6	1.18	0.26
14-A	0.35	2	0.1924	1.750	4.40	#4	4	0.79	0.51
14-B	0.35	2	0.1924	2.375	3.24	#4	4	0.79	0.51
14-C	0.35	1	0.0962	1.375	2.80	#4	4	0.79	0.51
14-D	0.35	1	0.0962	1.500	2.57	#4	4	0.79	0.51

1 in. = 25.4 mm

Table 2.2 Summary of reinforcement provided in each pile tested by Graybeal et al. (1998).

Pile	$f_{sy,nom}$ (ksi)	Δ_1		Δ_{spall}		Δ_2		$R_{P1/P2}$	$R_{fsp2/fsy,nom}$
		P_1 (kips)	f_{sp1} (ksi)	P_{spall} (kips)	$f_{sp,spall}$ (ksi)	P_2 (kips)	f_{sp2} (ksi)		
24-A	78	3910	25	2951	35	3826	70	0.98	0.90
24-B	107	3950	32	3173	50	3691	95	0.93	0.89
24-C	121	3926	28	3202	45	3579	85	0.91	0.70
24-D	140	3985	29	3092	55	3337	85	0.84	0.61
14-A	78	1359	25	957	35	1337	80	0.98	1.03
14-B	107	1366	28	959	45	1276	95	0.93	0.89
14-C	121	1367	20	921	45	1248	115	0.91	0.95
14-D	140	1355	22	924	40	1228	125	0.91	0.89

1 ksi = 6.895 MPa
1 kip = 4.448 kN

Table 2.3 Loading data and stresses in the spiral reinforcement at Δ_1, Δ_{spall}, and Δ_2 for tests conducted by Graybeal et al. (1998).

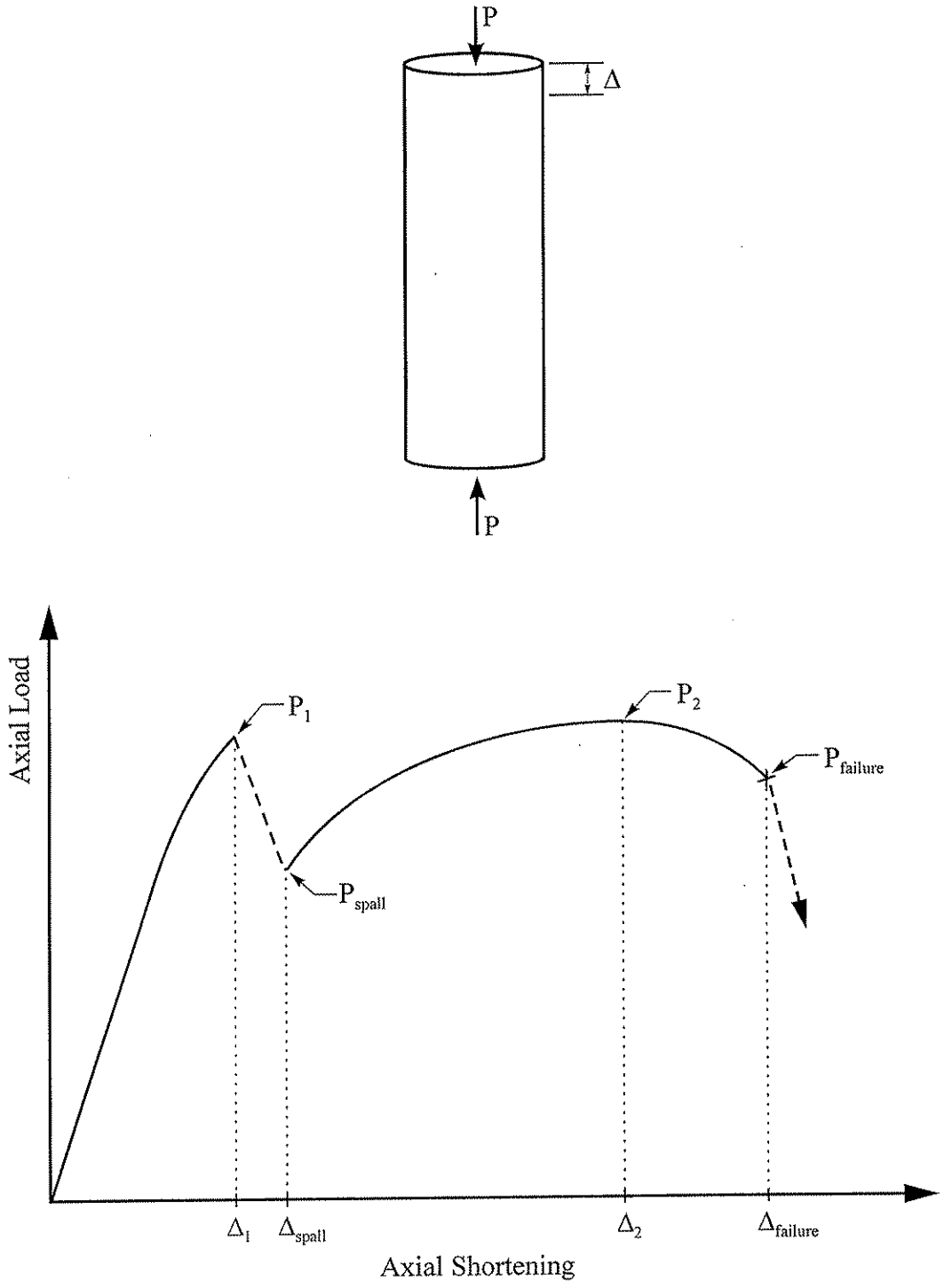

Figure 2.1 Idealized load-shortening behavior of a spirally reinforced member (Graybeal et al. (1998)).

Given: Pile dimensions, reinforcing (longitudinal and spiral) steel parameters, spiral steel stress-strain curve, unconfined concrete compressive strength, ultimate concrete strain.

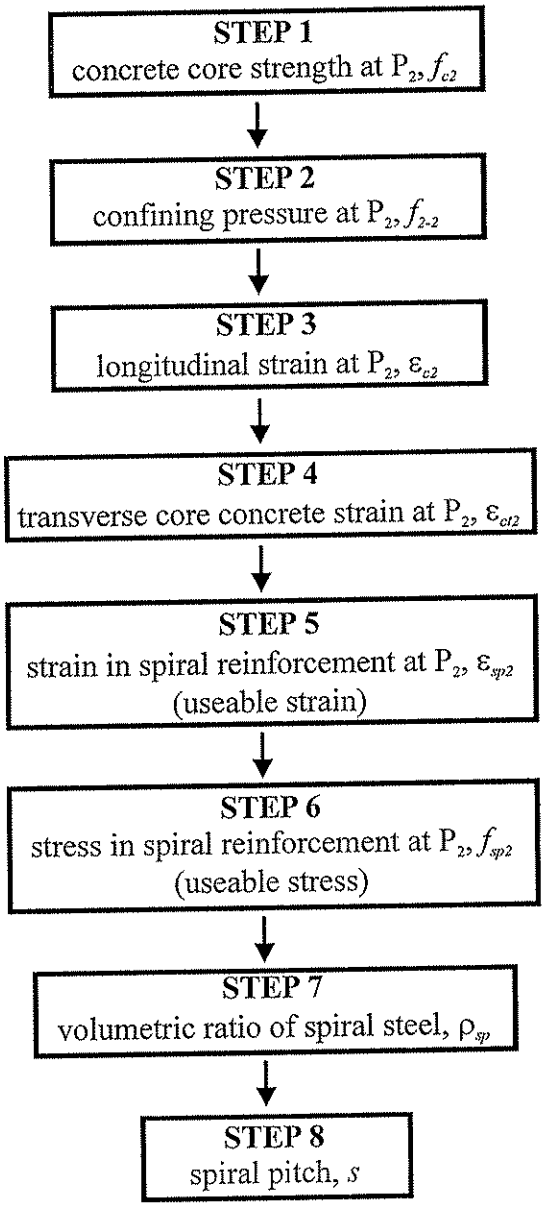

Figure 2.2 Schematic view of design approach proposed by Graybeal et al. (1998).

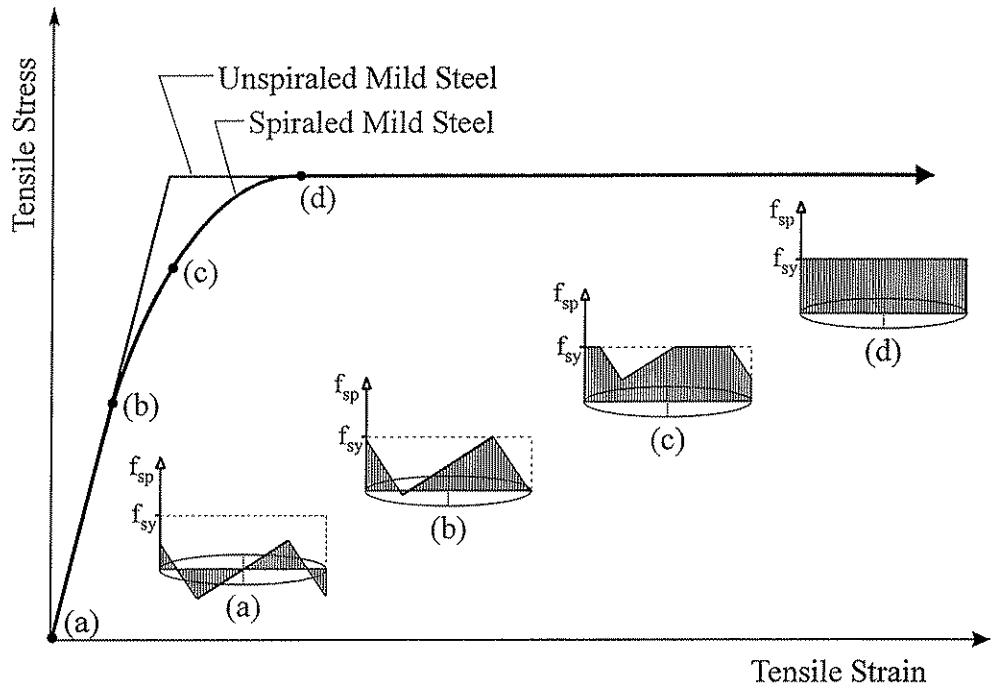

Figure 2.3 Stresses in the cross-section of a spiraled wire throughout the application of a tensile load (Graybeal et al. (1998)).

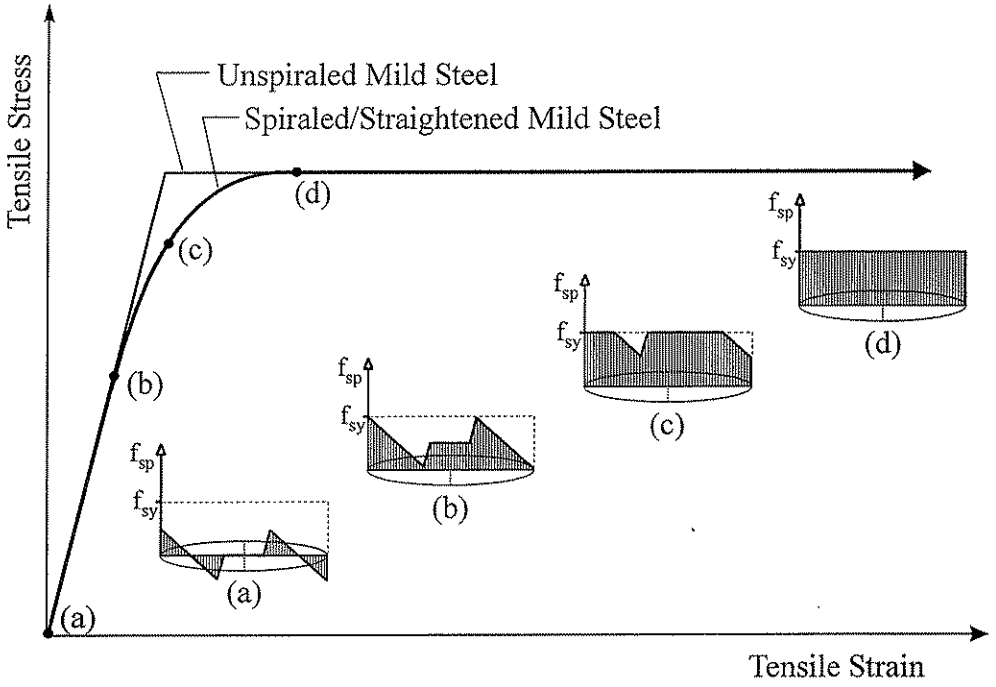

Figure 2.4 Stresses in the cross-section of a spiraled-straightened wire throughout the application of a tensile load (Graybeal et al. (1998)).

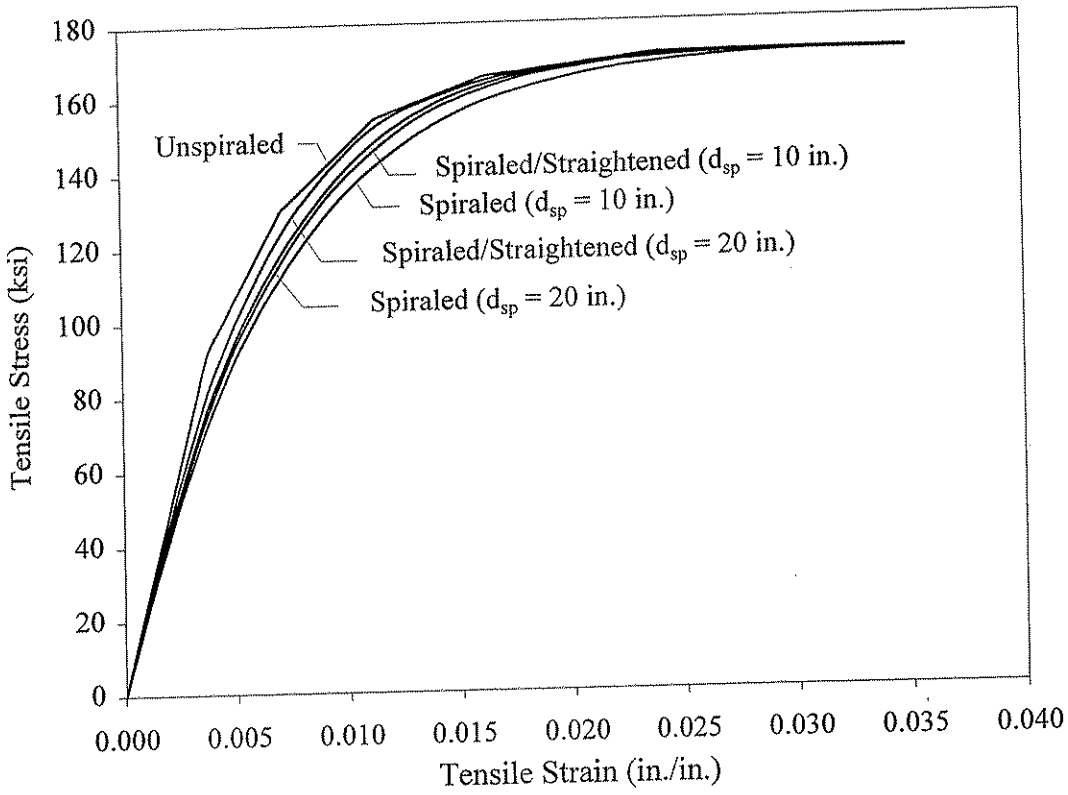

Figure 2.5 Fiber model analysis results showing effect of spiraling and straightening on Grade D spiral reinforcement (Graybeal et al. (1998)).

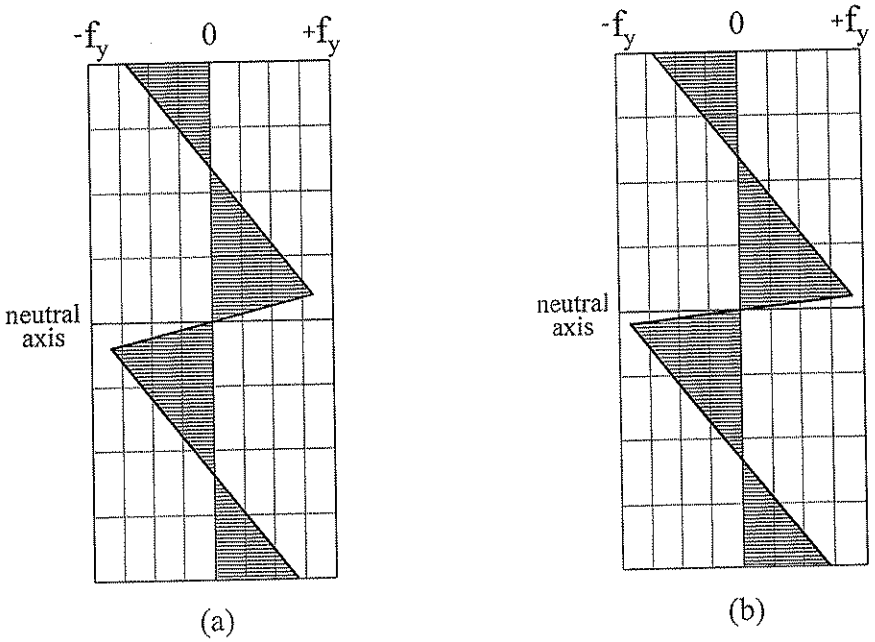

Figure 2.6 Residual stresses on the cross-section of a spiraled wire from fiber model analysis results for 60 ksi elastic-plastic steel, 0.35 in. diameter wire: (a) 20 in. spiral diameter; (b) 10 in. spiral diameter (Graybeal et al. (1998)).

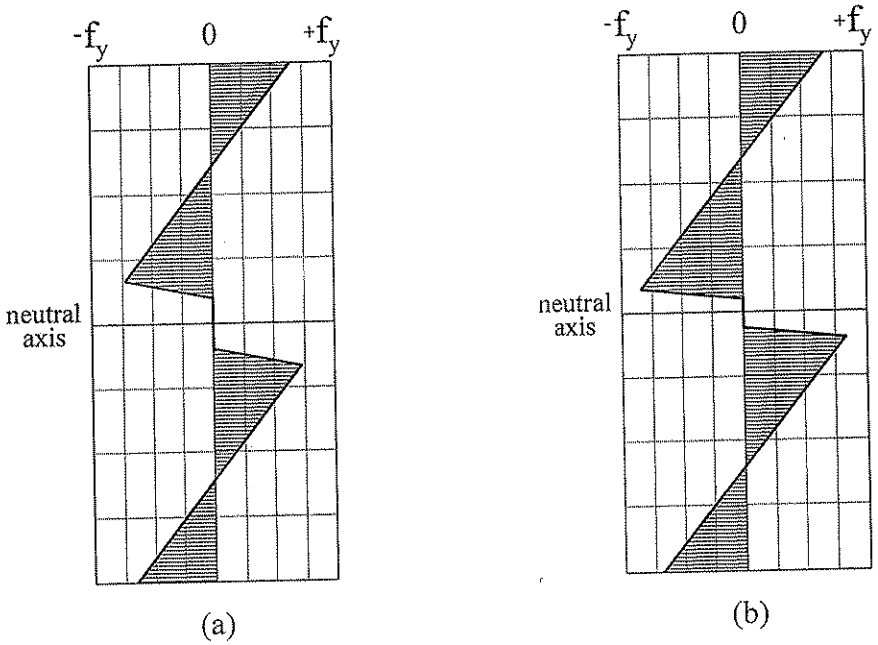

Figure 2.7 Residual stresses on the cross-section of a spiraled-straightened wire from fiber model analysis results for 60 ksi elastic-plastic steel, 0.35 in. diameter wire: (a) 20 in. spiral diameter; (b) 10 in. spiral diameter (Graybeal et al. (1998)).

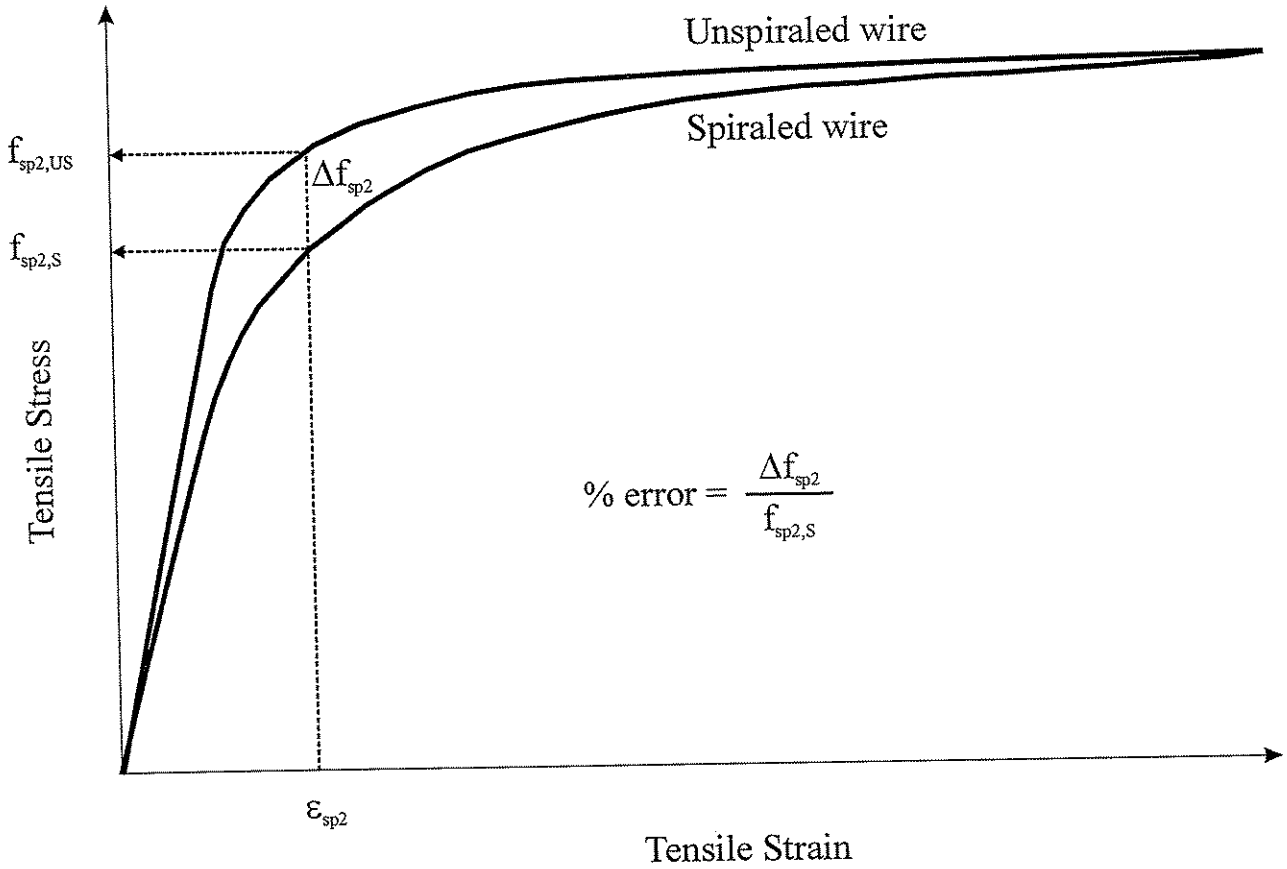

Figure 2.8 Tensile stress-strain curves for a typical high strength spiral steel showing the effect of spiraling on the determination of useable stress.

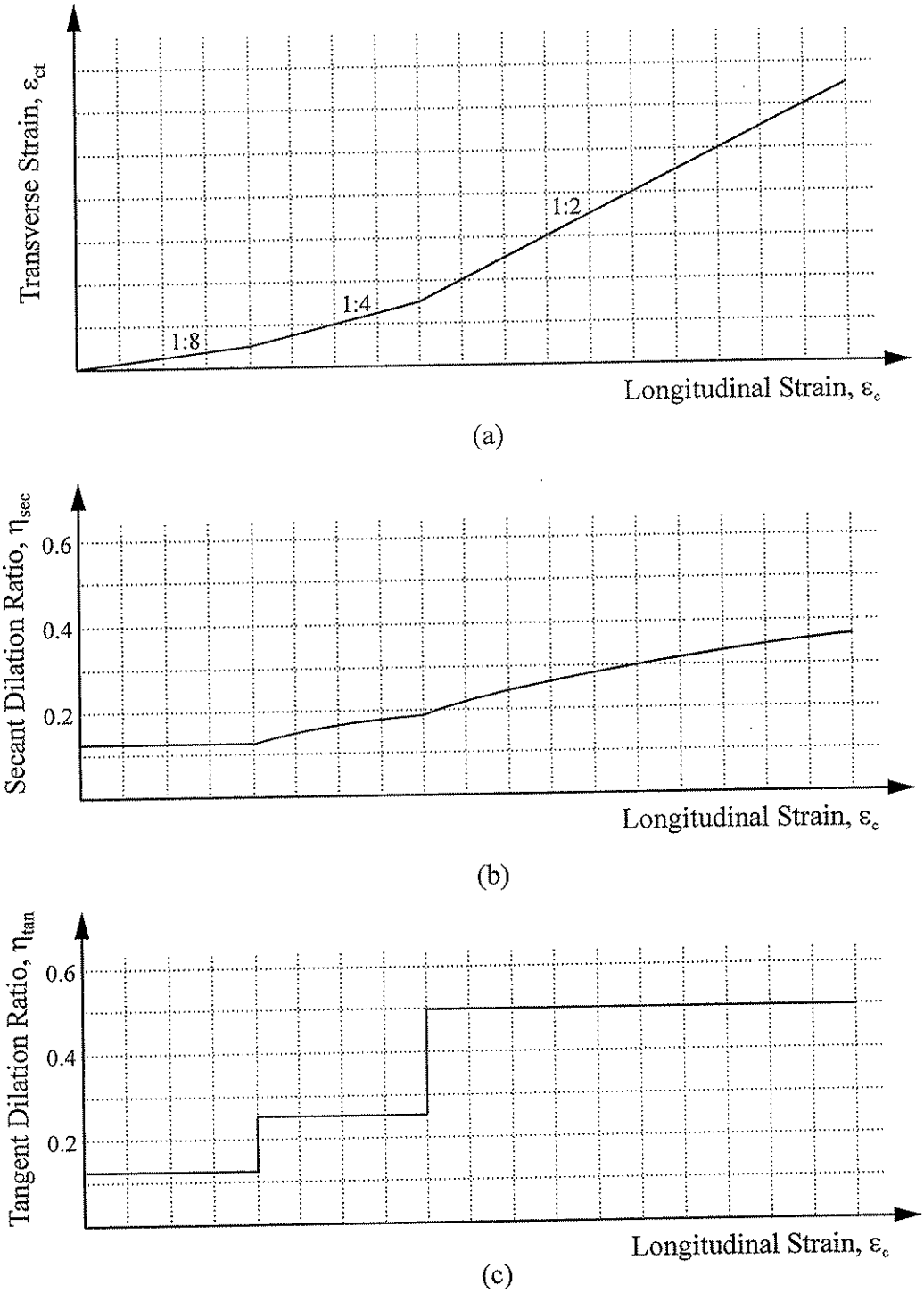

Figure 2.9 Definitions of dilation ratios: (a) idealized plot of transverse strain versus longitudinal strain; (b) secant dilation ratio; and (c) tangent dilation ratio (Graybeal et al. (1998)).

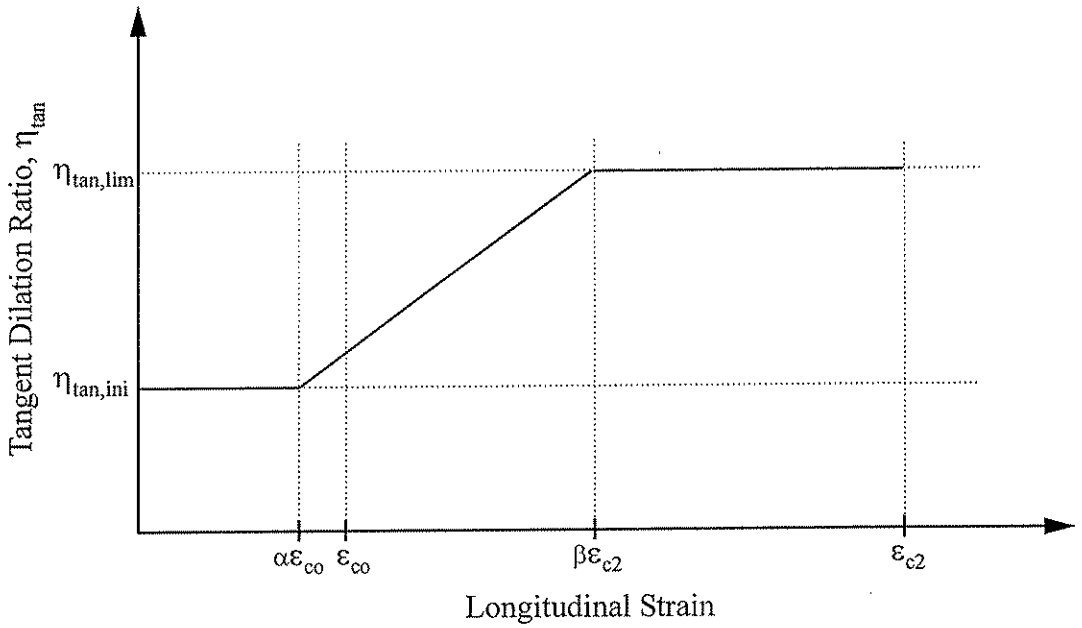

(a)

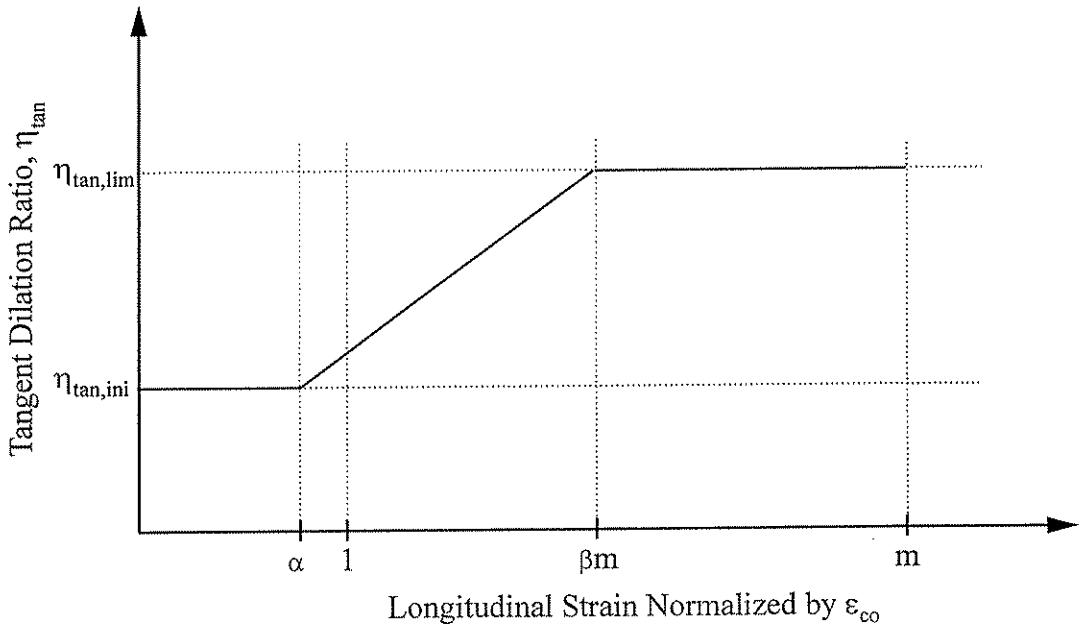

(b)

Figure 2.10 Proposed tangent dilation ratio relationship: (a) general form; (b) normalized by ε_{co} (Graybeal et al. (1998)).

CHAPTER 3
DESCRIPTION OF EXPERIMENTAL PROGRAM

3.1 INTRODUCTION

This chapter describes the experimental program. Section 3.2 presents the test matrix, and Section 3.3 presents the specimen details. The instrumentation which was used to measure specimen behavior during testing is described in Section 3.4. Section 3.5 explains how the specimens were made. Section 3.6 describes the loading procedure used in the testing of the pile specimens. Concrete material properties are presented in Section 3.7. Finally, the material properties of the spiral and longitudinal reinforcement are described in Section 3.8.

3.2 TEST MATRIX

The test matrix for this research, given in Table 3.1, was designed to investigate the proposed design procedure developed by Graybeal et al. (1998). The test matrix included six 14 in. (356 mm) diameter pile specimens made with six different spiral wires. Although the spiral reinforcement varied in nominal yield stress, the primary variable examined in this research was the useable stress, f_{sp2}. The alpha-numeric identifier for each specimen is used to indicate which wire is used for the specimen. Specimens identified as 14-A' through 14-D' represent piles containing spiral wires with reported yield stresses as follows: A' = 78 ksi (538 MPa), B' = 107 ksi (738 MPa), C' = 121 ksi (834 MPa), and D' = 140 ksi (965 MPa). These are the same spiral wires that were treated in the previous work by Graybeal et al. Two additional spiral wires which were not included in the work by Graybeal et al. are denoted E' and F'. Specimens 14-E' and 14-F' are the piles made with spiral steels that had reported nominal yield stresses of 195 ksi (1345 MPa) and 185 ksi (1276 MPa), respectively.

3.3 SPECIMEN DETAILS

Table 3.2 provides a summary of the design parameters for each pile. Each pile specimen measured 56 in. (1.42 m) in height and had a diameter of 14 in. (356 mm), which resulted in a height-to-diameter aspect ratio of 4-to-1. Figure 3.1 is a cross-sectional view of the reinforcement layout. Each pile contained 2 in. (51 mm) clear concrete cover between the outside of the spiral reinforcement and the outer surface of the specimen. All piles were designed using a concrete compressive strength, f_{co} = 8.0 ksi (55.2 MPa).

Figure 3.2 is a photograph of the specimen reinforcement cages prior to placement in the formwork. This figure shows that extra spiral confinement was provided within one diameter of height from each end. This was done to ensure that failure would occur in the middle half of the specimen height, also referred to as the test region.

Table 3.3 summarizes the reinforcement details for each specimen. Spiral pitch was determined through the design procedure developed by Graybeal et al., which was presented in Section 2.4. Several restrictions were implemented. The range of clear spacing was limited to between 1 in. (25.4 mm) to 3 in. (76.2 mm) and had to satisfy aggregate size requirements given in the ACI 318 Code and AASHTO Design Specification. In order to meet these requirements, two spiral wires

were bundled to fabricate the reinforcement cages for Specimen 14-A' and for Specimen 14-B'. This can be seen in Figure 3.2. Nominal 0.35 in. (8.9 mm) diameter spiral wires were used for Specimen 14-A' through Specimen 14-D', and 0.36 in. (9.1 mm) and 0.43 in. (10.9 mm) diameter spiral wires were used for Specimen 14-E' and Specimen 14-F', respectively.

Four #4 (0.5 in. (12.7 mm) diameter) Grade 60 deformed steel bars were used as longitudinal reinforcement in each pile. These bars were used to hold the spiral reinforcement in position during concrete placement. They provided a longitudinal steel ratio of 0.51 percent.

None of the pile specimens were prestressed. While prestressing is beneficial in preventing cracking during specimen transportation and increasing bending strength, especially in eccentrically loaded members, its effects in this research were expected to be of no consequence.

3.4 INSTRUMENTATION

Two types of instruments were utilized during testing. Electrical resistance strain gages (type CEA-06-250UN-120 from Measurements Group, Inc.) were used to measure strains in both the longitudinal and spiral reinforcement. Linear Variable Differential Transformers (LVDT) displacement transducers were employed to monitor the head travel of the testing machine, which was therefore a measure of the overall axial shortening of the pile specimens. The total number of strain gages used on each specimen varied between fifteen and seventeen. All gages were placed within the test region. Figure 3.3 shows the typical gage layout. Spiral gages, denoted S1 through S13, were distributed along the height of the test region in an alternating fashion between two locations, which were separated by 180 degrees around the spiral circumference. Also, the spiral gages were positioned midway between the longitudinal reinforcement to minimize the effects of bending of the spirals around the longitudinal bars. The spiral gages were generally placed on the bottom of the spiral wires and centered on the neutral axis about which the wires were coiled. This location provided maximum protection during concrete placement while at the same time reducing any bending effects. Where the spirals were bundled (Specimen 14-A', Specimen 14-B') the gages were placed alternately on each wire in order to detect any differences in strain between the wires.

Four gages, denoted L1 through L4, were placed on the longitudinal reinforcement of each specimen. Figure 3.3 shows that gages L1 and L3 were placed on the same longitudinal reinforcing bar, and that gages L2 and L4 were placed on the bar opposite to that on which L1 and L3 were located. All longitudinal gages were positioned so that the face of each gage was perpendicular to the diameter of the pile in order to reduce the bending effects of the longitudinal reinforcement on the measured strain values.

Two LVDTs were utilized in each test. One LVDT was attached to the testing machine head about 3 in. (76 mm) east of the specimen, and the other LVDT was located on the northwest corner of the testing machine head. The second instrument was used as a back-up reading in the event that the reading from the LVDT nearest the specimen was interrupted due to spalling concrete. Test results showed good agreement between the two measurements.

A computer-based data acquisition system was employed to sample and record all instrumentation, including the axial force applied to the pile by the 5000 kip (22.2 MN) capacity universal testing machine.

3.5 SPECIMEN FABRICATION

The steel reinforcement cages were assembled from straight deformed longitudinal reinforcing bars and collapsed helical spirals. The spiral wires were fastened to the longitudinal bars at the correct pitch using ordinary tie wire. Most coils of spiral contained between twenty and twenty-five turns of wire, although some coils used in the confined regions were comprised of fewer turns. In fabrication of the specimens, splicing of the spiral reinforcement was unavoidable. Where splicing was necessary, the spiral wires were overlapped between one and one-and-one-half turns. All splices were restricted to the heavily confined regions.

Figure 3.2 shows the reinforcement cages before placement into the formwork. The test region can clearly be distinguished from the heavily confined end regions in each specimen. This figure shows that, for each specimen, an additional spiral was bundled within one diameter from each end to create the confined regions, and that all splicing occurred within these regions.

For each specimen, 2 in. (51 mm) high chairs were utilized to maintain proper positioning of the reinforcing cage in the formwork and to ensure that the desired uniform concrete cover was provided. After the reinforcing cages had been completed and all strain gages were properly attached, the cages were inserted into cylindrical cardboard tubes, which served as the formwork. These tubes were then aligned adjacent to each other on a plywood base.

Along with the six spirally reinforced specimens, two plain concrete piles were prepared. One of these specimens, denoted as Specimen PCP1, contained two longitudinal bars, and the other one, denoted as Specimen PCP2, contained no reinforcement whatsoever. Several cores were extracted from unreinforced regions of Specimen PCP1. These cores were tested in axial compression. Specimen PCP2 was tested in concentric axial compression in the same manner as the spirally reinforced specimens. In addition, a number of 6 × 12 in. (152 × 305 mm) field cured cylinders were cast and later tested in axial compression.

All specimens were oriented vertically during concrete placement and curing. For each pile specimen, the concrete was placed in two lifts. Each lift was consolidated with an electrically powered internal submersion vibrator.

The piles were cured in the cardboard forms for 50 days, during which time the tops of them were covered in wet burlap and plastic sheeting. This unusually long curing period was used because early tests of 6 × 12 in. (152 × 305 mm) cylinders revealed that the material was only slowly coming up to the 8.0 ksi (55.2 MPa) design strength. After a total of 53 days, all specimens were stripped from their forms. The cylinders, which were kept in the same type of environment as the piles, were also removed from their plastic molds at this time.

3.6 LOADING PROCEDURE

Each 14 in. (356 mm) diameter specimen was tested under concentric axial compression in a 5000 kip (22.2 MN) capacity universal testing machine. Hydrostone was applied to both the top and bottom ends of each pile to ensure plumbness and to provide uniform contact between the specimen and the testing machine platens.

The load and loading rate were monitored throughout the test, and the manner in which each specimen was tested was based upon these values. Through the initial portion of each test, the load rate was around 24 kips/min. (107 kN/min.), which corresponded to a stress rate of about 155 psi/min. (1069 kPa/min) and an axial shortening rate of approximately 0.00175 in./min. (0.0445 mm/min.).

The testing machine was hydraulically driven, which means that the actual rate of loading or axial shortening rate was governed by the oil flow rate through the system. Once the desired load rate was obtained during the initial linear stage of the load-shortening behavior, no further adjustments were made to the oil flow rate of the machine until specimen failure. Accordingly, as each pile approached the first peak in the load-shortening response, the load rate decreased due to softening of the specimen.

3.7 CONCRETE MATERIAL PROPERTIES

In this research, the concrete material property of primary interest is the unconfined compressive strength. Four approaches were taken and compared to evaluate this property:

1. Compression tests were performed on 6 × 12 in. (152 × 305 mm) field cured cylinders.
2. Compression tests were performed on 6 × 11 in. (152 × 279 mm) cored cylinders.
3. Specimen PCP2 was tested in concentric axial compression.
4. The unconfined concrete compressive strength was computed from the first peak (P_1) in the axial load response of each spirally reinforced specimen.

All cylinders were prepared in plastic molds as per ASTM C-31 procedures. In order to provide ideal bearing surfaces for load application, the cylinders were capped with sulfur mortar compound according to ASTM C-617. The cylinders were tested in concentric axial compression at a displacement rate of 0.05 in./min. (1.3 mm/min.) in a 600 kip (2.70 MN) capacity universal testing machine according to ASTM C-39 procedures.

The cored cylinders were extracted from Specimen PCP1 using an electric coring machine, according to ASTM C-42. The ends of the cores were saw cut to obtain smooth and parallel faces. Each core had a diameter of 6 in. (152 mm) and was cut to a height of 11 in. (279 mm). A strength reduction factor of 0.99 was applied to the tested compressive strength to correct for the deviation from a 12 in. (305 mm) height as per ASTM C-42. As shown in Figure 3.4, four cores were removed along the height of the pile, although only three of them were tested. The cores were extracted and tested approximately two weeks after the piles were tested. Each core was capped

with sulfur mortar compound according to ASTM C-617 and tested in the same manner as the cylinders according to ASTM C-39 procedures.

The third approach used to determine the strength of the unconfined concrete was to evaluate the strength of Specimen PCP2. This specimen was tested in concentric axial compression in the 5000 kip (22.2 MN) capacity universal testing machine at the same age as the spirally reinforced piles. Specimen PCP2 was loaded at the same rate as the spirally reinforced pile specimens.

The last method employed to determine the unconfined concrete compressive strength was to compute the concrete strength from the first peak (P_1) in the load-shortening plot of the pile specimens. As explained by Graybeal et al., the unconfined concrete compressive strength can be calculated as follows:

$$f_{co} = \frac{P_1 - A_{lg} f_y}{A_{c,total}} \tag{3.1}$$

where $A_{c,total}$ is the total area of concrete in the pile cross-section. This method assumes that the longitudinal bars have yielded by the time P_1 is reached. The individual test summaries in Chapter 4 show that this is generally a good assumption.

Several factors were expected to have affected the results of the various methods used to determine the concrete compressive strength. These factors include (1) loading rate; (2) concrete curing temperature; (3) presence of voids due to bleed water effects; (4) age of concrete at the time of testing, and others. Due to these factors, some disparity in the results was expected.

Table 3.4 summarizes the results of the four approaches taken to evaluate the unconfined concrete compressive strength. The following points are noted:

1. The results from the cored cylinders show only a slight variation in concrete strength over the height of the pile. The strength difference between the top and bottom of the cored pile was 0.17 ksi (1.2 MPa), or 2 percent, which is negligible. Therefore, any bleed water effects on concrete strength were small.
2. The results from compressive tests on the cored cylinders and field-cured cylinders at the same age were in close agreement.
3. The effects of the concrete age on the compressive strength were evident. Figure 3.5 shows the variation of concrete strength over time. As expected, concrete strength increased over time, but at a consistently decreasing rate. All piles were tested over a 12 day period (ages of 79 to 91 days). The variation of strength from the piles does not seem to be attributed to the age of the concrete.
4. The effect of the loading (stress) rate was evaluated by testing field-cured cylinders at both a high stress rate of 85 psi/sec (586 kPa/sec), which corresponded to a displacement rate of 0.05 in./min (1.27 mm/min), and at a much slower stress rate of 2.5 psi/sec (17 kPa/sec), which was nearly the same stress rate to which the piles were subjected. These are the loading rates established during the initial elastic

loading of each specimen. The slower loading rate resulted in a 3% reduction in strength. It is noted that the slow tests were conducted one week after the tests with higher loading rates.

5. The unconfined concrete strengths, f_{co}, of the piles and the field-cured cylinders tested at the same age show similar results. The strength obtained from the field-cured cylinders was 3% higher than that obtained from the piles. If this difference can be attributed to the loading rate, as discussed above, then these results are in close agreement.
6. The unconfined concrete compressive strength values computed from P_1 for the six spirally reinforced piles varied within a range of 1.2 ksi (8.3 MPa). This is a much higher variation than was reported by Graybeal et al. (0.2 ksi (1.4 MPa)). Also, the unreinforced pile tested at the low end of the observed range of strengths. It is not known why this rather large disparity between specimens occurred.

Based on the results shown in Table 3.4 and the discussion presented above, f_{co} was taken to be 7.55 ksi (52.1 MPa). This value corresponds to the average strength computed from the first peak in the load-shortening response of the spirally reinforced piles. This is the same manner in which the concrete compressive strength was determined by Graybeal et al.

Finally, the same ready-mix concrete mix that was used in the work of Graybeal et al. was ordered for this research. The resulting concrete compressive strengths obtained in this study are similar to the strengths obtained by Graybeal et al. Therefore, the axial concrete strain corresponding to the unconfined concrete strength, ε_{co}, was taken as 0.0027, which was determined from compression tests by Graybeal et al.

3.8 REINFORCING STEEL MATERIAL PROPERTIES

This section discusses the key material properties of the spiral and longitudinal reinforcement used in each pile specimen. The information reported on the spiral reinforcement is a compilation of data provided by the spiral manufacturers as well as data recorded from testing performed at Lehigh University. The information relating to the longitudinal reinforcement was obtained through tension tests performed at Lehigh University.

3.8.1 Spiral Reinforcing Steel

The six different spiral reinforcement wires treated in this research were supplied to Lehigh University by three different manufacturers. The wires were delivered bent into coils with an outer diameter of 10 in. (254 mm). Four of the wires had 0.35 in. (8.89 mm) diameter circular cross-sections. These wires, denoted as A' through D', had nominal yield stresses of 78, 107, 121, and 140 ksi (538, 738, 834, 965 MPa), respectively. As noted before, these are the same materials used in the earlier work by Graybeal et al. Spiral wire E' had a nominal diameter of 0.36 in. (9.1 mm) and a reported yield stress of 195 ksi (1345 MPa). Finally, spiral wire F' had a nominal diameter of 0.43 in. (10.9 mm) diameter and a minimum reported yield stress of 185 ksi (1276 MPa). It is noted that spiral wires E' and F' were not perfectly circular in cross-section, but instead had small reductions in section formed by grooves in the wires along their lengths.

Tension tests were performed at Lehigh University to obtain stress-strain curves for each wire, and key material properties were obtained from these curves. Figure 3.6 shows the experimentally obtained stress-strain curves for each wire.

Two types of tension specimens were tested: (1) unspiraled specimens (D', E', F'); and, (2) spiraled-straightened specimens (A', B', C', D'). Each curve shown in Figure 3.6 is labeled as to the state of the wire that was tested. Results of the tension tests, along with manufacturer reported yield values, are shown in Table 3.5. Yield stress values were determined by the 0.2 percent offset method. Tension tests conducted by Graybeal et al. showed the yield stress of spiraled-straightened wires A', B', C', and D' to be 76, 102, 109, and 111 ksi (524, 703, 752, and 765 MPa), respectively, and the yield stress of the unspiraled wire D' to be 132 ksi (910 MPa). Tests conducted on unspiraled wires as part of this research showed a yield stress of 188 ksi (1296 MPa) for spiral wire E' and 193 ksi (1331 MPa) for spiral wire F'.

Of critical importance to this research was the useable stress in the spiral reinforcement. As previously discussed, the useable stress, not the nominal yield stress, was used in the design of the specimens. The useable stress corresponds to the stress in the spiral reinforcement at the second peak (P_2) of the load-shortening response of the spirally reinforced specimens. For the given parameters of pile diameter, cover distance, and concrete material properties, the useable strain was computed as 0.0062, and the useable stresses were determined at that strain.

Table 3.6 summarizes the calculations performed to arrive at the value for useable strain of 0.0062. The steps listed in this table correspond to the steps of the proposed design procedure as outlined in Figure 2.2. Given at the top of the table are the parameters that were used in the design of the piles. In Step 1, f_{c2} was calculated through Equation 2.7 to be 15.76 ksi. (108.7 MPa). In Step 2, Equation 2.8 was used to calculate $f_{2\text{-}2}$ to be 1.88 ksi (13.0 MPa). ε_{c2} was calculated in Step 3 by Equation 2.9 as 0.0158. In Step 4, ε_{ct2} was calculated through Equation 2.10 to be 0.0062. In Step 5, the use of Equation 2.11 produces a value for ε_{sp2} equal to 0.0062. This is the useable strain value used in the design of the specimens.

Figure 3.7 shows the stress-strain curves used in the design of the piles. These curves were fit to the experimental data to reduce the data from several tests into one governing relationship. The useable strain is shown in Figure 3.7 as a vertical line. The intersection of this vertical line with each stress-strain curve is the useable stress for the respective spiral steel.

Useable stress values for wires A' through D' were determined by Graybeal et al. on spiraled-straightened steel specimens and are as follows: A' = 79 ksi (545 MPa); B' = 104 ksi (717 MPa); C' = 108 ksi (745 MPa); D' = 110 ksi (758 MPa). Useable stress values for E' and F' were determined as part of this research to be 164 ksi (1131 MPa) and 161 ksi (1110 MPa), respectively. The useable stress values are presented in Table 3.5.

It is noted here that there was an unavoidable inconsistency in the approach taken to determine the useable stress values. The inconsistency is as follows: For wires A' through D', the useable stress

was determined from the spiraled-straightened curves. In contrast, for wires E' and F', the useable stress was determined from the unspiraled tension stress-strain curves. As seen in Table 3.5, for spiral wires A' through C', the data was compiled solely from tension tests performed on straightened segments of wires which had been spiraled into coils of 20 in. (508 mm) outside diameter. Unspiraled samples of these wires were not available for testing. Tension tests were performed on both spiraled-straightened segments of spiral wire D', just as in cases A'-C', and on unspiraled segments of wire. However, the data from the unspiraled case was not used in the design of the pile. Finally, tension tests were performed only on unspiraled lengths of wire for E' and F', and these curves were used to determine the useable stress. This was done because the high strengths of these wires prevented sufficient straightening of the spirals to enable tension testing. As shown in Section 2.3.4, the stress-strain curve representing the spiraled-straightened condition, as opposed to the unspiraled condition, more closely represents the in-situ stress-strain curve of the spiral wire.

3.8.2 Longitudinal Reinforcing Steel

Tension tests were conducted at Lehigh University on the #4 (0.5 in. (12.7 mm)) diameter standard longitudinal reinforcing bars. The steel was found to possess a yield stress of 71 ksi (490 MPa) and an ultimate strength of 112 ksi (772 MPa). The strain corresponding to yielding, ε_{ly} was taken as 0.00245, which is 71 ksi (490 MPa) divided by an elastic modulus of 29×10^3 ksi (20×10^4 MPa).

Pile Identification	14-A'	14-B'	14-C'	14-D'	14-E'	14-F'
Nominal Spiral Yield Stress, f_{sy} (ksi)	78	107	121	140	195	185
Spiral Useable Stress, f_{sp2} (ksi)	79	104	108	110	164	161

1 ksi = 6.895 MPa

Table 3.1 Test matrix.

Pile	Diameter (in.)	Cover (in.)	Height (in.)	f_{co} (ksi)	f_{sp2} (ksi)	ρ_{sp} %	f_{ly} (ksi)	ρ_{lg} %
14-A'	14	2	56	8.0	79	4.76	60	0.51
14-B'	14	2	56	8.0	104	3.62	60	0.51
14-C'	14	2	56	8.0	108	3.48	60	0.51
14-D'	14	2	56	8.0	110	3.42	60	0.51
14-E'	14	2	56	8.0	164	2.29	60	0.51
14-F'	14	2	56	8.0	161	2.34	60	0.51

1 ksi = 6.895 MPa
1 in. = 25.4 mm

Table 3.2 Summary of design parameters.

Pile	Spiral Reinforcement					Longitudinal Reinforcement			
	d_{sp} (in.)	n_{sp}	A_{sp} (in.^{2})	s (in.)	ρ_{sp} %	Bar Size	n_{lg}	A_{lg} (in.^{2})	ρ_{lg} %
14-A'	0.35	2	0.192	1.62	4.76	#4	4	0.79	0.51
14-B'	0.35	2	0.192	2.12	3.62	#4	4	0.79	0.51
14-C'	0.35	1	0.096	1.11	3.48	#4	4	0.79	0.51
14-D'	0.35	1	0.096	1.13	3.42	#4	4	0.79	0.51
14-E'	0.36	1	0.101	1.75	2.29	#4	4	0.79	0.51
14-F'	0.43	1	0.142	2.43	2.34	#4	4	0.79	0.51

1 in. = 25.4 mm

Table 3.3 Summary of reinforcement provided in each pile.

Age (days)	Concrete Strength (psi)			
	Cylinders ASTM Test	Cylinders Slow Test	Cores ASTM Test	Pile Test
11	5780			
11	5870			
28	6390			
28	6730			
42	6750			
42	6820			
79				6900 (A')
81				7370 (B')
81				6780 (PCP2)
84	7510			8100 (C')
84	7840			
86				7780 (D')
88				7680 (E')
91	7690			7480 (F')
91	7990			
106	8390		7860 (Core #1)	
106	7870		8040 (Core #2)	
106	8170		8030 (Core #4)	
106	7640			
113		7700		
113		7930		

1 psi = 6.895 kPa

Table 3.4 Summary of concrete compressive test results.

Spiral Steel Type	Manufacturer Reported Yield Stress (ksi)	Yield Stress from Tension Tests at Lehigh University (ksi) (0.2% offset method)		Useable Stress (ksi) at $\varepsilon_{sp2} = 0.0062$	
		Spiraled-Straightened	Unspiraled	Spiraled-Straightened	Unspiraled
A'	78	76	-	79	-
B'	107	102	-	104	-
C'	121	109	-	108	-
D'	140	111	132	110	119
E'	195	-	188	-	164
F'	185	-	193	-	161

1 ksi = 6.895 MPa

Table 3.5 Spiral reinforcing steel properties.

Given: 14 in. diameter pile; 2 in. concrete cover; 4 - #4 longitudinal bars; $f_{co} = 8.0$ ksi; $\varepsilon_{co} = 0.0027$; $f_{ly} = 60$ ksi; $A_{fy} = 0.79$ in^2			
Step	To Get:	Use Equation:	Numerical Result
1	f_{c2}	2.7	15.76 ksi
2	$f_{2\text{-}2}$	2.8	1.88 ksi
3	ε_{c2}	2.9	0.0158
4	ε_{ct2}	2.10	0.0062
5	ε_{sp2}	2.11	0.0062

1 in. = 25.4 mm
1 ksi = 6.895 MPa

Table 3.6 Summary of calculations to evaluate the useable strain, ε_{sp2}.

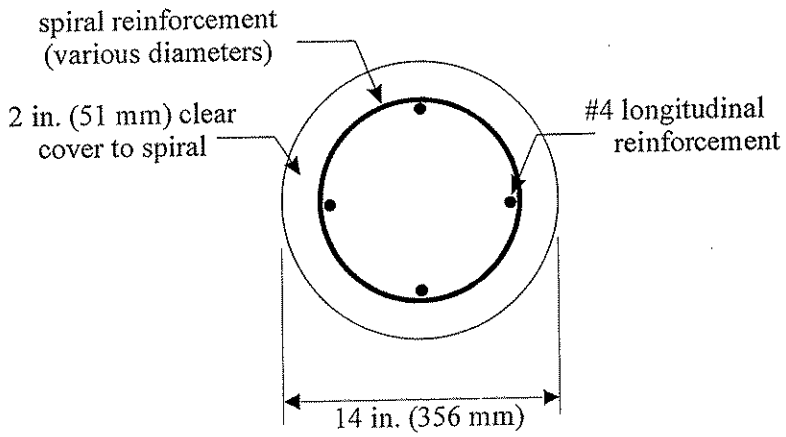

Pile	Spiral Wire Diameter
14-A'	0.35 in. (8.89 mm)
14-B'	0.35 in. (8.89 mm)
14-C'	0.35 in. (8.89 mm)
14-D'	0.35 in. (8.89 mm)
14-E'	0.36 in. (9.14 mm)
14-F'	0.43 in. (10.9 mm)

Figure 3.1 14 in. diameter pile cross-section.

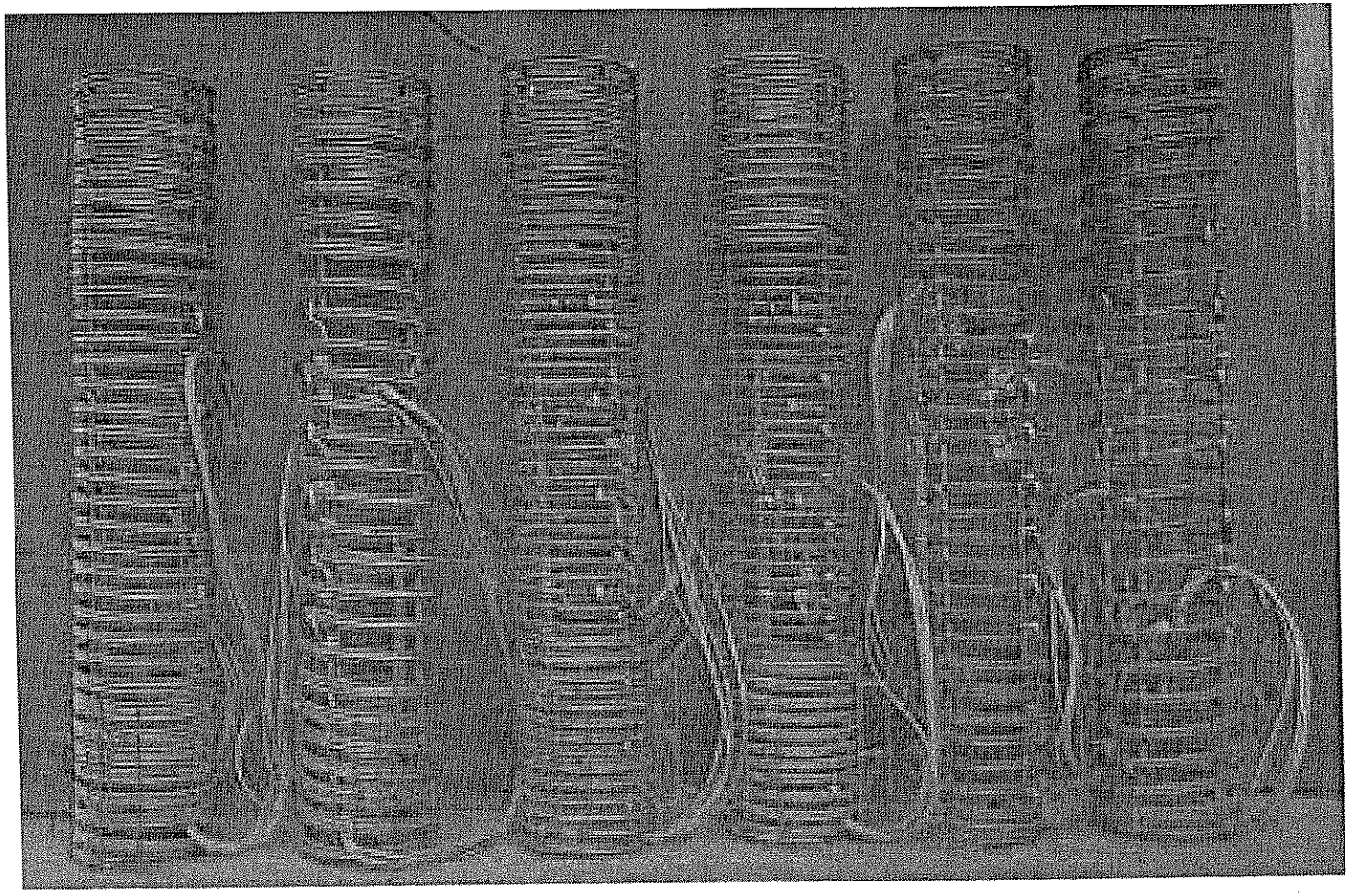

Figure 3.2 Photograph of 10 in. (254 mm) diameter reinforcing cages. Spiral wires A' - F' are shown from left to right.

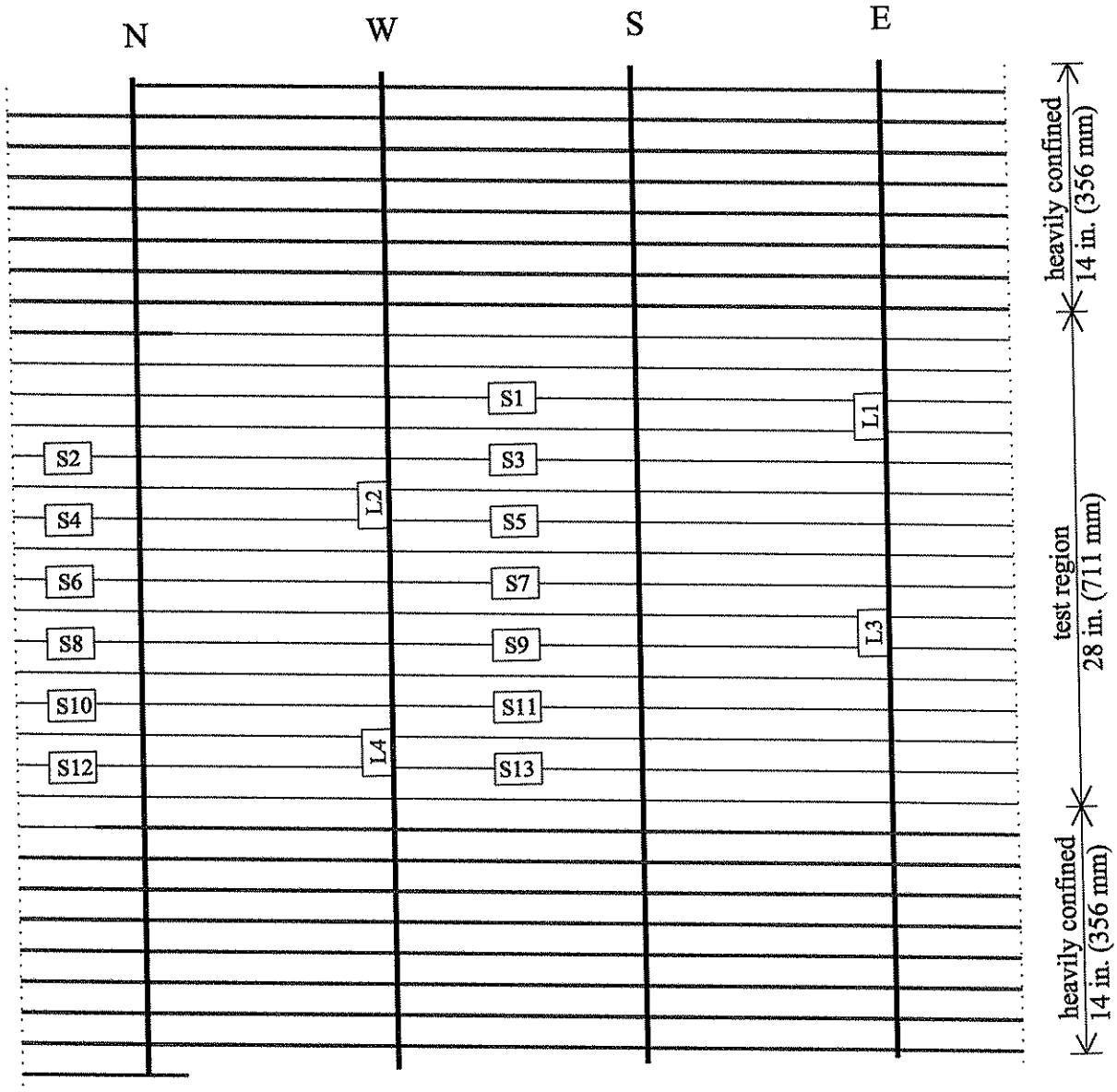

Figure 3.3 Typical pile reinforcing cage showing general layout of strain gages.

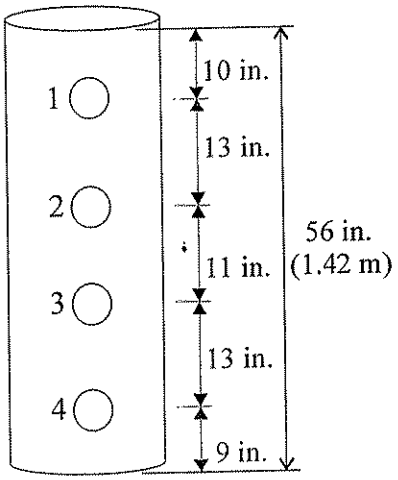

Figure 3.4 Locations at which cores were extracted from Specimen PCP1.

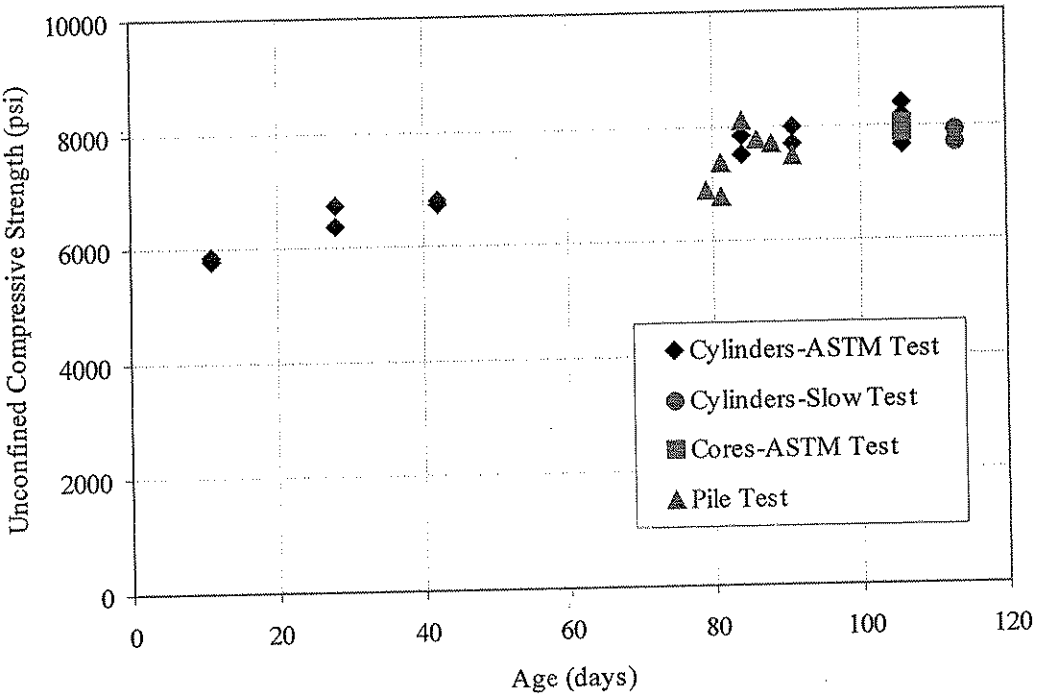

Figure 3.5 Concrete compressive strength variation over time.

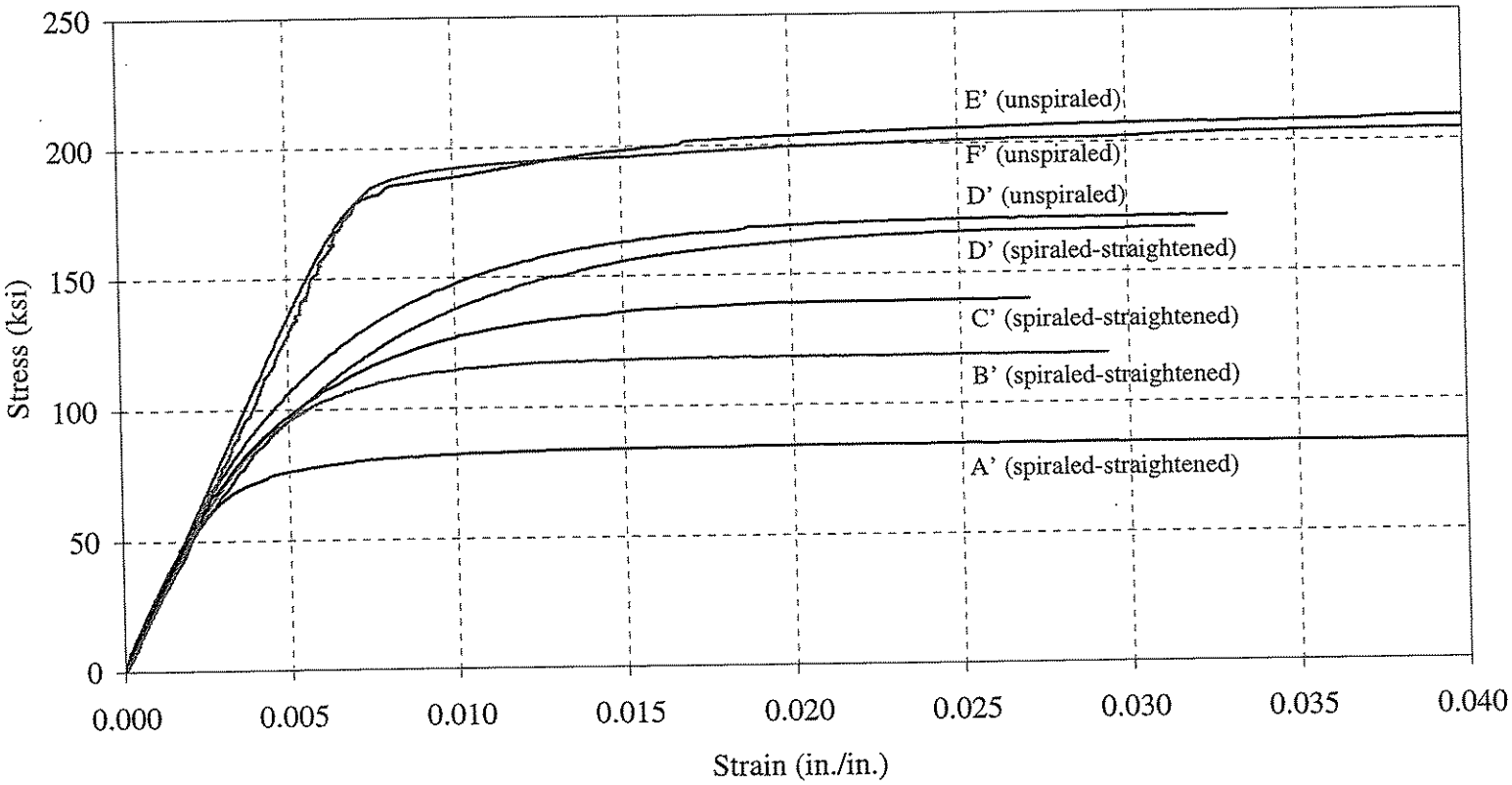

Figure 3.6 Tensile stress-strain behavior of spiral wires tested at Lehigh University.

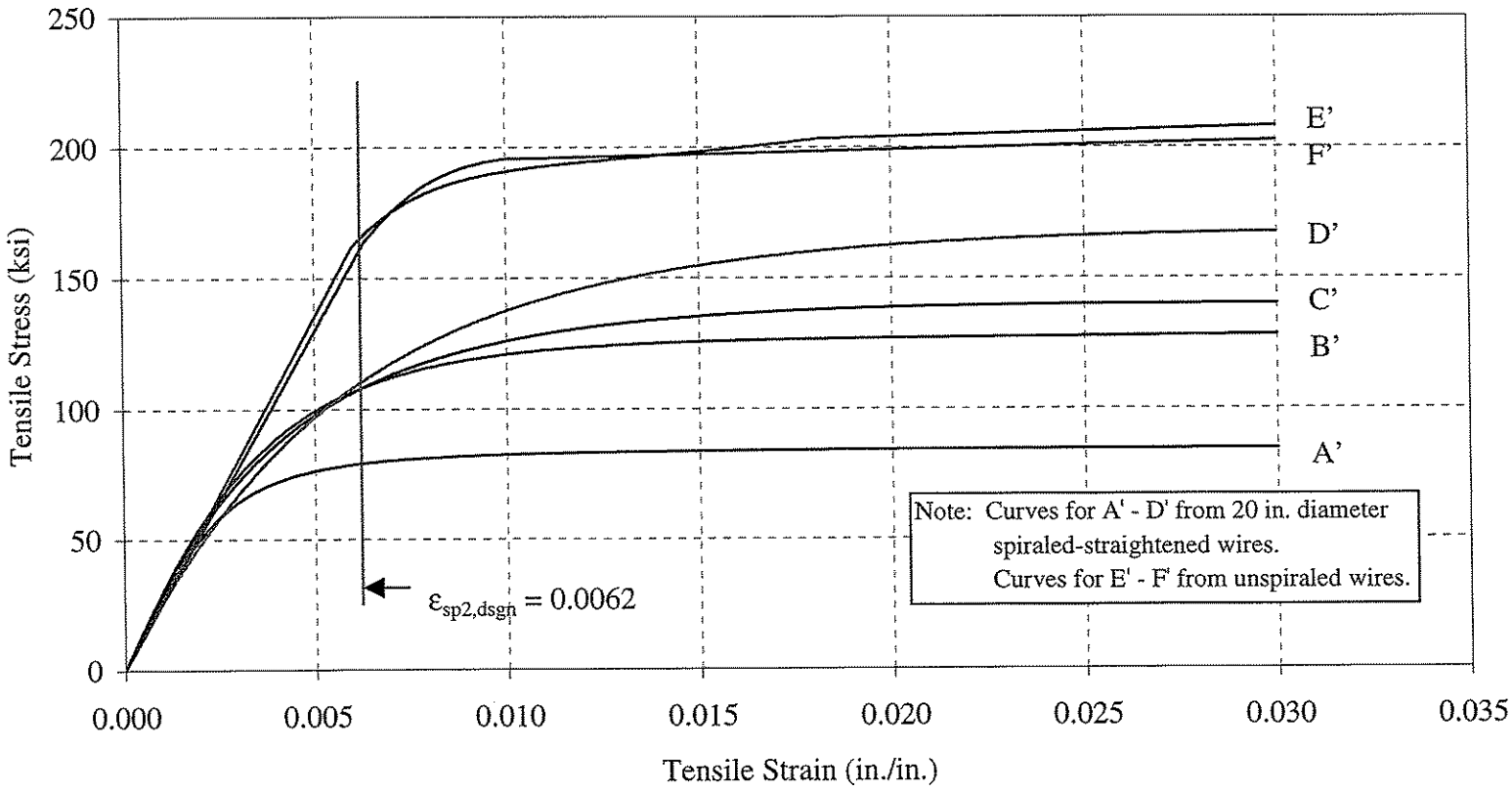

Figure 3.7 Best-fit spiral steel stress-strain curves used in the design of the pile specimens.

CHAPTER 4
EXPERIMENTAL RESULTS

4.1 INTRODUCTION

This chapter presents a detailed description of the results of the experimental program. Individual test summaries for the six 14 in. (356 mm) diameter spirally reinforced specimens are all presented using the same general format as described in Section 4.2. Section 4.3 presents the individual test summaries for the specimens.

4.2 FORMAT OF SUMMARIES

Each individual test summary is presented using the same general format:

1. A summary of the geometry and material properties that comprise the specimen.
2. A description of the behavior of the pile during the test. Included are remarks about the axial load, axial shortening, and axial strain at key stages of the response, including first peak, cover spalling, second peak, and pile failure. Axial strain values presented in the descriptions are taken as the average of the readings from the strain gages attached to the longitudinal reinforcement for that particular point in the response.
3. A plot of axial load versus axial shortening. The axial shortening value is taken as the reading from the LVDT mounted closest to the specimen during testing. As previously mentioned in earlier sections, P_1, P_{spall}, P_2, and $P_{failure}$ indicate the load at the first peak, after cover spalling, at the second peak, and at pile failure, respectively.
4. A plot of the strain in the spiral reinforcement versus the axial shortening. The spiral strain values are the strains in the spiral reinforcement as recorded by the strain gages which were attached to the spiral wires during the reinforcement cage fabrication.
5. A plot of the strain in the longitudinal reinforcement versus the axial shortening. The longitudinal strain values are the strains in the longitudinal steel as recorded by the strain gages which were applied to the longitudinal bars during the reinforcement cage fabrication. The average longitudinal strain at each increment of axial shortening is also shown on the plot. This average value curve was truncated as soon as the average value was significantly affected due to failure of one or more of the gages.
6. A schematic drawing which shows the post-test appearance of the pile. Noted in this sketch are locations of spiral necking and fractures and other distinct features related to how the specimen failed.
7. Photographs that show the pile after the completion of the test.

4.3 INDIVIDUAL TEST SUMMARIES

4.3.1 Pile 14-A'

Pile 14-A' had an unconfined concrete compressive strength of 7.55 ksi (52.1 MPa). The spiral reinforcement had a design useable stress of 79 ksi (545 MPa) and manufacturer reported nominal yield and ultimate strengths of 78 ksi (538 MPa) and 84 ksi (579 MPa), respectively. The spiral reinforcement was comprised of two 0.35 in. (8.89 mm) diameter smooth wires bundled together at a pitch of 1.62 in. (41.1 mm). The longitudinal reinforcement consisted of four 0.5 in. (12.7 mm) diameter standard deformed steel reinforcing bars spaced evenly around the perimeter of the confined concrete core. The longitudinal reinforcement had a yield stress of 71 ksi (490 MPa).

The axial load versus axial shortening response of Specimen 14-A' is plotted in Figure 4.1. The specimen reached the first peak load of $P_1 = 1113$ kips (4.95 MN) at an overall axial shortening of $\Delta_1 = 0.137$ in. (3.48 mm). The corresponding axial strain was 0.0022. At this load, the concrete cover exhibited significant damage, but did not fail completely. Figure 4.1 shows that the cover failed in two main events.

Prior to cover failure, few, if any, cracks were observed in the cover concrete. At cover failure, visible damage to the cover concrete was apparent circumferentially around the test region. Longitudinal cracks also formed, extending from the circumferential splitting toward the top and bottom of the pile. The loss of cover concrete caused the load to drop to $P_{spall} = 876$ kips (3.90 MN).

The specimen exhibited considerably less axial stiffness after the loss of the concrete cover. This behavior is evidenced by the shallower slope of the axial load-axial shortening plot in Figure 4.1 after P_{spall}. The specimen achieved its second peak at an axial load of $P_2 = 1245$ kips (5.54 MN) and at an axial shortening of $\Delta_2 = 0.876$ in. (22.25 mm). The axial strain was 0.0153.

After reaching the second peak in the load-shortening response, the specimen continued to shorten while the load decreased until failure occurred at a load of $P_{failure} = 1031$ kips (4.59 MN) and an axial shortening of 1.277 in. (32.44 mm). In this research, failure was defined as the fracture of one or more spirals.

Figure 4.2 shows the strain in the spiral reinforcement plotted versus the axial shortening. Each channel was plotted up to the point in the test at which the strain gage failed. The displacements at the first peak and second peak in the load-shortening response are indicated in Figure 4.2 by Δ_1 and Δ_2, respectively.

Figure 4.3 shows the strain in the longitudinal reinforcement plotted versus the axial shortening. Just as in Figure 4.2, the displacements at the first peak and second peak in the load-shortening response are indicated by Δ_1 and Δ_2, respectively. In addition, the yield strain in the longitudinal reinforcement is indicated in Figure 4.3. Figure 4.3 shows that, on average, the stress in the longitudinal reinforcement was slightly below its yield value when Δ_1 was reached.

Figure 4.4 presents a schematic drawing of the failed pile. The spiral fractures occurred in two bundles in the southeast face of the specimen. Three bundles of spirals were observed to have undergone necking at the same location. No clearly observable failure plane was detected in the concrete core. However, the pattern of damage to the spiral reinforcement corresponded to a plane of approximately 43° from the horizontal in the southeast face. Buckling of the longitudinal reinforcement was detected in one location along the south bar at the location of fractured spirals.

Figure 4.5 shows two post-test photographs of the failed specimen with most of the concrete cover removed. The concrete cover had completely spalled away from the core and remained attached to the specimen only through the tie wires embedded in the cover concrete. An overall view of the failed pile is illustrated in part (a). Figure 4.5 (b) is a close-up view of the fractured spiral reinforcement around the south longitudinal reinforcing bar.

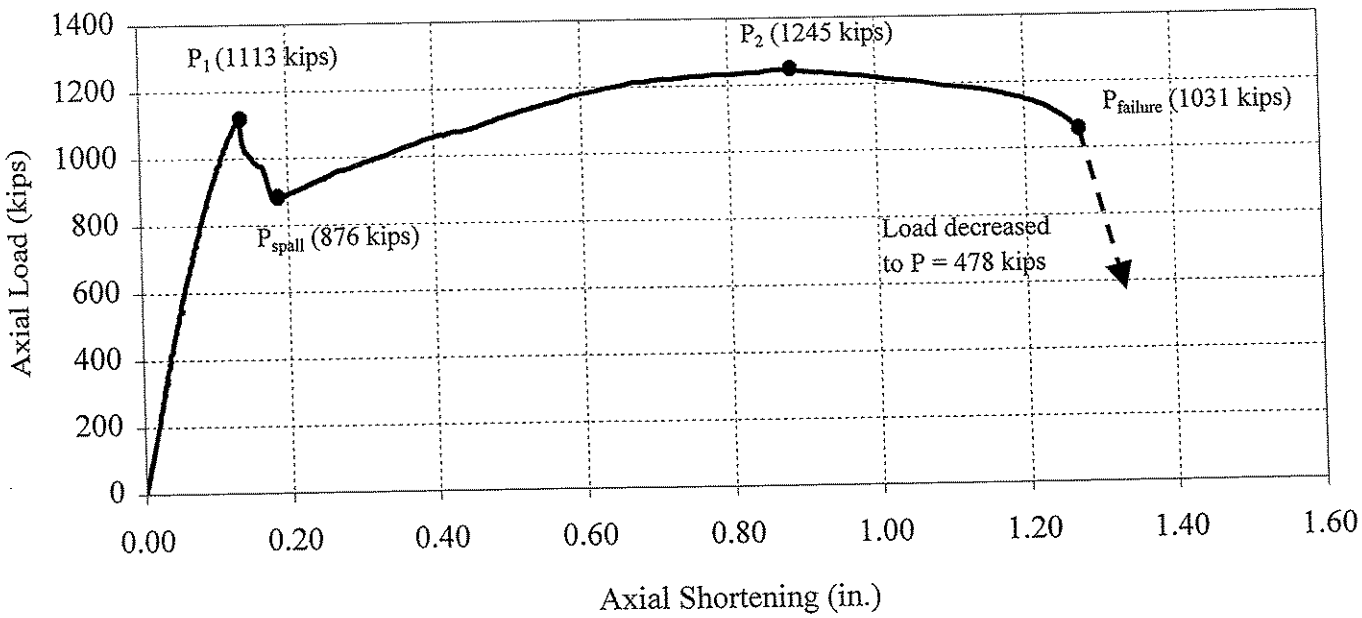

Figure 4.1 Plot of axial load versus axial shortening for Specimen 14-A'.

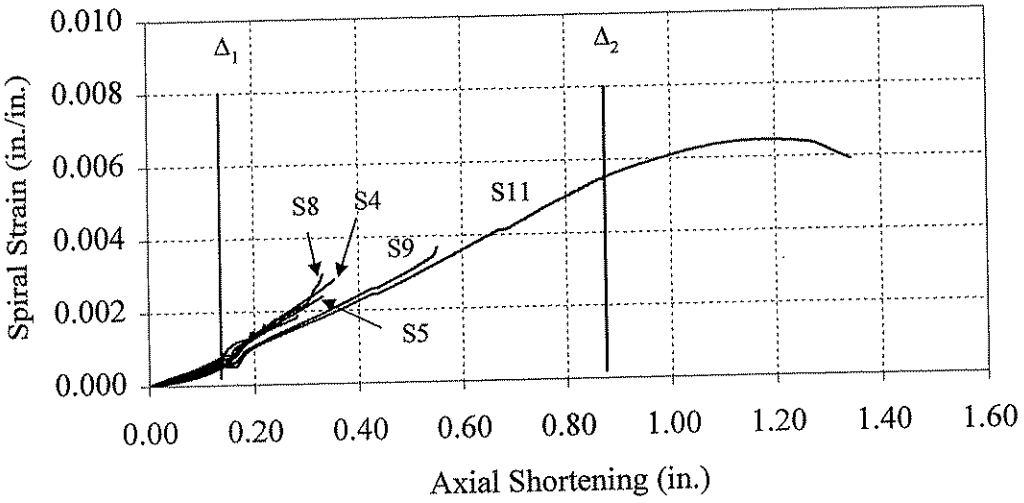

Figure 4.2 Plot of spiral strain versus axial shortening for Specimen 14-A'.

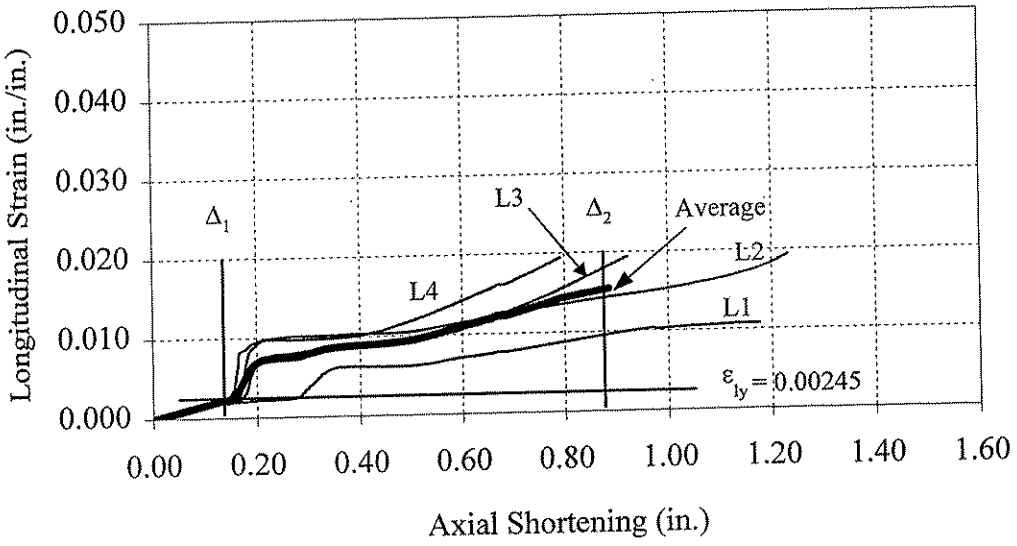

Figure 4.3 Plot of longitudinal strain versus axial shortening for Specimen 14-A'.

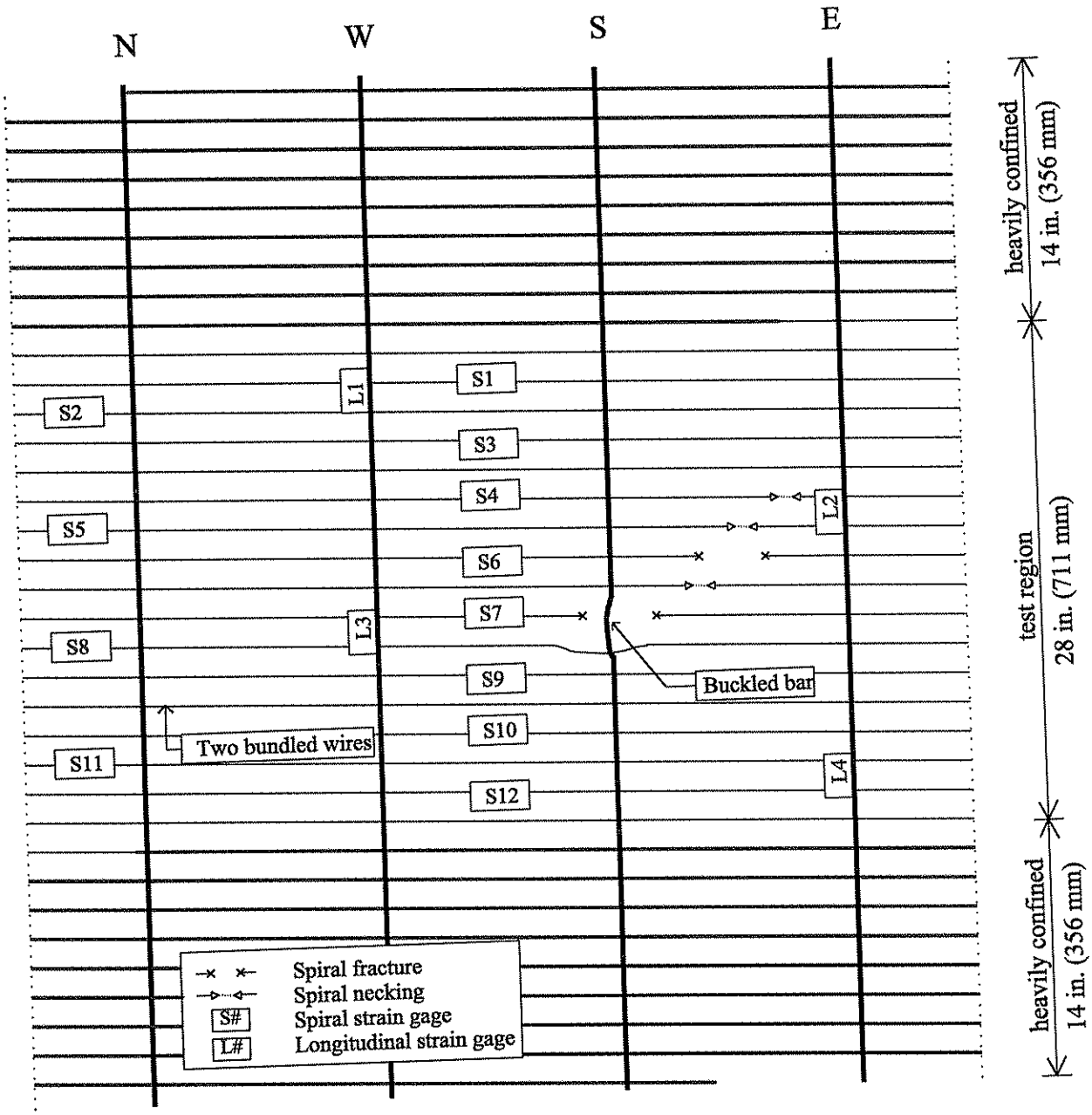

Figure 4.4 Schematic drawing of post-test appearance of Specimen 14-A'.

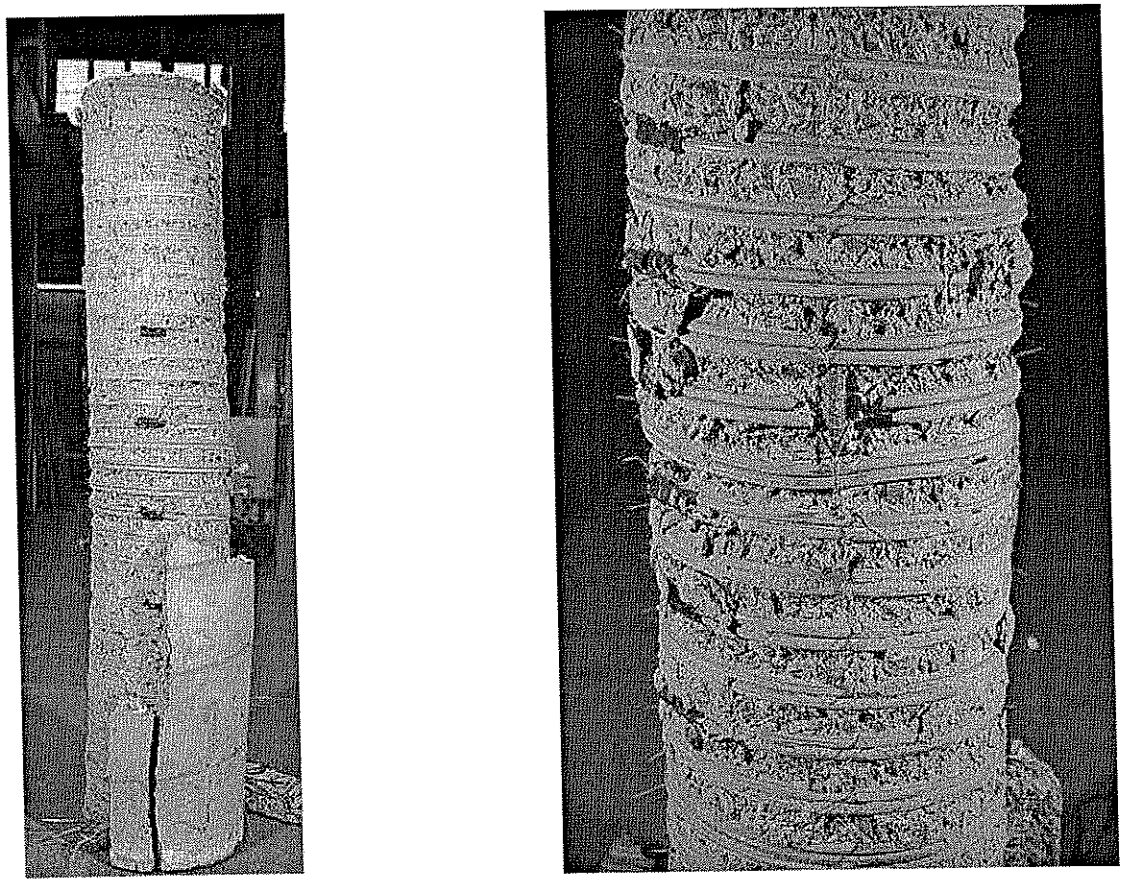

(a) (b)

Figure 4.5 Post-test photographs of Specimen 14-A': (a) overall view; (b) south face.

4.3.2 Pile 14-B'

Pile 14-B' had an unconfined concrete compressive strength of 7.55 ksi (52.1 MPa). The spiral reinforcement had a design useable stress of 104 ksi (717 MPa) and manufacturer reported nominal yield and ultimate strengths of 107 ksi (738 MPa) and 116 ksi (800 MPa), respectively. The spiral reinforcement was comprised of two 0.35 in. (8.89 mm) diameter smooth wires bundled together at a pitch of 2.12 in. (53.8 mm). The longitudinal reinforcement consisted of four 0.5 in. (12.7 mm) diameter standard deformed steel reinforcing bars spaced evenly around the perimeter of the confined concrete core. The longitudinal reinforcement had a yield stress of 71 ksi (490 MPa).

The axial load versus axial shortening response of Specimen 14-B' is plotted in Figure 4.6 up to P_{spall}. The specimen reached the first peak load of P_1 = 1185 kips (5.27 MN) at an overall axial shortening of Δ_1 = 0.147 in. (3.73 mm). The corresponding axial strain was 0.0042. At this load, the concrete cover failed in a sudden manner.

Prior to cover failure, few, if any, cracks were observed in the cover concrete. At cover failure, visible damage to the cover concrete was apparent circumferentially around the test region. Longitudinal cracks also formed, extending from the circumferential splitting toward the top and bottom of the pile. The loss of cover concrete caused the load to drop to P_{spall} = 809 kips (3.60 MN).

As shown in the post-test photographs (Figure 4.9), Specimen 14-B' failed in an unintended manner in the heavily confined region at the top end of the specimen. This failure occurred after the loss of the concrete cover, i.e. after P_1. Failure was attributed to inadequate anchorage of the spiral reinforcement. Basically, the spiral opened up and the core concrete failed in unconfined compression. Thus, the results of this test are invalid. Accordingly, the results presented here are limited to that part of the test extending to spalling of the concrete cover, and the results of this specimen are largely ignored in the discussions in subsequent chapters.

Figure 4.7 shows the strain in the spiral reinforcement plotted versus the axial shortening up to P_{spall}. Each channel was plotted up to the point in the test at which the strain gage failed. The displacement at the first peak is indicated in Figure 4.7 by Δ_1.

Figure 4.8 shows the strain in the longitudinal reinforcement plotted versus the axial shortening. Just as in Figure 4.7, the displacement at the first peak in the load-shortening response is indicated by Δ_1. In addition, the yield strain in the longitudinal reinforcement is indicated in Figure 4.8. Figure 4.8 shows that, on average, the longitudinal reinforcement had achieved its yield value by the time Δ_1 was reached.

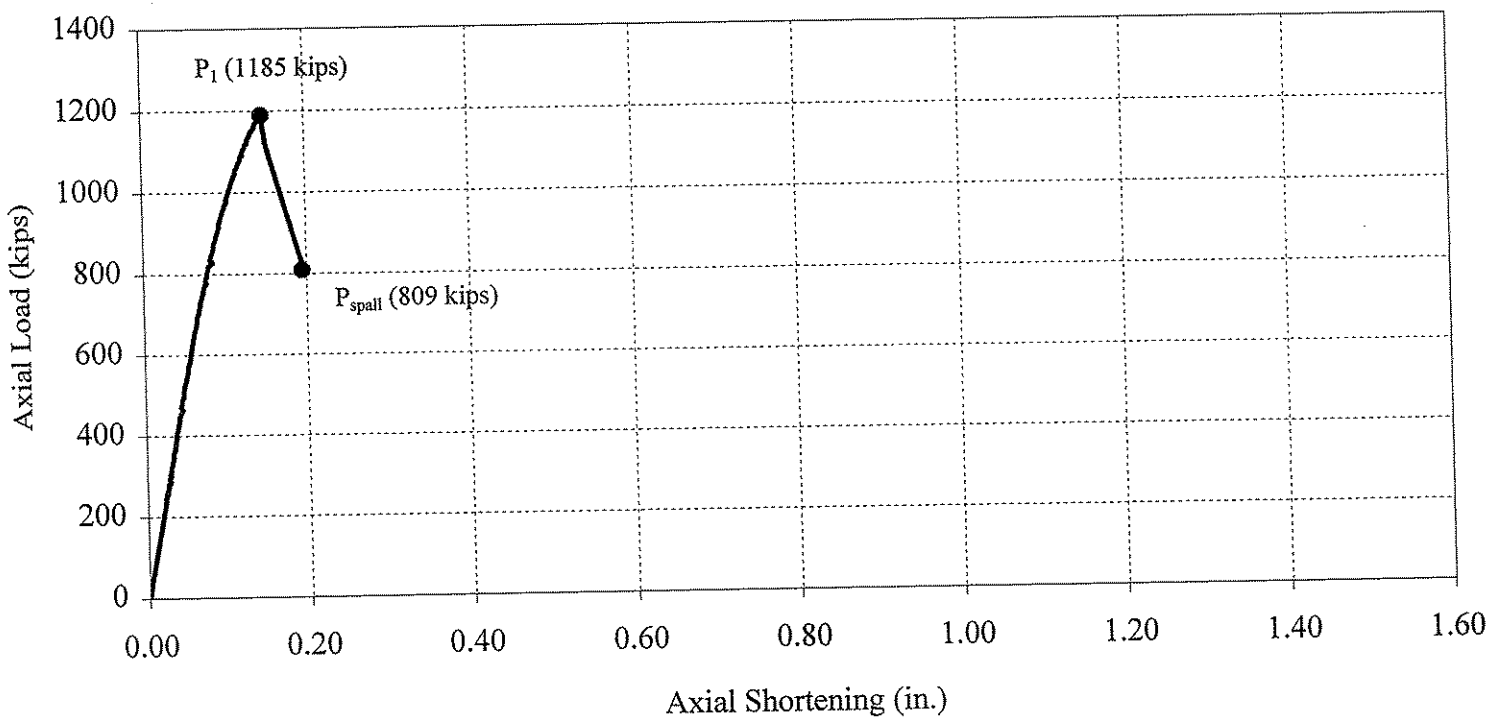

Figure 4.6 Plot of axial load versus axial shortening for Specimen 14-B'.

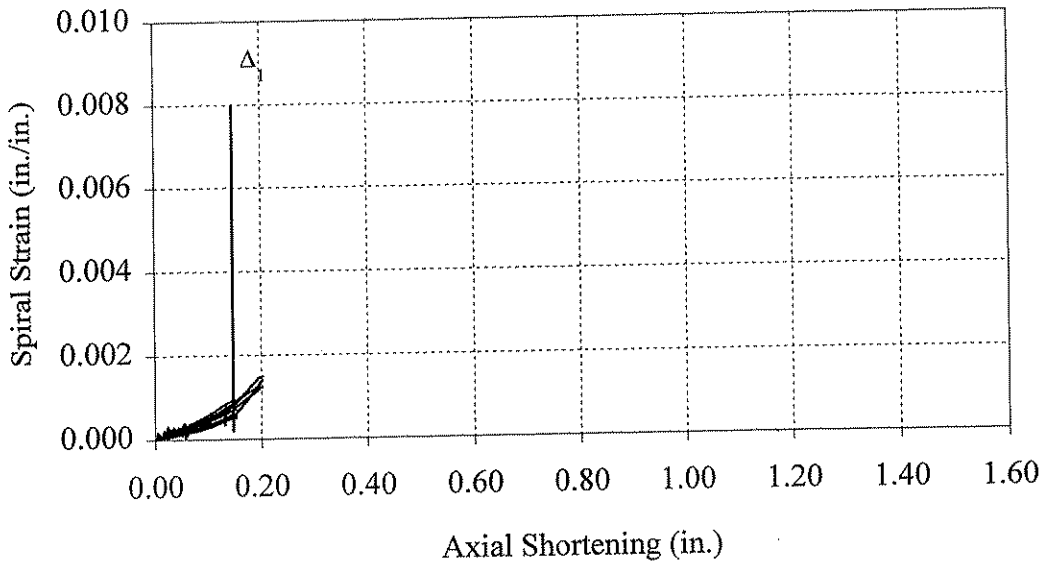

Figure 4.7 Plot of spiral strain versus axial shortening for Specimen 14-B'.

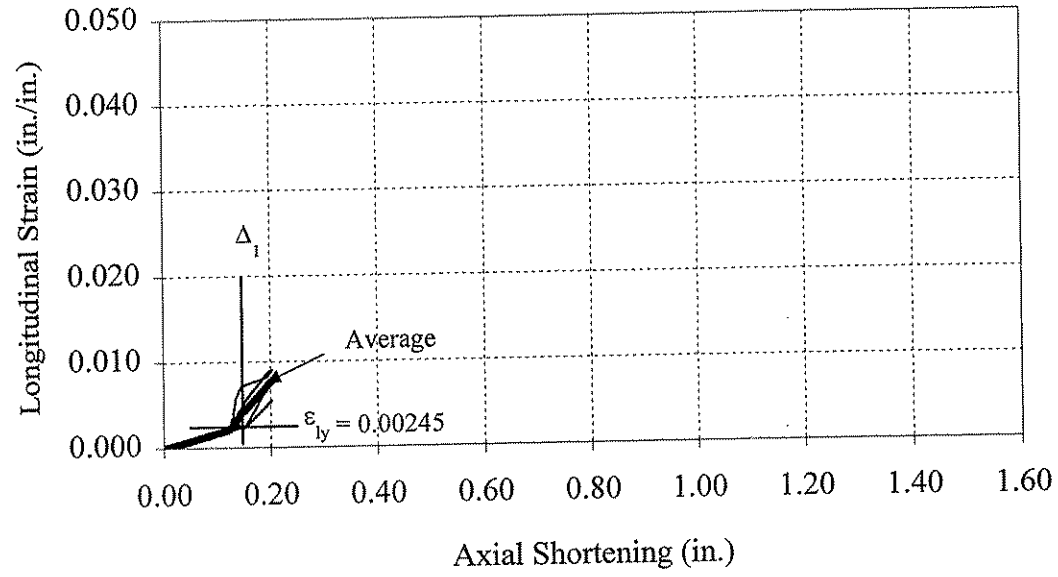

Figure 4.8 Plot of longitudinal strain versus axial shortening for Specimen 14-B'.

(a) (b)

Figure 4.9 Post-test photographs of Specimen 14-B': (a) overall view; (b) top of specimen.

4.3.3 Pile 14-C'

Pile 14-C' had an unconfined concrete compressive strength of 7.55 ksi (52.1 MPa). The spiral reinforcement had a design useable stress of 108 ksi (745 MPa) and manufacturer reported nominal yield and ultimate strengths of 121 ksi (834 MPa) and 143 ksi (986 ksi), respectively. The spiral reinforcement was comprised of one 0.35 in. (8.89 mm) diameter smooth wire at a pitch of 1.11 in. (28.2 mm). The longitudinal reinforcement consisted of four 0.5 in. (12.7 mm) diameter standard deformed steel reinforcing bars spaced evenly around the perimeter of the confined concrete core. The longitudinal reinforcement had a yield stress of 71 ksi (490 MPa).

The axial load versus axial shortening response of Specimen 14-C' is plotted in Figure 4.10. The specimen reached the first peak load of $P_1 = 1296$ kips (5.76 MN) at an overall axial shortening of $\Delta_1 = 0.197$ in. (5.00 mm). The corresponding axial strain was 0.0073. At this load, the concrete cover failed in a sudden manner.

Prior to cover failure, few, if any, cracks were observed in the cover concrete. At cover failure, visible damage to the cover concrete was apparent circumferentially around the test region. Longitudinal cracks also formed, extending from the circumferential splitting toward the top and bottom of the pile. The loss of cover concrete caused the load to drop to $P_{spall} = 898$ kips (3.99 MN).

The specimen exhibited considerably less axial stiffness after the loss of the concrete cover. This behavior is evidenced by the shallower slope of the axial load-axial shortening plot in Figure 4.10 after P_{spall}. The specimen achieved its second peak at an axial load of $P_2 = 1250$ kips (5.56 MN) and at an axial shortening of 0.943 in. (23.95 mm). The axial strain was 0.0219.

After reaching the second peak in the load-shortening response, the specimen continued to shorten while the load decreased until failure occurred by fracture of the spiral reinforcement at a load of $P_{failure} = 1046$ kips (4.65 MN) and an axial shortening of 1.316 in. (33.43 mm).

Figure 4.11 shows the strain in the spiral reinforcement plotted versus the axial shortening. The displacements at P_1 and P_2 are indicated in Figure 4.11 by Δ_1 and Δ_2, respectively.

Figure 4.12 shows the strain in the longitudinal reinforcement plotted versus the axial shortening. Just as in Figure 4.11, the displacements at P_1 and P_2 are indicated by Δ_1 and Δ_2, respectively. Figure 4.12 shows that, on average, the longitudinal reinforcement had achieved its yield value by the time Δ_1 was reached.

Figure 4.13 presents a schematic diagram of the failed pile. Spiral fractures were observed in two wires, and necking was observed in one wire. These effects were primarily detected in the southeast face of the pile. Buckling was observed in each longitudinal reinforcing bar. No failure plane was observed in the concrete core.

Figure 4.14 shows two post-test photographs of the failed specimen. Figure 4.14(a) presents an overall view of the failed pile. Figure 4.14(b) is a close-up view of a failure region on the southeastern face of the specimen. This figure shows well that the spiral steel failed in a ductile manner, as evidenced by the cup and cone appearance of the fractured ends of the spiral wire.

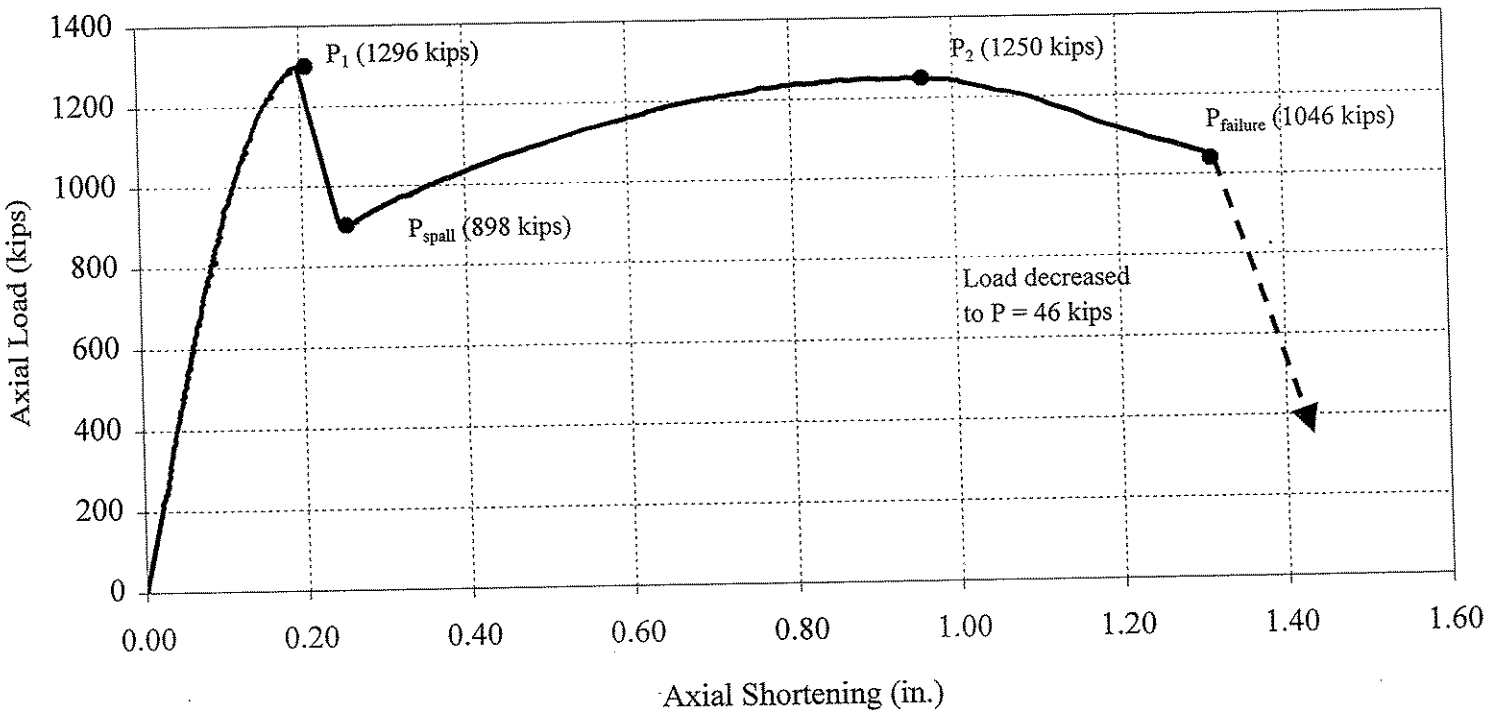

Figure 4.10 Plot of axial load versus axial shortening for Specimen 14-C'.

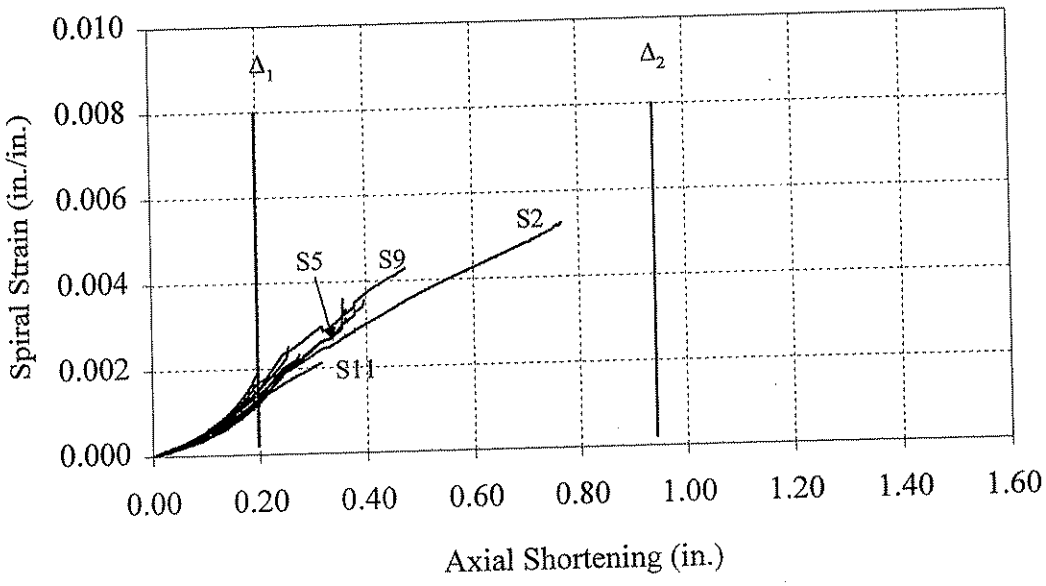

Figure 4.11 Plot of spiral strain versus axial shortening for Specimen 14-C'.

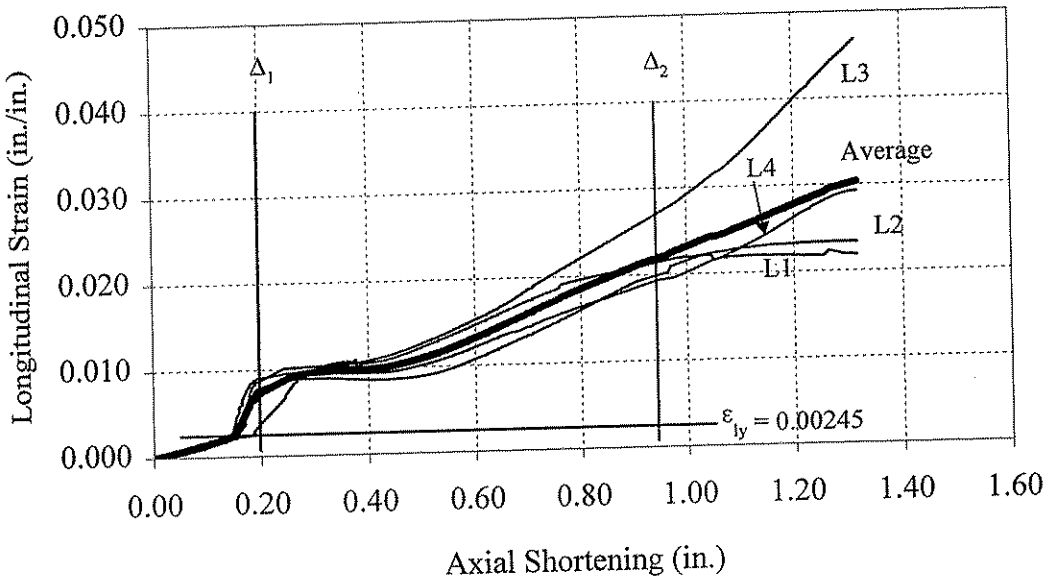

Figure 4.12 Plot of longitudinal strain versus axial shortening for Specimen 14-C'.

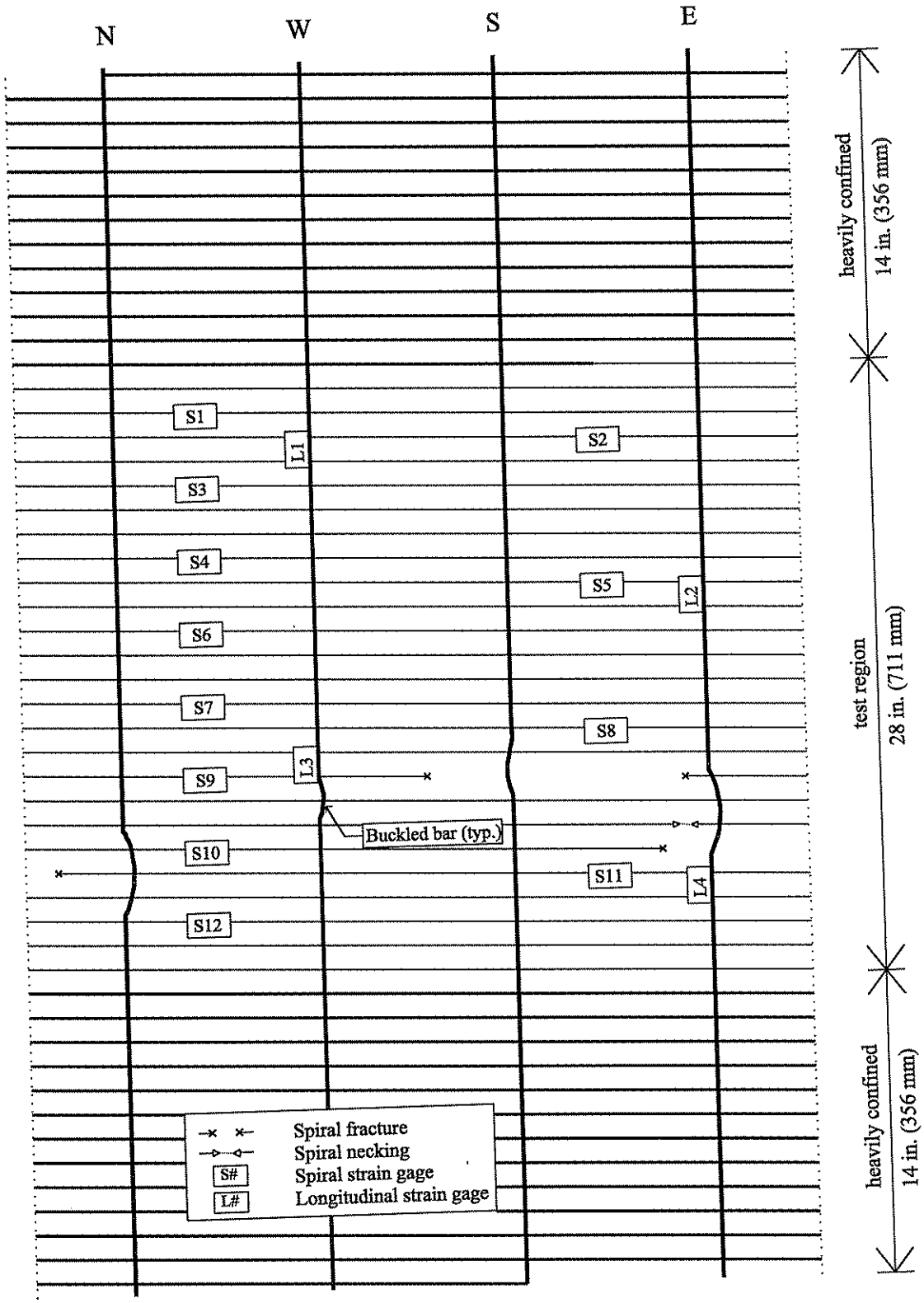

Figure 4.13 Schematic drawing of post-test appearance of Specimen 14-C'.

(a) (b)

Figure 4.14 Post-test photographs of Specimen 14-C': (a) overall view; (b) southeast face.

4.3.4 Pile 14-D'

Pile 14-D' had an unconfined concrete compressive strength of 7.55 ksi (52.1 MPa). The spiral reinforcement had a design useable stress of 110 ksi (758 MPa) and manufacturer reported nominal yield and ultimate strengths of 140 ksi (965 MPa) and 174 ksi (1200 MPa), respectively. The spiral reinforcement was comprised of one 0.35 in. (8.89 mm) diameter smooth wire at a pitch of 1.13 in. (28.7 mm). The longitudinal reinforcement consisted of four 0.5 in. (12.7 mm) diameter standard deformed steel reinforcing bars spaced evenly around the perimeter of the confined concrete core with a yield stress of 71 ksi (490 MPa).

The axial load versus axial shortening response of Specimen 14-D' is plotted in Figure 4.15. The specimen reached the first peak load of $P_1 = 1248$ kips (5.55 MN) at an overall axial shortening of $\Delta_1 = 0.165$ in. (4.19 mm). The corresponding axial strain was 0.0026. At this load, the concrete cover failed in a sudden manner.

Similar to the previous specimens, few, if any, cracks were observed in the cover concrete prior to cover failure. At cover failure, visible damage to the cover concrete was apparent circumferentially around the test region. Longitudinal cracks also formed, extending from the circumferential splitting toward the top and bottom of the pile. The loss of cover concrete caused the load to drop to $P_{spall} = 898$ kips (3.99 MN).

Again, similar to the previous specimens, Specimen 14-D' exhibited considerably less axial stiffness after the loss of the concrete cover, as evidenced by the shallower slope of the axial load-axial shortening plot in Figure 4.15 after P_{spall}. The specimen achieved its second peak at an axial load of $P_2 = 1328$ kips (5.91 MN) and at an axial shortening of 1.134 in. (28.80 mm). The axial strain was 0.0344.

After reaching the second peak in the load-shortening response, the specimen continued to shorten while the load decreased until failure occurred at a load of $P_{failure} = 1260$ kips (5.60 MN) and an axial shortening of 1.537 in. (39.04 mm).

Figure 4.16 shows the strain in the spiral reinforcement plotted versus the axial shortening. Each channel was plotted up to the point in the test at which the strain gage failed. The displacements at P_1 and P_2 in the load-shortening response are indicated in Figure 4.16 by Δ_1 and Δ_2, respectively. All spiral gages failed well before the achievement of Δ_2.

Figure 4.17 shows the strain in the longitudinal reinforcement plotted versus the axial shortening. Just as in Figure 4.16, the displacements at P_1 and P_2 in the load-shortening response are indicated by Δ_1 and Δ_2, respectively. Figure 4.17 shows that, on average, the longitudinal reinforcement was near its yield value when Δ_1 was reached. During the test, gage L3 reached its maximum output value before Δ_2 was achieved. After gage L3 reached its peak output, the average value curve was computed using this constant maximum value for L3.

Figure 4.18 presents a schematic drawing of the post-test condition of Pile 14-D'. The appearance of the failed pile showed only one spiral fracture around the west longitudinal reinforcing bar near the midheight of the specimen. No necking of any spiral wires was detected during the visual inspection. Buckling was observed in three of the four longitudinal reinforcing bars. No failure plane was detected in the concrete core.

Figure 4.19 shows two post-test photographs of the failed specimen. An overall view of the failed pile is presented in Figure 4.19(a). Figure 4.19(b) highlights the failure region on the west side of the specimen.

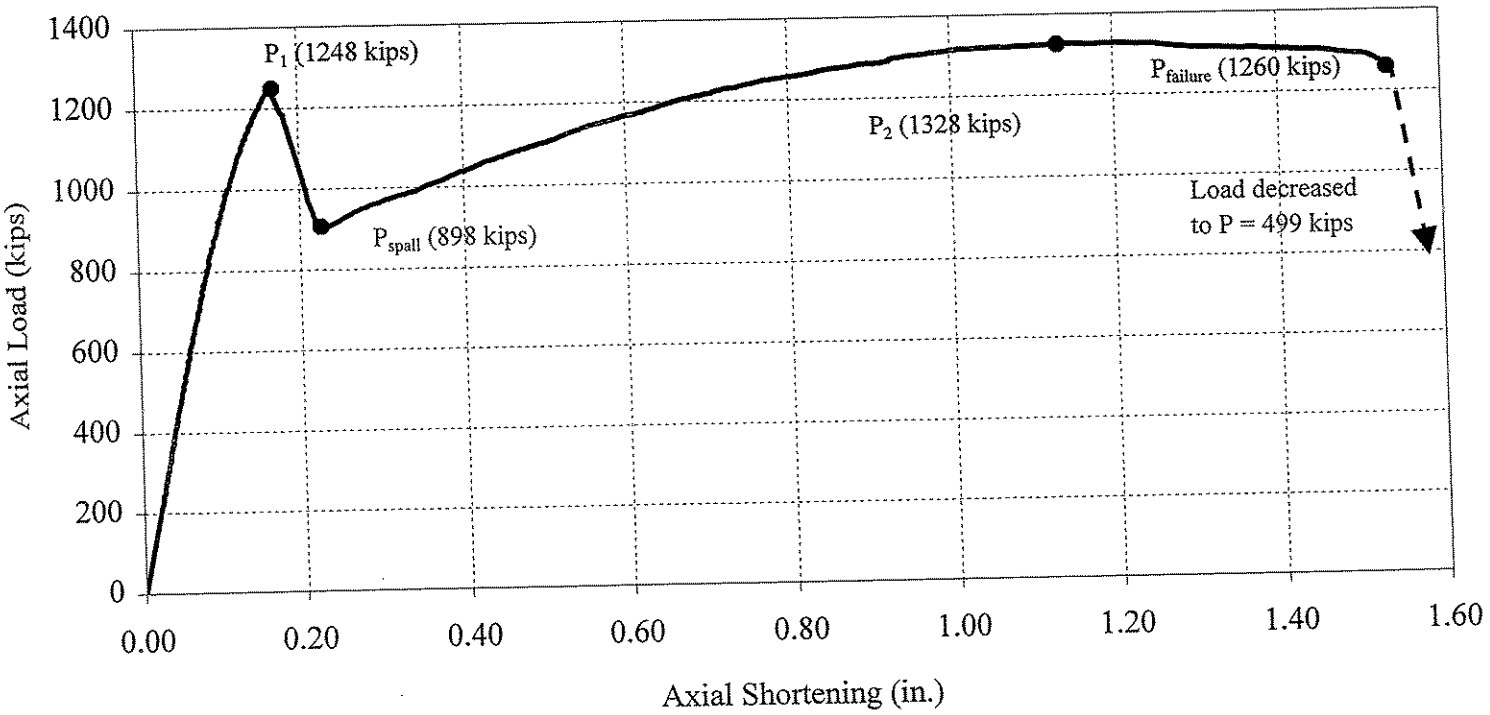

Figure 4.15 Plot of axial load versus axial shortening for Specimen 14-D'.

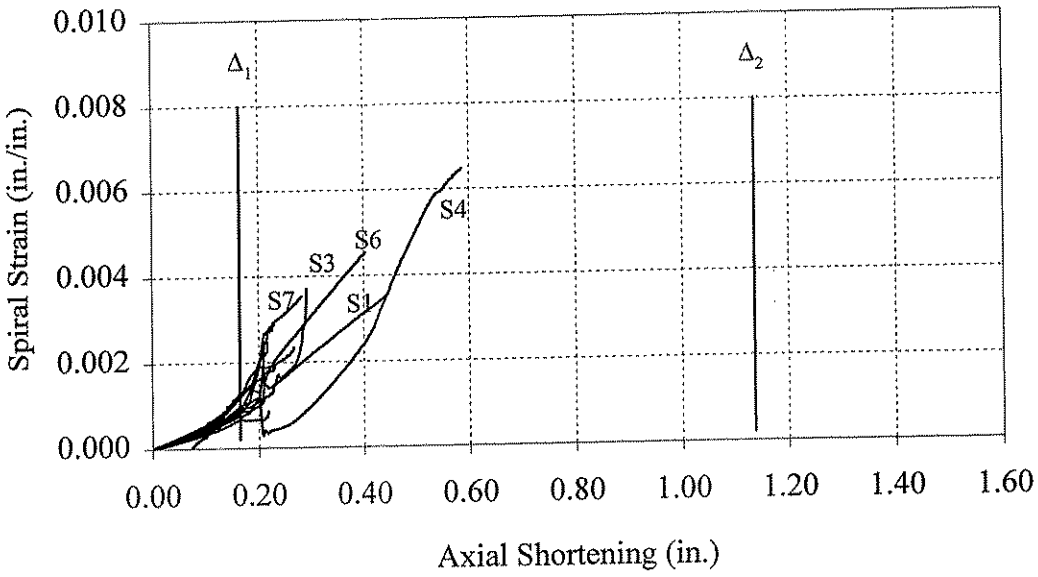

Figure 4.16 Plot of spiral strain versus axial shortening for Specimen 14-D'.

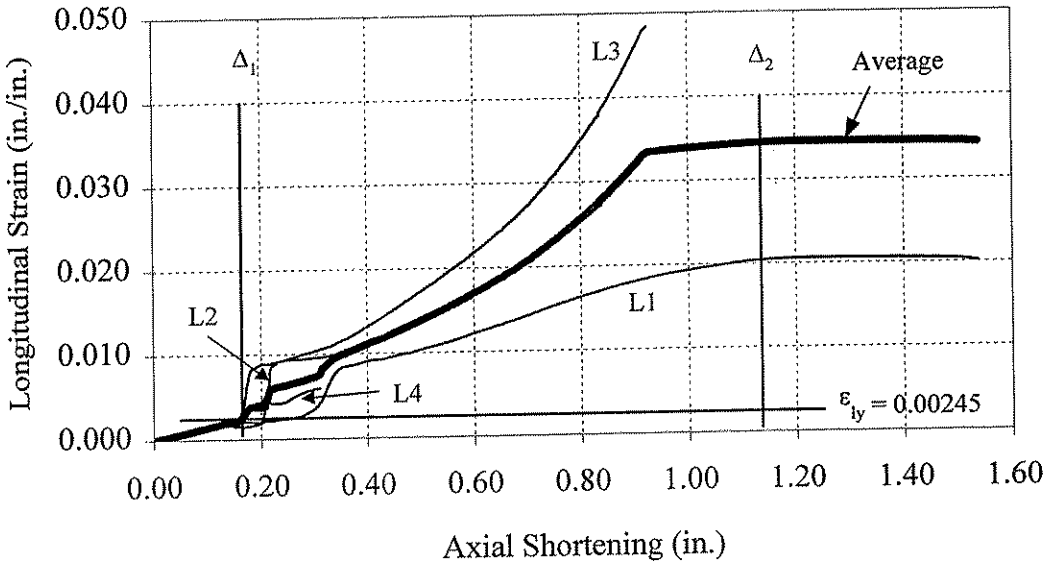

Figure 4.17 Plot of longitudinal strain versus axial shortening for Specimen 14-D'.

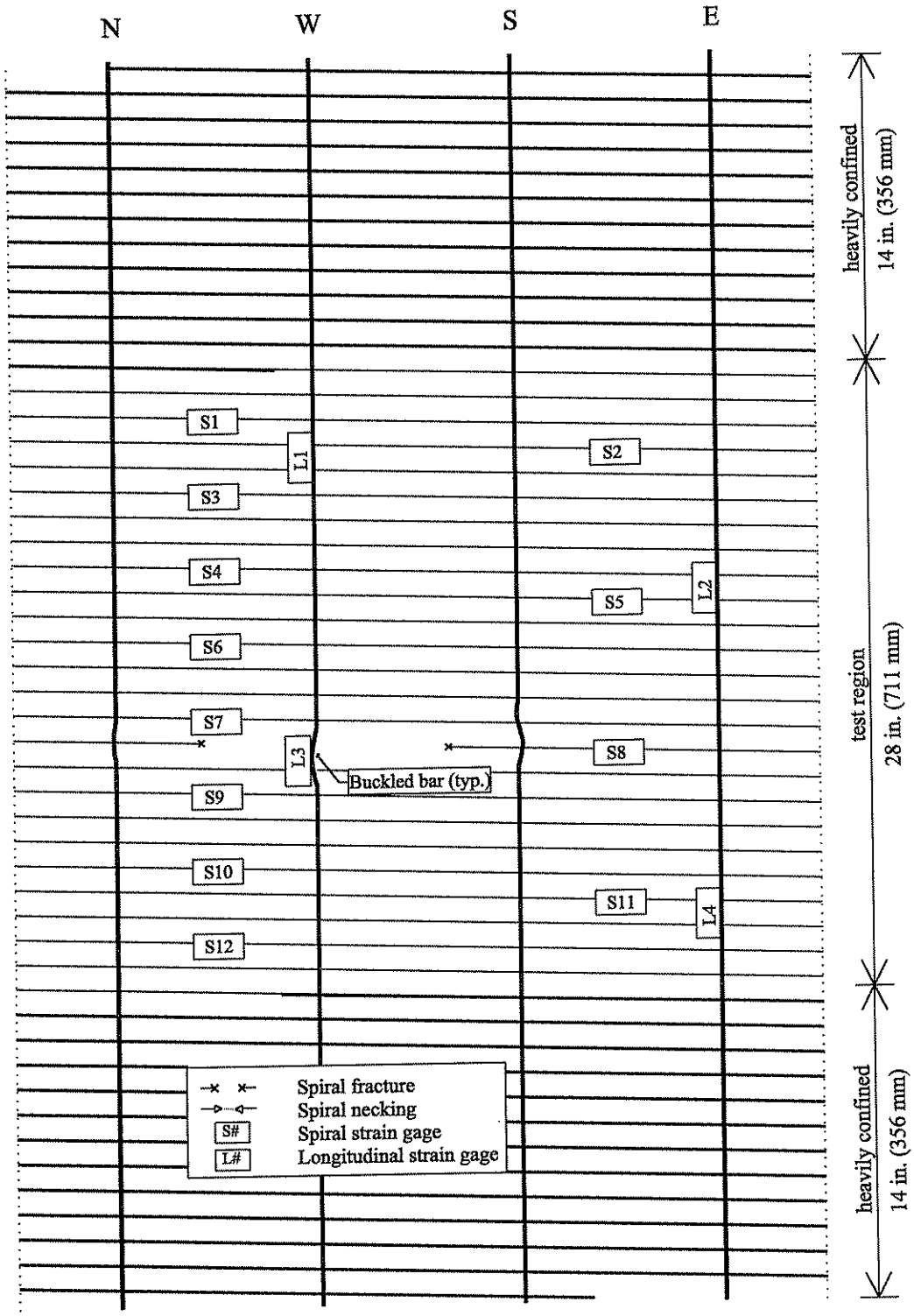

Figure 4.18 Schematic drawing of post-test appearance of Specimen 14-D'.

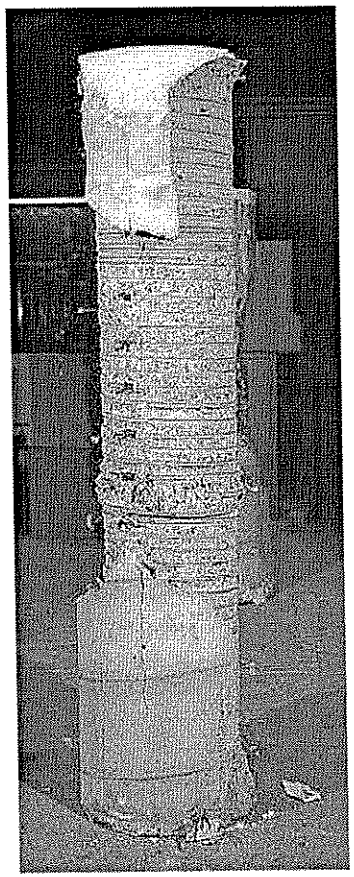

(a)

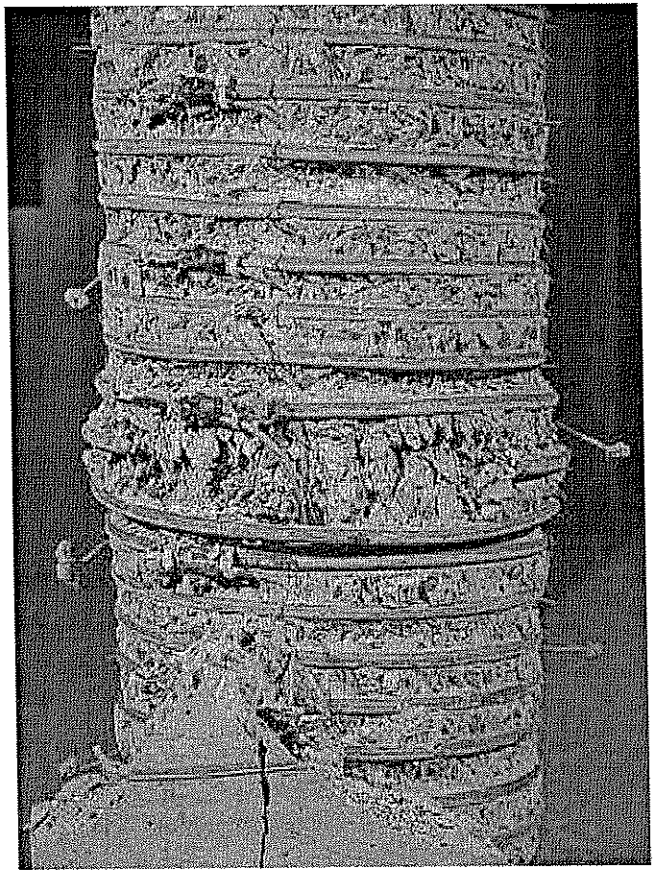

(b)

Figure 4.19 Post-test photographs of Specimen 14-D': (a) overall view; (b) west face.

4.3.5 Pile 14-E'

Pile 14-E' had an unconfined concrete compressive strength of 7.55 ksi (52.1 MPa). The spiral reinforcement had a design useable stress of 164 ksi (1131 MPa) and manufacturer reported nominal yield and ultimate strengths of 195 ksi (1345 MPa) and 206 ksi (1420 MPa), respectively. The spiral reinforcement was comprised of one 0.36 in. (9.14 mm) diameter wire at a pitch of 1.75 in. (44.5 mm). The longitudinal reinforcement consisted of four 0.5 in. (12.7 mm) diameter standard deformed steel reinforcing bars spaced evenly around the perimeter of the confined concrete core. The longitudinal reinforcement had a yield stress of 71 ksi (490 MPa).

The axial load versus axial shortening response of Specimen 14-E' is plotted in Figure 4.20. The specimen reached the first peak load of $P_1 = 1233$ kips (5.48 MN) at an overall axial shortening of $\Delta_1 = 0.175$ in. (4.45 mm). The corresponding axial strain was 0.0082. At this load, the concrete cover suffered extensive damage, losing nearly all of its effectiveness. After a small increase in load, the remainder of the cover failed.

Prior to cover failure, few, if any, cracks were observed in the cover concrete. At cover failure, visible damage to the cover concrete was apparent circumferentially around the test region. Longitudinal cracks also formed, extending from the circumferential splitting toward the top and bottom of the pile. The loss of cover concrete caused the load to drop to $P_{spall} = 834$ kips (3.71 MN).

The specimen exhibited considerably less axial stiffness after the loss of the concrete cover, evidenced by the shallower slope of the axial load-axial shortening plot in Figure 4.20 after P_{spall}. The specimen achieved its second peak at an axial load of $P_2 = 1117$ kips (4.97 MN) and at an axial shortening of 1.053 in. (26.75 mm). The axial strain was 0.0231.

After reaching P_2, the specimen continued to shorten while the load decreased until failure occurred at a load of $P_{failure} = 932$ kips (4.15 MN) and an axial shortening of 1.343 in. (34.11 mm).

Figure 4.21 shows the strain in the spiral reinforcement plotted versus the axial shortening. Each channel was plotted up to the point in the test at which the strain gage failed. The displacements at P_1 and P_2 are indicated in Figure 4.21 by Δ_1 and Δ_2, respectively.

Figure 4.22 shows the strain in the longitudinal reinforcement plotted versus the axial shortening. Just as in Figure 4.21, the displacements at P_1 and P_2 are indicated by Δ_1 and Δ_2, respectively. Figure 4.22 shows that, on average, the longitudinal reinforcement had achieved its yield value by the time Δ_1 was reached.

Figure 4.23 shows a schematic diagram of the failed pile. Only one spiral fracture was observed, which occurred near midheight of the pile around the north longitudinal reinforcing bar. No other fractures or necking were detected. Buckling was observed in all four longitudinal reinforcing bars, and no failure plane was seen in the concrete core.

Figure 4.24 shows two post-test photographs of the failed specimen. Figure 4.24(a) presents an overall view of the failed specimen. A relatively substantial amount of cover concrete surrounding the confined end regions remained attached throughout this test. It is not clear whether this was attributed solely to the tie wires. Figure 4.24(b) highlights the failure region on the north face, showing both the fracture of the spiral wire and buckling of the longitudinal reinforcement.

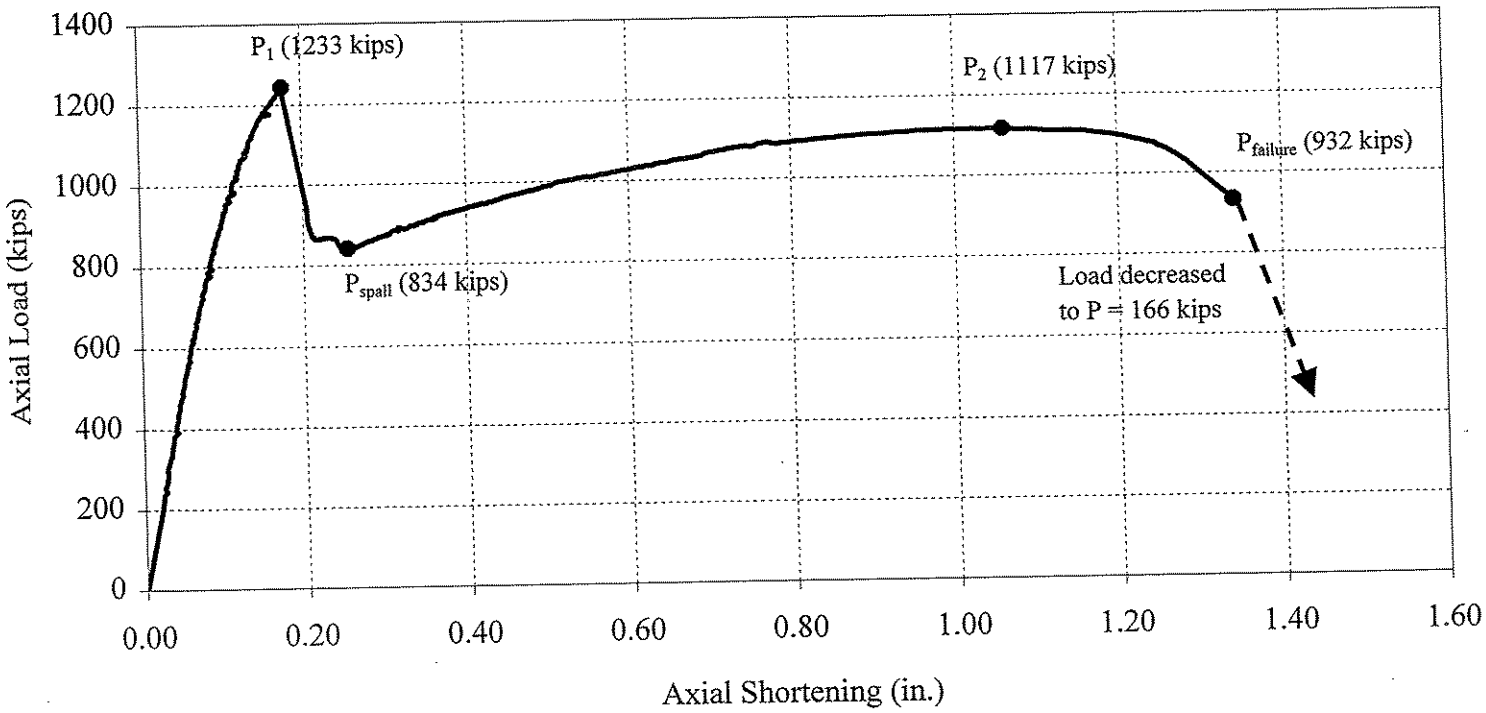

Figure 4.20 Plot of axial load versus axial shortening for Specimen 14-E'.

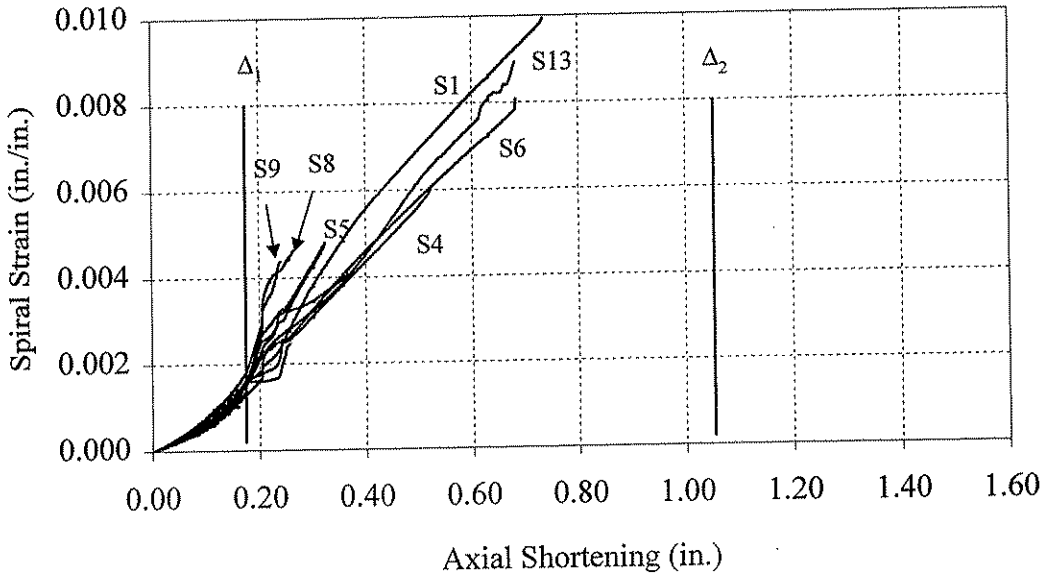

Figure 4.21 Plot of spiral strain versus axial shortening for Specimen 14-E'.

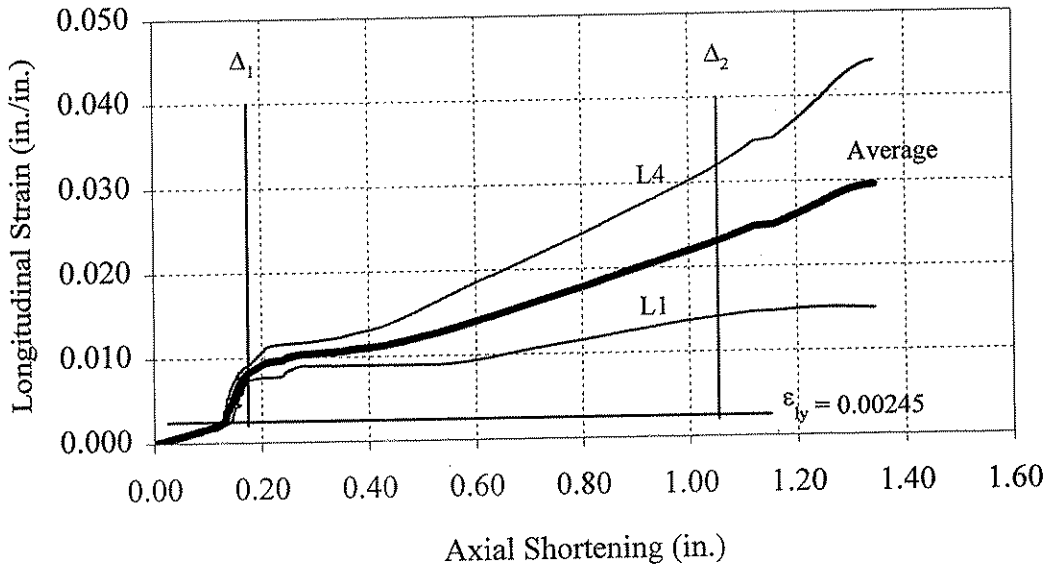

Figure 4.22 Plot of longitudinal strain versus axial shortening for Specimen 14-E'.

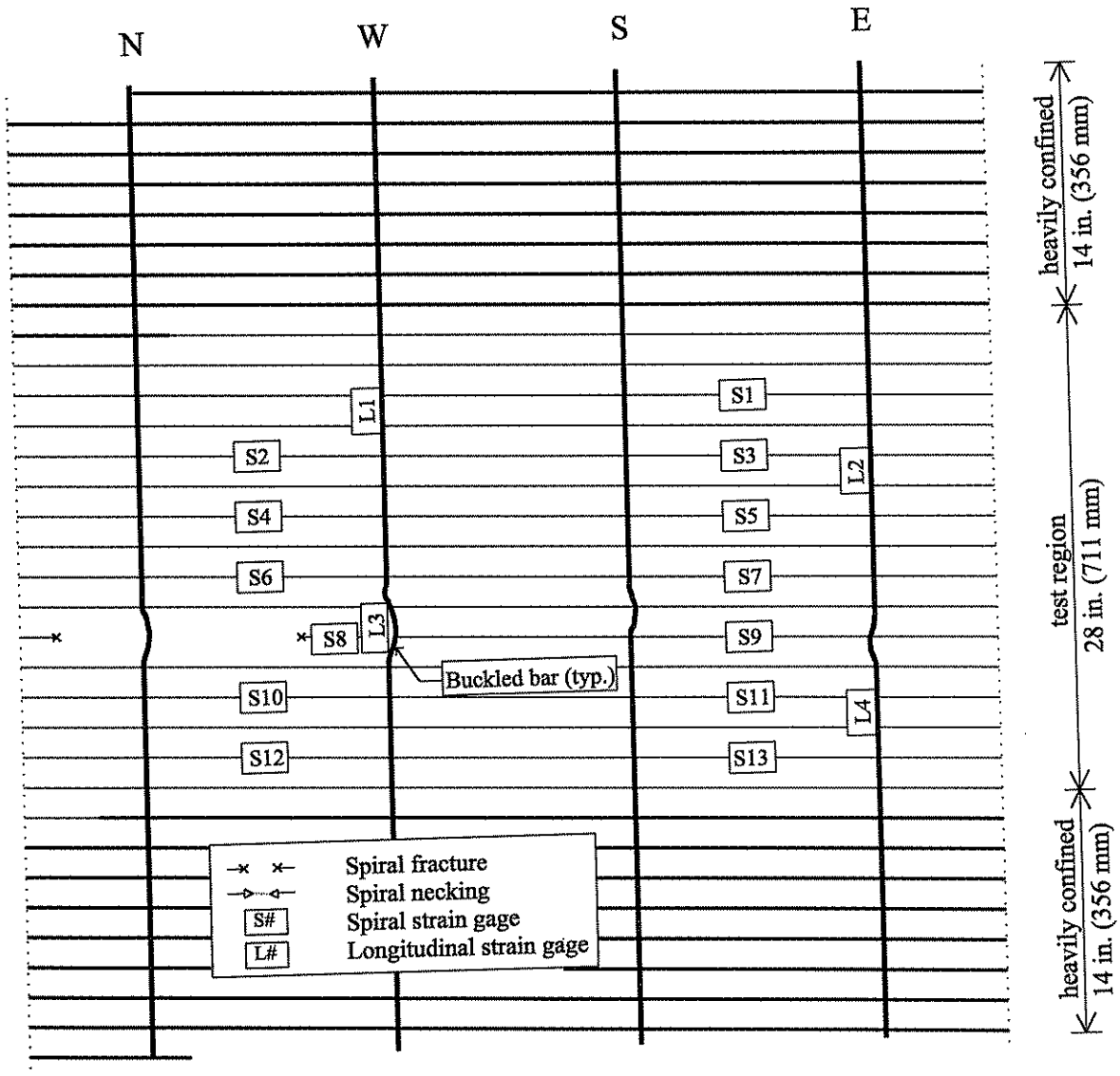

Figure 4.23 Schematic drawing of post-test appearance of Specimen 14-E'.

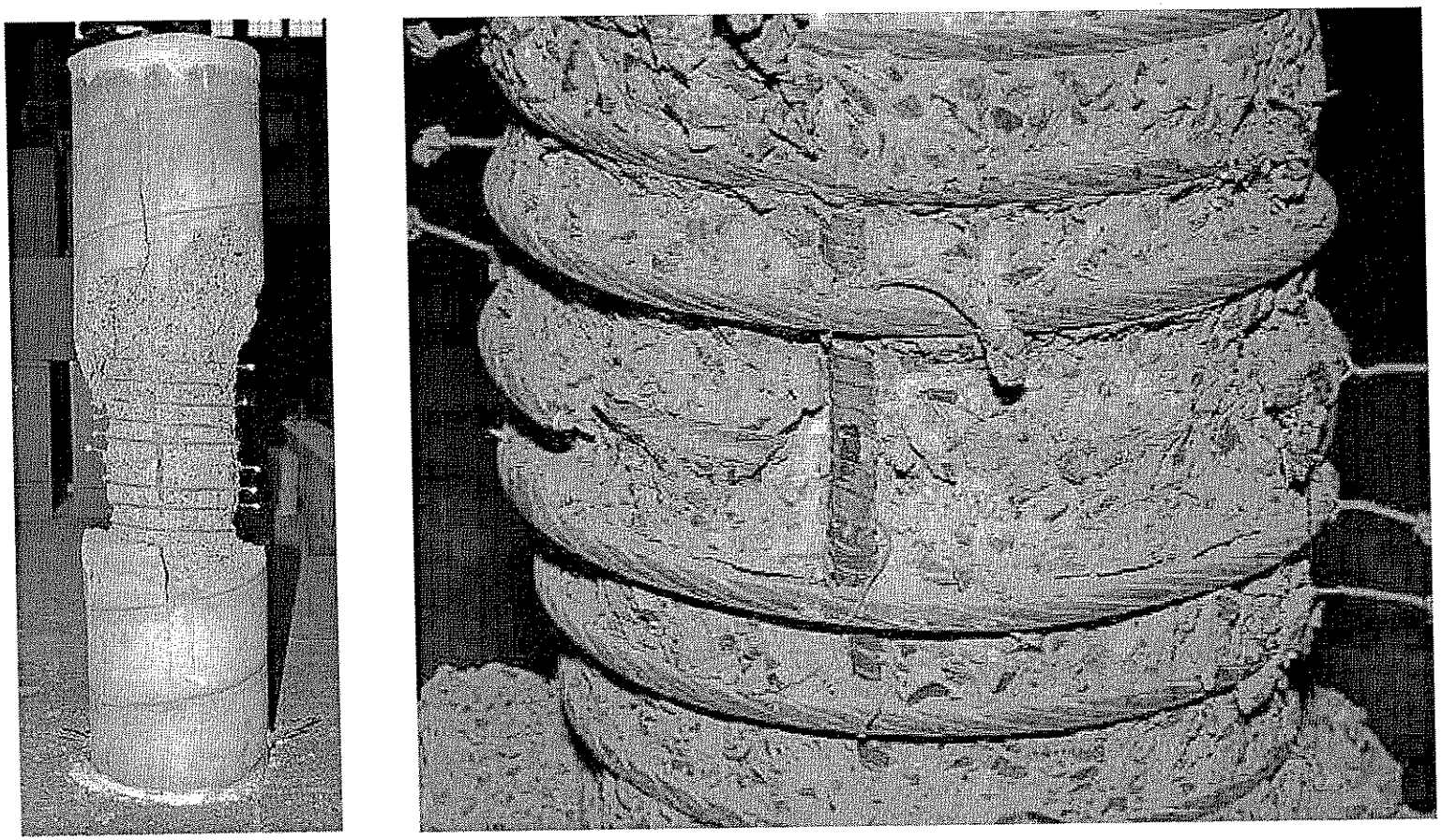

(a) (b)

Figure 4.24 Post-test photographs of Specimen 14-E': (a) overall view; (b) north face.

4.3.6 Pile 14-F'

Pile 14-F' had an unconfined concrete compressive strength of 7.55 ksi (52.1 MPa). The spiral reinforcement had a design useable stress of 161 ksi (1110 MPa) and manufacturer reported nominal yield and ultimate strengths of 185 ksi (1276 MPa) and 206 ksi (1420 MPa), respectively. The spiral reinforcement was comprised of one 0.43 in. (10.9 mm) diameter wire at a pitch of 2.43 in. (61.7 mm). The longitudinal reinforcement consisted of four 0.5 in. (12.7 mm) diameter standard deformed steel reinforcing bars spaced evenly around the perimeter of the confined concrete core. The longitudinal reinforcement had a yield stress of 71 ksi (490 MPa).

The axial load versus axial shortening response of Specimen 14-F' is plotted in Figure 4.25. The specimen reached the first peak load of $P_1 = 1201$ kips (5.34 MN) at an overall axial shortening of $\Delta_1 = 0.157$ in. (3.99 mm). The corresponding axial strain was 0.0021. At this load, the concrete cover suffered extensive damage, losing most of its effectiveness. After a brief increase in load, the remainder of the cover failed.

Prior to cover failure, few, if any, cracks were observed in the cover concrete. At cover failure, visible damage to the cover concrete was apparent circumferentially around the test region. Longitudinal cracks also formed, extending from the circumferential splitting toward the top and bottom of the pile. The loss of cover concrete caused the load to drop to $P_{spall} = 894$ kips (3.98 MN).

The specimen exhibited considerably less axial stiffness after the loss of the concrete cover. This behavior is evidenced by the shallower slope of the axial load-axial shortening plot in Figure 4.25 after P_{spall}. The specimen achieved its second peak at an axial load of $P_2 = 1131$ kips (5.03 MN) and at an axial shortening of 0.951 in. (24.16 mm). The axial strain was 0.0206.

After reaching the second peak in the load-shortening response, the specimen continued to shorten while the load decreased until failure occurred at a load of $P_{failure} = 613$ kips (2.73 MN) and an axial shortening of 1.431 in. (36.35 mm).

Figure 4.26 shows the strain in the spiral reinforcement plotted versus the axial shortening. Each channel was plotted up to the point in the test at which the strain gage failed. The displacements at P_1 and P_2 are indicated in Figure 4.26 by Δ_1 and Δ_2, respectively.

Figure 4.27 shows the strain in the longitudinal reinforcement plotted versus the axial shortening. Just as in Figure 4.26, the displacements at P_1 and P_2 are indicated by Δ_1 and Δ_2, respectively. Figure 4.27 shows that, on average, the stress in the longitudinal reinforcement was slightly below its yield value when Δ_1 was reached.

Figure 4.28 presents a schematic diagram of the failed pile. One spiral fracture was observed, located in the lower east part of the test region. Necking of the spiral reinforcement was detected in two locations on opposite faces of the pile. Buckling was observed in each longitudinal reinforcing bar. Furthermore, extensive damage was seen in the concrete core. A concrete failure

plane of approximately 46° inclination from the horizontal was observed in the southwest face of the pile, but the concrete failure plane did not clearly extend throughout the entire pile.

Figure 4.29 shows several post-test photographs of the failed specimen. Figure 4.29(a) presents an overall view of the failed pile. Figure 4.29(b) shows the failure region on the east face of the specimen, and Figure 4.29(c) illustrates the failure region on the northeast face. In Figure 4.29(b), arrows are used to highlight the suggested formation of a partially developed inclined failure plane in the concrete core. Extensive buckling of the north and east longitudinal bars, as well as severe damage to the concrete core, can be seen in the figures.

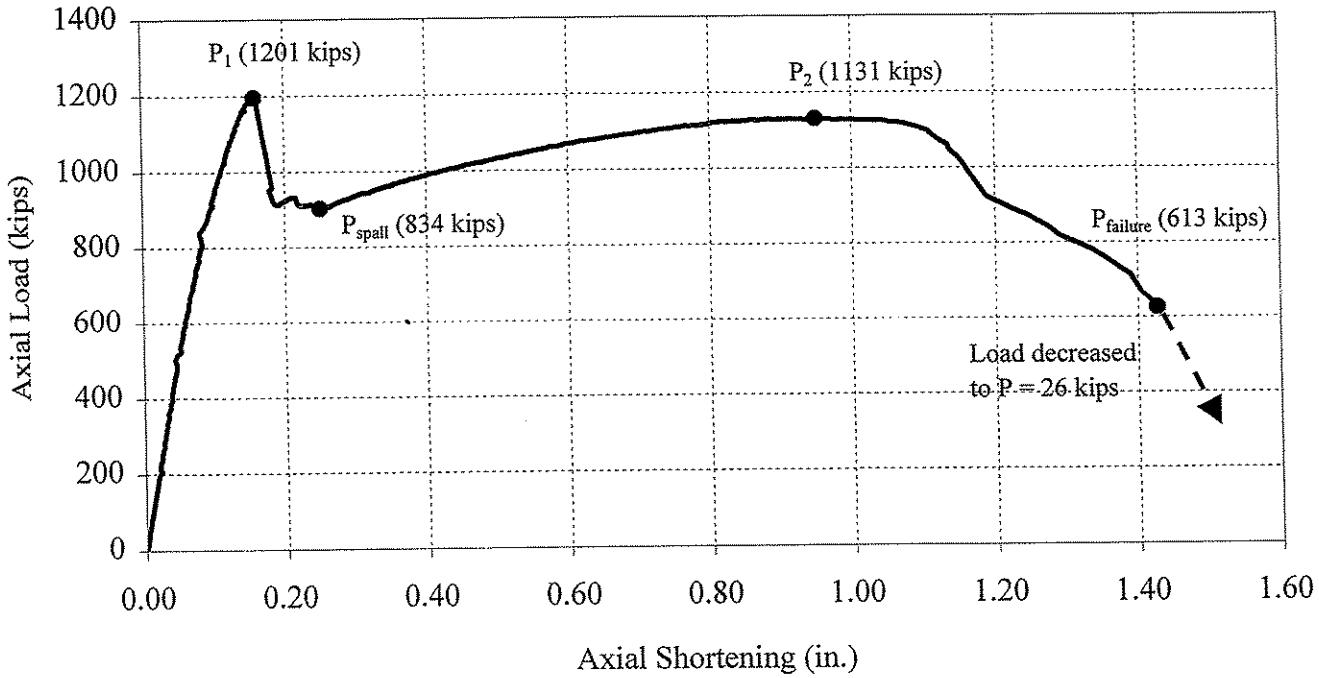

Figure 4.25 Plot of axial load versus axial shortening for Specimen 14-F'.

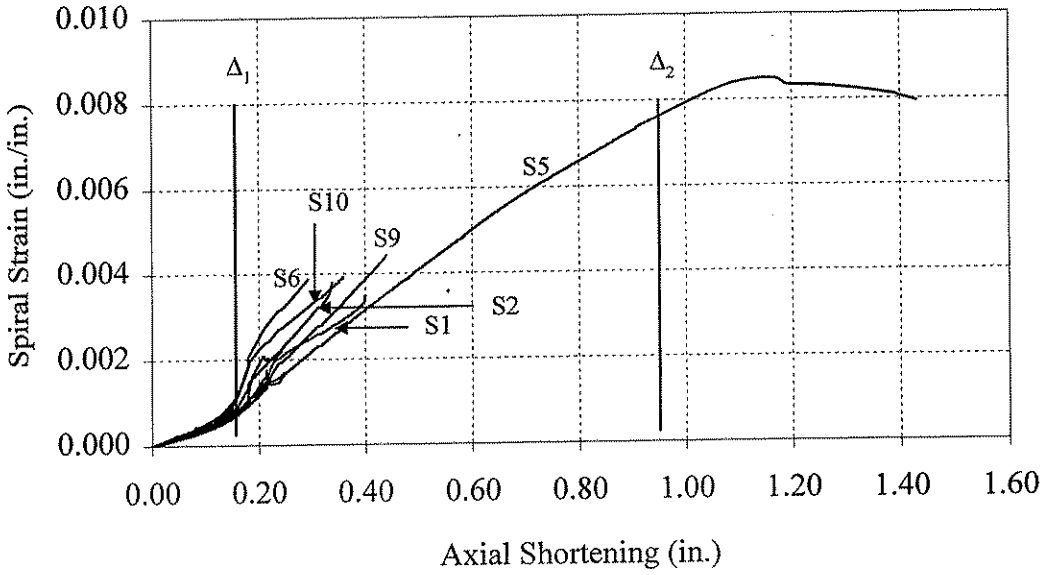

Figure 4.26 Plot of spiral strain versus axial shortening for Specimen 14-F'.

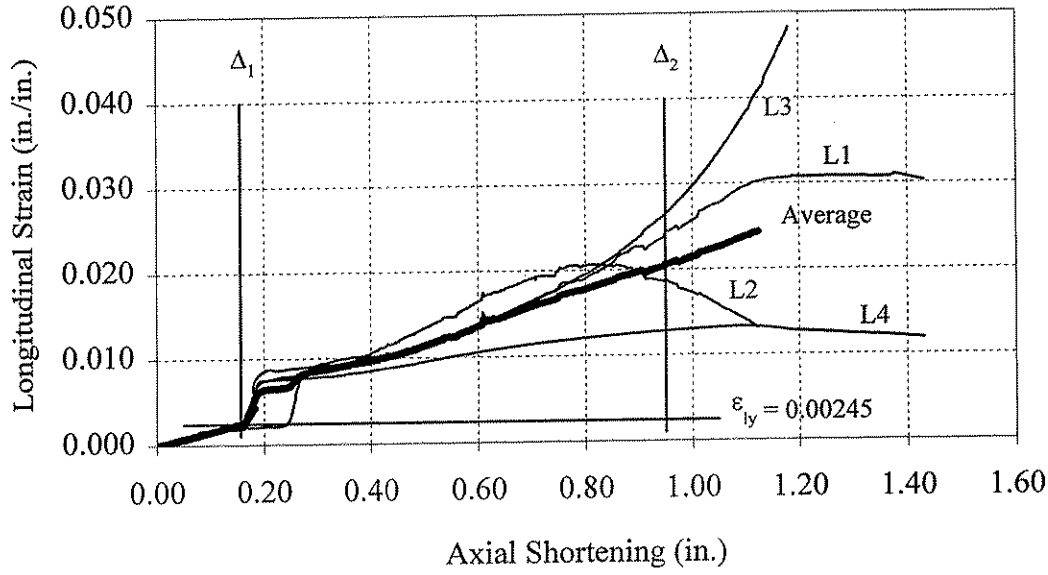

Figure 4.27 Plot of longitudinal strain versus axial shortening for Specimen 14-F'.

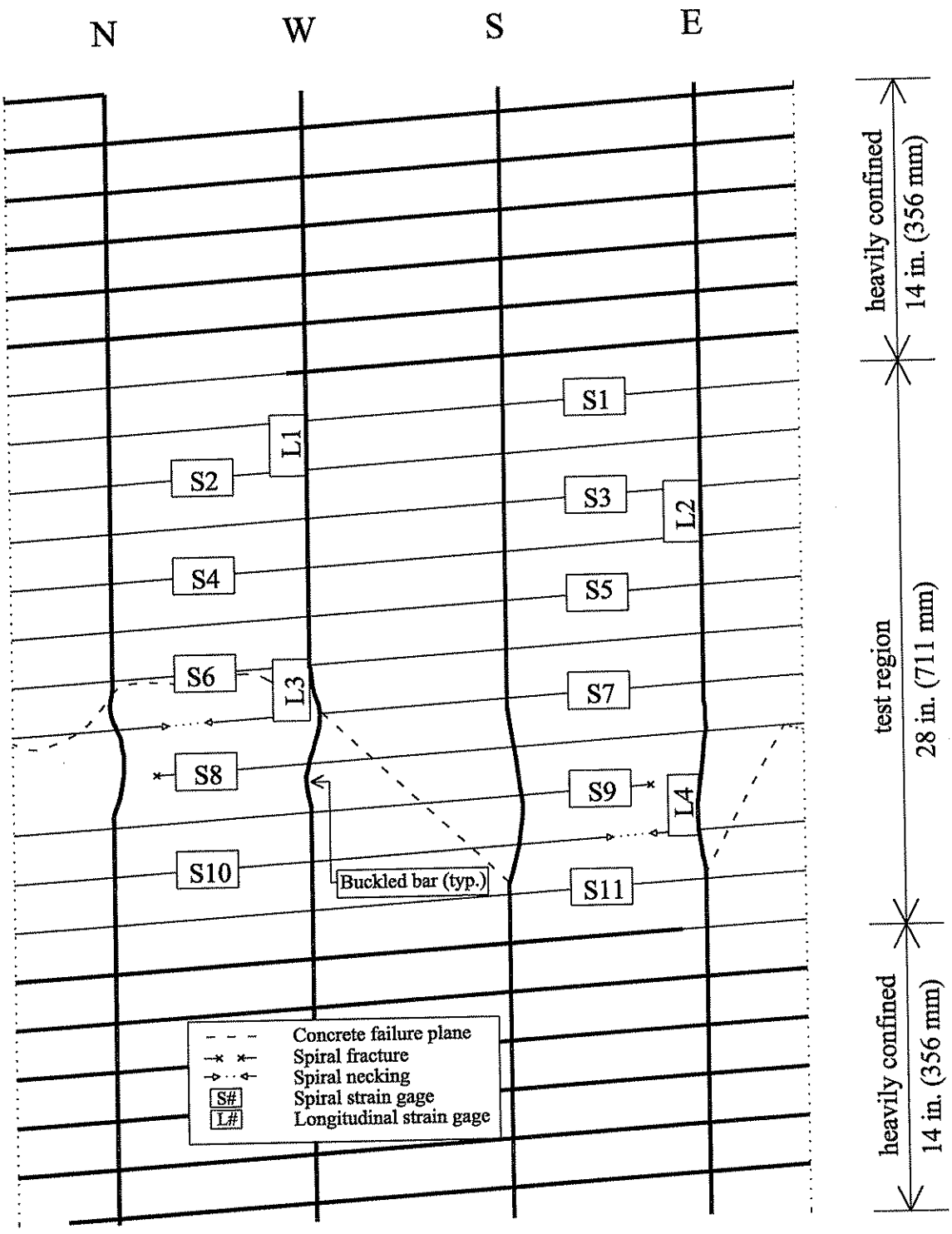

Figure 4.28 Schematic drawing of post-test appearance of Specimen 14-F'.

(a) (b) (c)

Figure 4.29 Post-test photographs of Specimen 14-F': (a) overall view; (b) east face; (c) northeast face.

CHAPTER 5
ANALYSIS OF SPIRAL STRESS-STRAIN RELATIONSHIPS

5.1 INTRODUCTION

The results of tension tests performed on the spiral wires were presented in Chapter 3. As noted in Chapter 3, three of the wires were tested in an unspiraled state (D', E', F'), and four of the wires were tested in a spiraled-straightened state (A', B', C', D').

The process of spiraling a wire introduces residual stresses into the cross-section. These residual stresses change the tension stress-strain curve of the material from its unspiraled state. Straightening a wire from its spiraled state further alters the residual stresses on the cross-section, and thus further alters the stress-strain curve of the wire. The effect of the spiraling and straightening processes on the stress-strain behavior of a wire was studied by Graybeal et al. (1998) and reviewed in Chapter 2.

This chapter examines the effect of the spiraling and straightening processes on the stress-strain behavior of wires E' and F'. Fiber model analyses, using the DRAIN-2DX computer program (Prakash and Powell, 1993), were performed for this purpose.

Much of the background information related to this chapter has previously been presented in Section 2.3.4. Section 5.2 presents the fiber modeling and analysis procedures employed to obtain the desired results from DRAIN-2DX. Section 5.3 discusses the results of the fiber model analyses.

5.2 FIBER MODELING

The analyses performed utilize the fiber element, which is a nonlinear inelastic element in DRAIN-2DX. Using this element, the cross-section of a wire is discretized into a number of fibers. Each individual fiber is characterized by a distance from the reference axis along the length of the member, an area, and a uniaxial stress-strain relationship. The monotonic stress-strain relationship for each fiber can be defined by up to five points, and the program assumes a linear interpolation between each point, resulting in a five-part linear approximating stress-strain curve. The cyclic stress-strain relationship of the fiber is computed by DRAIN-2DX based upon the monotonic stress-strain relationship and hysteretic rules that are predefined for the material. The hysteretic rules used in this research are the same as employed by Graybeal et al. and are shown in Figure 5.1. As shown in the figure, the strains in the uniaxial stress-strain curve are doubled in order to determine the shape of the cyclic curve.

Figures 5.2 and 5.3 show the experimentally determined stress-strain curves obtained from tension tests on unspiraled lengths of spiral steels E' and F', respectively. Superimposed on the experimentally determined stress-strain curves are the five-part approximating curves.

Plane section behavior of the cross-section is assumed in the response of the fiber element. By utilizing a plane section analysis and an assumed curvature, the strain in each fiber is computed. The stress-strain curve is then used to compute the stress in each fiber. These stresses are

integrated over the cross-section and equilibrium is checked with the current applied forces. Successive values of curvature are assumed until equilibrium is established.

In order to model the wire using DRAIN-2DX, the length and cross-section of the wire must be defined. For this research, the spiraling and straightening processes were modeled by applying pure bending moment to a length of wire. Thus the length of the wire is arbitrary, and the model was composed of a segment of wire whose length was equal to ten percent of the circumference of the spiraled configuration of the wire, as shown in Figure 5.4. A circular cross-section was used to model the wire cross-section. Figure 5.4 shows the circular cross-section divided into 14 fibers, each of equal height. For this research, 140 equal height fibers were utilized to model the cross-section of the element. Graybeal et al. reported that this provided a satisfactory balance between accuracy and computational time. Each fiber was assigned the same stress-strain curve.

As noted above, the spiraling process was modeled by applying a constant bending moment over the length of the wire. The modeling of the spiraling process was done by trial and error. First, a constant moment was applied to the ends of a straight wire, which resulted in a radius of curvature of the deformed wire that was smaller than the desired radius of curvature of the spiral. Next, the spiraling moment was effectively removed by applying an equal and opposite moment to the ends of the deformed wire. Through trial and error, the value of moment that created the desired spiraled curvature was obtained.

DRAIN-2DX was also used to model the straightening process. The procedure is basically the same as that of the spiraling process. In this case, a constant bending moment of opposite sense to the spiraling moment was applied to the ends of the spiraled wire. The magnitude of the moment, which was slightly less than that of the spiraling moment, was such that it caused the wire to bend through the straight position into the opposite curvature. Next, the straightening moment was effectively removed through the application of an equal and opposite moment. The correct straightening moment caused all strains in the cross-section to return to zero.

DRAIN-2DX was also used to model the application of axial tension to a wire in its unspiraled, spiraled, and spiraled-straightened states. This load application resulted in the generation of a monotonic stress-strain curve for each wire in each state.

Application of the spiraling moment, unspiraling moment, and the axial load were displacement-controlled. The process of releasing the moments was load-controlled. The spiraling and unspiraling moments were applied by incremental changes in rotation of the ends of the wire. The desired curvature was achieved by incrementally releasing the moments until a net value of zero was achieved. In the application of axial tension, the wire was strained incrementally to an approximate value of 0.0033. This value was chosen because it easily exceeded the maximum strain value to which the spiral reinforcement would be subjected during the pile tests, and it allowed nearly total convergence of the three different stress-strain curves.

5.3 FIBER MODEL ANALYSIS RESULTS

Figures 5.5 and 5.6 show the fiber model analysis results for wires E' and F', respectively. Shown in each figure are the fiber model predicted tension stress-strain curves for the unspiraled, spiraled, and spiraled-straightened states. Both figures show that when a high strength spiraled wire is placed in uniaxial tension, considerable rounding or softening of the stress-strain curve is produced as compared to the unspiraled case. Straightening a spiraled wire before placing it in uniaxial tension restores some resistance to the wire at a given value of strain. However, the original stress-strain curve produced from uniaxial tension on an unspiraled wire was not achieved. Eventually, as strain increased, all three stress-strain curves converge to the yield stress value.

Quantitative comparisons were made to evaluate the effects of the spiraling and straightening processes. Table 5.1 presents numerical results obtained from the fiber model analyses at two key values of strain. In the table, 'US' represents the unspiraled state, 'S' represents the spiraled state, and 'SS' represents the spiraled-straightened state. At the design value of useable strain, 0.0062, the spiraling process caused a 15 percent reduction in stress from the unspiraled state ($R_{S/US} = 0.85$) for both wires. When the straightening process was applied to the spiraled wire, the resulting stress was found to be 90 percent of the stress value returned from the analysis on an unspiraled wire at that strain value. This shows that 5 percent of the strength lost due to spiraling was recovered in the straightening process at that particular value of axial strain.

Table 5.1 also presents the stresses corresponding to the second peaks in the load-deflection plots of the respective pile specimens. For spiral wire E', the experimentally observed value of strain at P_2 was 0.0122. The fiber model analysis showed that the spiraling process resulted in a 4 percent decrease in the stress level that would be achieved in the unspiraled wire at that value of strain. By straightening the wire, the analysis showed a 2 percent increase in stress from that in the spiraled wire. For spiral wire F', the experimentally determined value of ϵ_{sp2} was 0.0086. The fiber model analysis showed that the spiraling process resulted in a 12 percent decrease in the stress level that would be achieved in the unspiraled wire at that value of strain. The analysis showed that by straightening the wire, the deviation between the stresses in the wire in its unspiraled and spiraled-straightened states at 0.0086 was 8 percent.

The results of the fiber model analyses show that an error of about 15 percent was incurred in the design of Specimen 14-E' and Specimen 14-F' by basing the design of the piles on the stress-strain curves of unspiraled wire specimens as opposed to spiraled wires. Had the designs of Specimens 14-E' and 14-F' been based on theoretical spiraled stress-strain curves instead of experimental unspiraled stress-strain curves, the useable stress values would have been reduced from 164 ksi to 148 ksi (1131 MPa to1020 MPa) for Specimen 14-E', and from 161 ksi to 145 ksi (1110 MPa to1000 MPa) for Specimen 14-F'. Furthermore, should the trend hold true for wires A' through D', the design useable stresses were overestimated by approximately 10 percent by basing the design of the piles on the stress-strain curves of spiraled-straightened wire specimens.

From the above discussions and the values presented in Table 5.1, the fiber model analyses indicate that the design useable stress values should be modified to account for the changes in the tension stress-strain curve that are caused by spiraling.

Strain	Spiral Steel	Strain Value	Stress in Spiral (ksi)			$R_{S/US}$	$R_{SS/US}$
			Unspiraled State	Spiraled State	Spiraled-Straightened State		
Design Useable Strain, $\varepsilon_{sp2,dsgn}$	E'	0.0062	164	139	148	0.85	0.90
	F'	0.0062	161	137	145	0.85	0.90
Experimentally Determined Useable Strain, $\varepsilon_{sp2,exp}$	E'	0.0122	194	177	191	0.96	0.98
	F'	0.0086	191	168	176	0.88	0.92

1 ksi = 6.895 MPa

Table 5.1 Comparison of stresses at key values of strain as obtained from fiber model analyses of spiral wires E' and F' in the unspiraled, spiraled, and spiraled-straightened states.

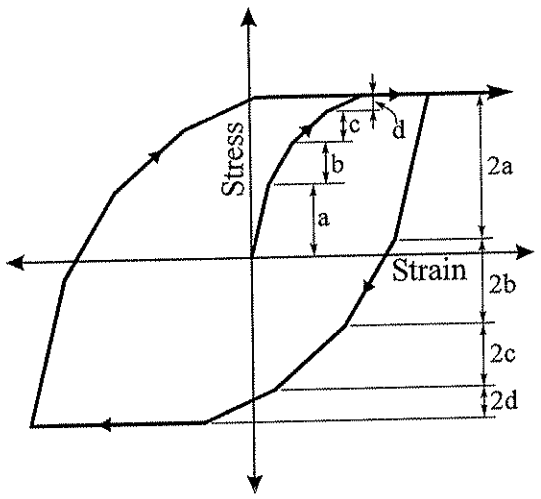

Figure 5.1 General cyclic stress-strain relationship of a multi-linear stress-strain curve used in the fiber model (Graybeal et al. (1998)).

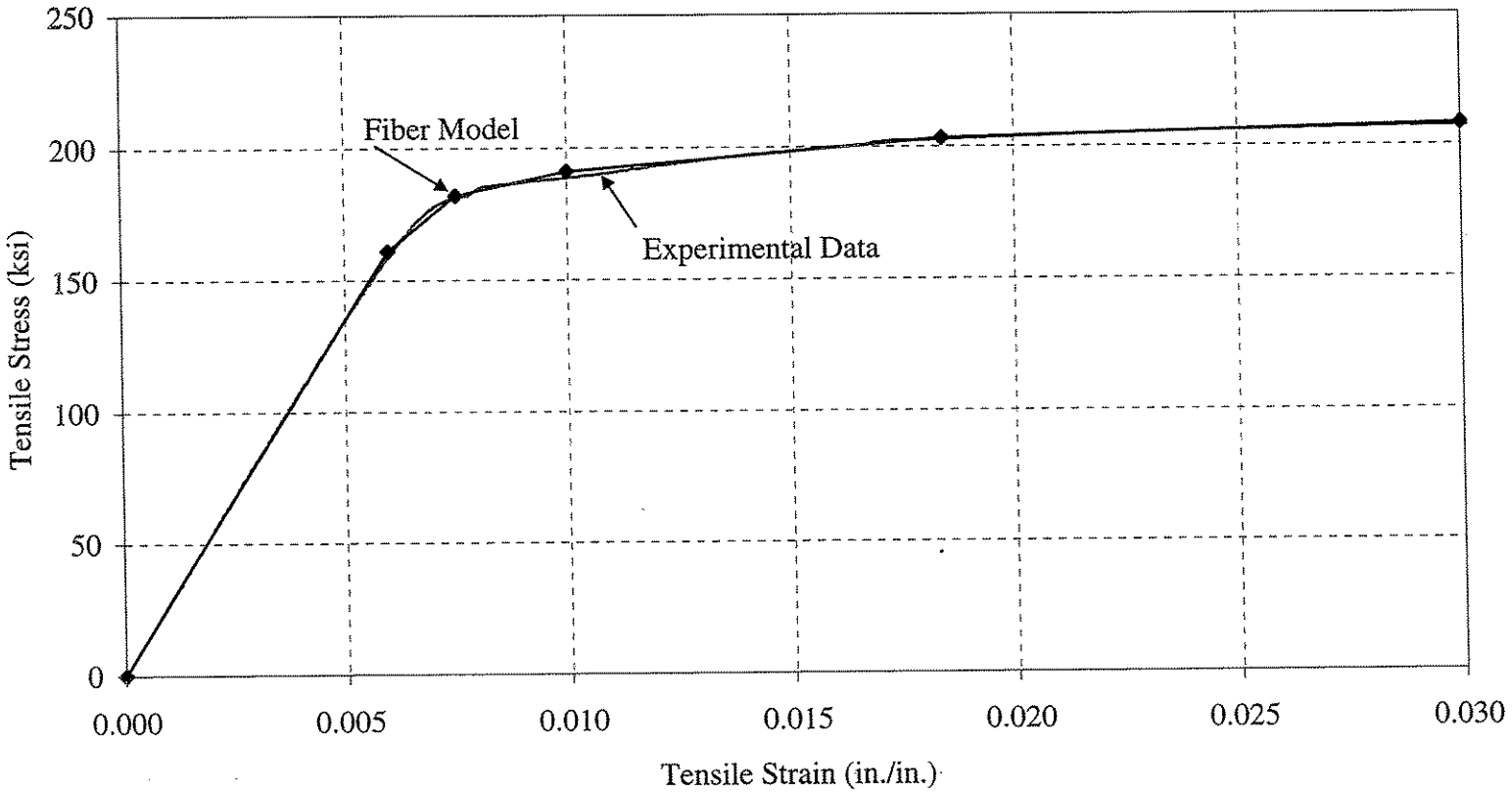

Figure 5.2 Approximation of spiral steel E' unspiraled stress-strain curve used in fiber model analyses.

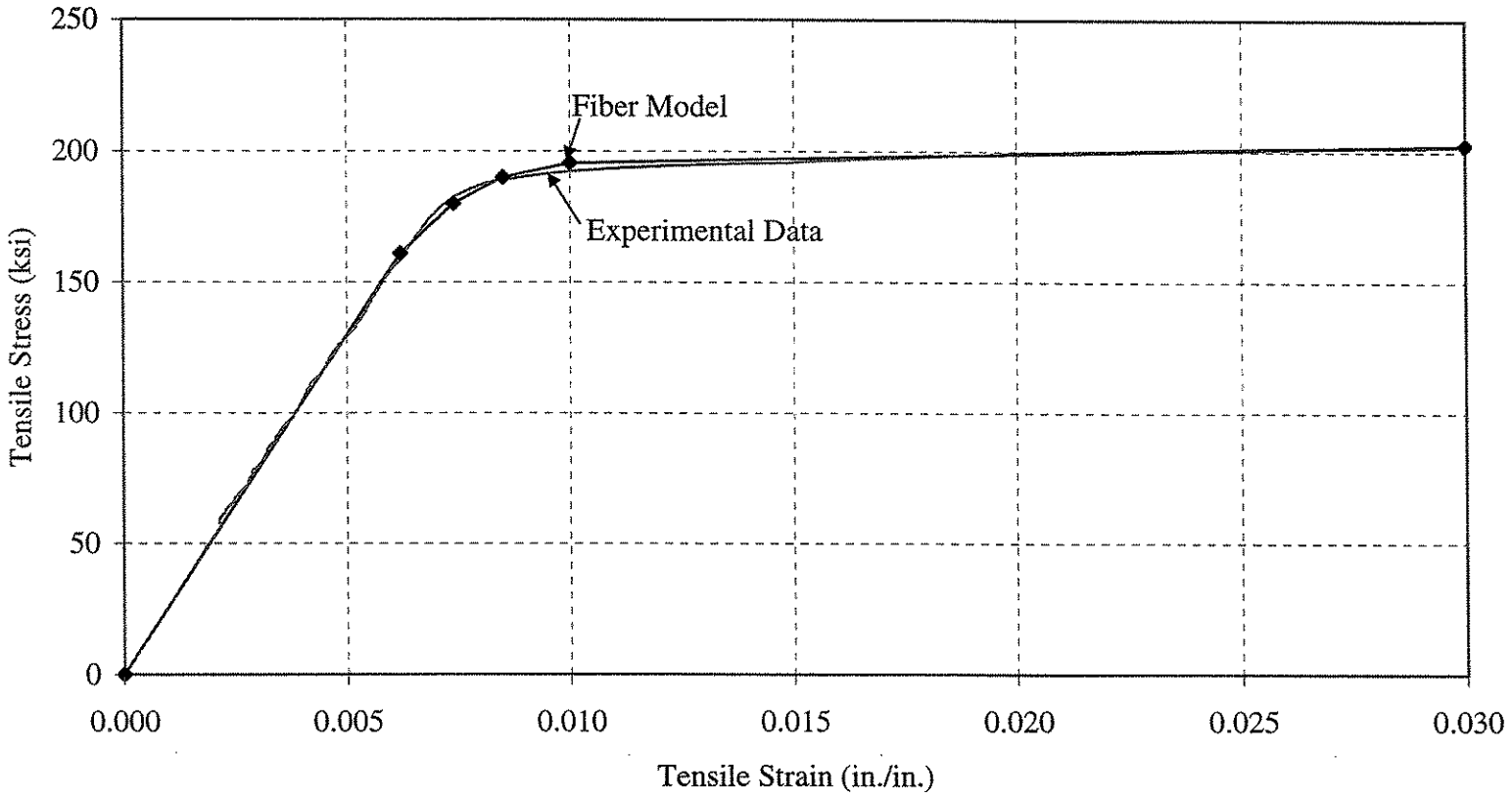

Figure 5.3 Approximation of spiral steel F' unspiraled stress-strain curve used in fiber model analyses.

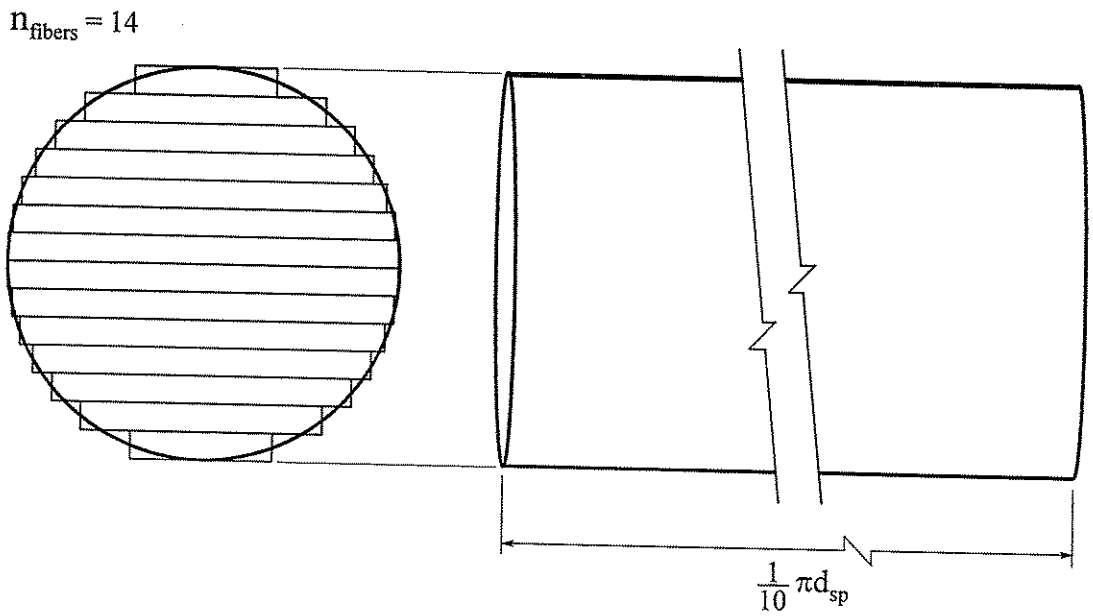

Figure 5.4 Example of fiber model of wire cross-section and length (Graybeal et al. (1998)) (Actual model used $n_{fibers} = 140$).

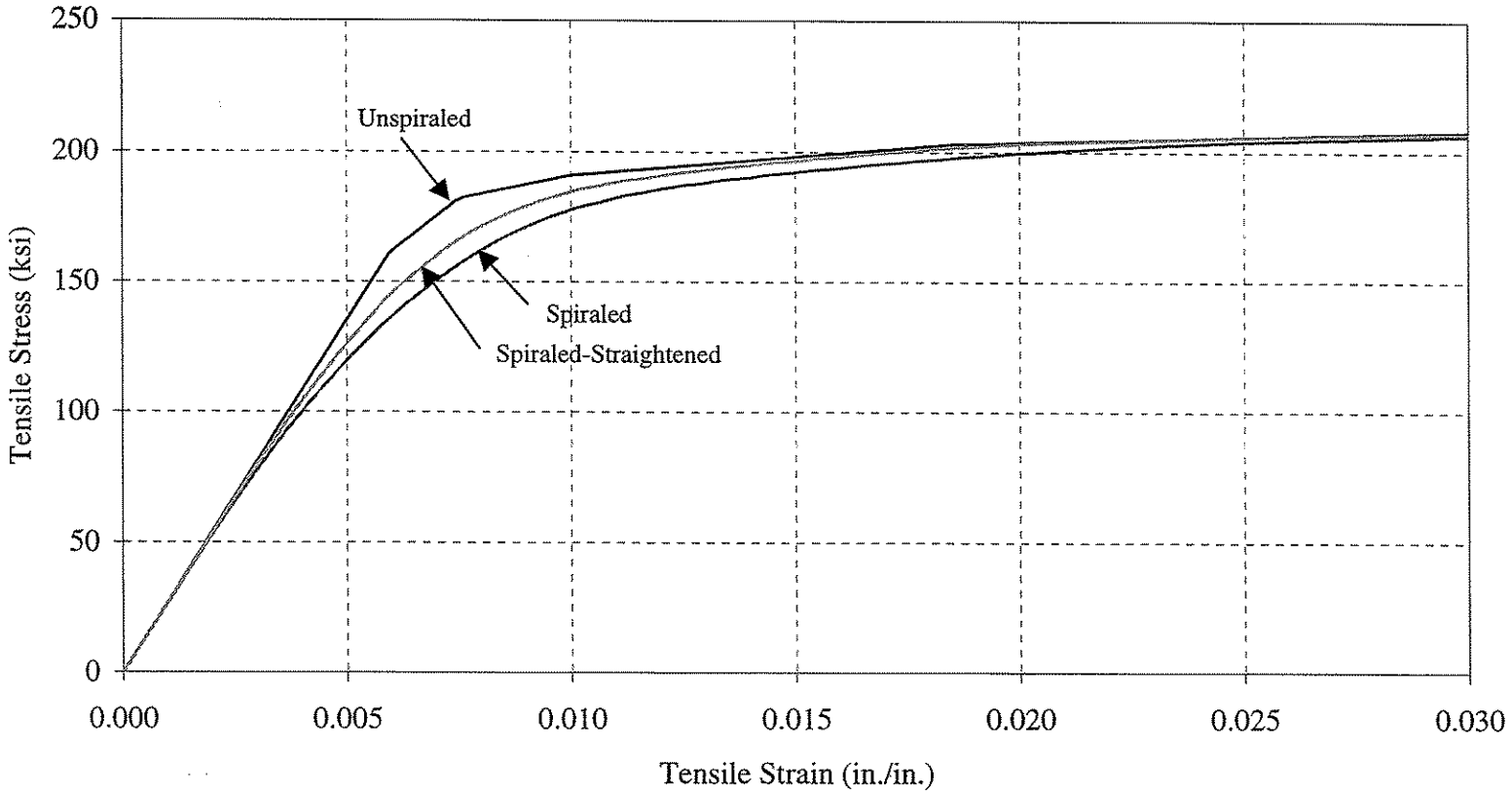

Figure 5.5 Fiber model analysis results showing effects of spiraling and straightening processes on spiral steel E'.

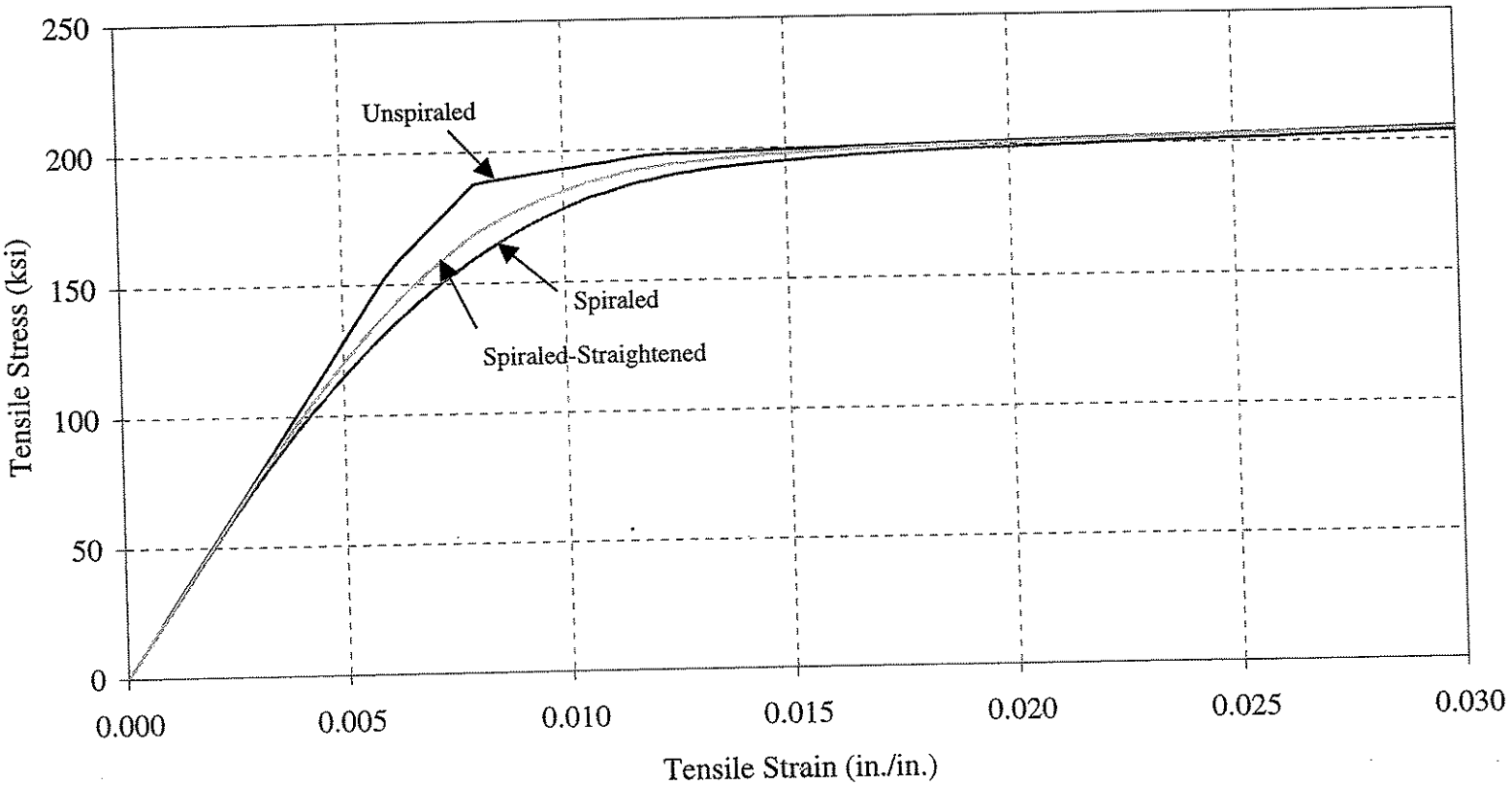

Figure 5.6 Fiber model analysis results showing effects of spiraling and straightening processes on spiral steel F'.

CHAPTER 6
ANALYSIS AND DISCUSSION OF RESULTS

6.1 INTRODUCTION

This chapter presents a detailed analysis and discussion of the results obtained from the experimental program. The topics covered in this chapter include spiral behavior, cover behavior, pile failure mechanisms, and concrete dilation behavior. Additionally, comparisons between experimental and predicted results are made.

Section 6.2 provides a comparison between the experimentally recorded longitudinal strain at Δ_2, the design value of strain, and the strain predicted by two different empirical equations. Section 6.3 discusses the behavior of the spiral reinforcement in the response of the piles. The measured strains and stresses at key stages in the response of each pile are compared to predicted values of strains and stresses. Section 6.4 provides a brief description of the cover behavior as observed during the pile tests, and Section 6.5 discusses the observed pile failure mechanisms. Section 6.6 presents a comparison between the experimental increase in confined concrete strength and the increase in confined concrete strength predicted by the results in the literature. Section 6.7 discusses the dilation behavior of the piles. The experimentally determined value of transverse strain at Δ_2, $\epsilon_{ct2,exp}$, is compared to the values of ϵ_{ct2} predicted by the secant and tangent dilation ratios, $\epsilon_{ct2,sec}$ and $\epsilon_{ct2,tan}$, respectively. The tangent dilation ratio relationship proposed by Graybeal et al. is briefly reviewed and compared to the experimental results. Section 6.8 comments on the applicability of the design procedure proposed by Graybeal et al. Finally, Section 6.9 presents some limitations on the proposed design procedure. Included in this section are brief discussions of several factors that may have hindered the concrete core strength enhancement for Specimens 14-E' and 14-F'.

As stated earlier, the results for Specimen 14-B' are valid only up to cover spalling. Therefore, all comparisons and discussions regarding pile behavior after Δ_{spall} do not include Specimen 14-B'.

6.2 COMPARISON OF EXPERIMENTAL AND PREDICTED LONGITUDINAL STRAINS

The longitudinal strain in a pile at Δ_2 is a key parameter in the spiral design procedure proposed by Graybeal et al. A comparison is made here between the experimental, design, and predicted longitudinal strains of the piles treated in this study.

From the strain gages attached to the longitudinal steel reinforcement, experimental values were obtained for the longitudinal strain in each pile specimen at Δ_2. The average of the readings for each specimen at Δ_2 was computed, and this value is taken as $\epsilon_{c2,exp}$. The design value of strain was computed in Step 3 of the design procedure proposed by Graybeal et al. and is given as $\epsilon_{c2,dsgn}$.

Table 6.1 shows the experimentally obtained values and design values of ϵ_{c2}. For the pile geometry and material properties included in this study, the value of $\epsilon_{c2,dsgn}$ was calculated from the proposed design procedure as 0.0158. Additionally, the ratio of the experimental and design

values, $R(\epsilon_{c2})_{exp/dsgn}$, is shown. These ratios are plotted in Figure 6.1. Table 6.1 and Figure 6.1 show that the experimental values exceed the design values in every case except Specimen 14-A', where the value of $R(\epsilon_{c2})_{exp/dsgn}$ is 0.97. This indicates that the proposed design procedure is conservative in the prediction of longitudinal strains at Δ_2.

Equation 2.9, which was proposed by Richart et al. (1928, 1929, 1934) to predict the axial strain at peak confined concrete compressive stress, is repeated here.

$$\varepsilon_{c2,rich} = \varepsilon_{co}\left(5\frac{f_{c2}}{f_{co}} - 4\right) \tag{2.9}$$

In order to examine the applicability of the equation, the experimentally determined values of f_{c2} and f_{co} were substituted into it. The value of f_{c2} was determined from Equation 2.7, the value of f_{co} was taken as 7.55 ksi (52.1 MPa), and the value of ϵ_{co} was taken as 0.0027.

Table 6.1 shows both the experimentally obtained values and Richart et al. predicted values of ϵ_{c2}. Table 6.1 also shows the ratio of these two values, $R(\epsilon_{c2})_{exp/rich}$. This ratio is plotted in Figure 6.2 for each pile specimen. For every specimen except Specimen 14-A', where the predicted value of longitudinal strain exceeded the experimental value, the experimental value is considerably higher than the predicted value. Generally, a higher confining pressure at Δ_2, $f_{2\text{-}2}$, corresponds to a more conservative prediction of the longitudinal strain.

Cusson and Paultre (1995) also developed an equation to predict ϵ_{c2}. This relationship is given as Equation 6.1.

$$\varepsilon_{c2,cus} = \varepsilon_{co} + 0.21\left(\frac{f_{2-2}}{f_{co}}\right)^{1.7} \tag{6.1}$$

The applicability of this equation was examined by substituting into it the experimentally determined values for $f_{2\text{-}2}$ and f_{co}, as well as a value of ϵ_{co} determined by Graybeal et al. The strain computed from this equation is referred to as $\epsilon_{c2,cus}$. ϵ_{co} and f_{co} were taken as 0.0027 and 7.55 ksi (52.1 MPa), respectively. For each pile, the value of $f_{2\text{-}2}$ was calculated from Equation 2.12 using the value of f_{sp2} approximated in Table 6.3. The method employed to obtain the value of f_{sp2} will be discussed in Section 6.3.

Table 6.1 shows the experimentally obtained values and Cusson et al. values of ϵ_{c2}. Additionally, the ratio of these two values, $R(\epsilon_{c2})_{exp/cus}$, is shown. These ratios are plotted in Figure 6.3. Figure 6.3 shows that Equation 2.9 provides a reasonable or conservative estimate of ϵ_{c2}. In four of the five cases (with the exception being Specimen 14-C'), the experimentally observed longitudinal strains are less than the predicted values. While four of the five predictions overestimate the experimental values, the general trend in the data shows that the Cusson et al. prediction becomes more conservative as the value of f_{c2} increases. This trend is opposite to that reported by Graybeal et al. in their work.

Based on these results, it is concluded that the Richart et al. prediction of longitudinal strain (Equation 2.9), in general, provides conservative estimates of ϵ_{c2}. This is particularly true for higher strength spiral reinforcement. In comparison, the Cusson et al. prediction of axial strain (Equation 6.1) generally overestimates the experimental value of ϵ_{c2}. Thus, it is concluded that Equation 2.9 is more appropriate as part of the proposed design procedure, since this equation will lead to a conservative design of the spiral.

6.3 SPIRAL BEHAVIOR

Included in each individual test summary in Chapter 4 was a plot of spiral strain versus axial shortening for the respective pile specimens. Those results, replotted in terms of stress in the spiral reinforcement, are shown in Figures 6.4 through 6.8. The stresses were obtained from the strain measurements and through the use of the best-fit stress-strain curves shown in Figure 3.8. As previously mentioned, these curves are numerical approximations of the experimental data from tension tests on segments of spiral reinforcement. Best-fit curves were based on stress-strain curves from spiraled-straightened wires for spiral wires A' through D' and from unspiraled wires for spiral wires E' and F'.

As noted in Chapter 4, many of the strain gages failed prior to the completion of the tests. Therefore, some of the data was extrapolated based on the trends observed both in the existing data and the trends observed in the work of Graybeal et al. (1998). From these trends, an approximate range is indicated for several of the key values of spiral stress. When it was necessary to extrapolate data, the extrapolations were made based on the spiral strain versus axial shortening plots as opposed to the spiral stress versus axial shortening plots. This was done because the trends were more linear when plotted as strains rather than stresses, and thus the approximations were thought to be more accurate. This approach differs from that taken in Graybeal et al., where approximations were taken from the spiral stress versus axial shortening curves.

Table 6.2 presents approximate values of spiral strain at three values of axial shortening: Δ_1, Δ_{spall}, and Δ_2. Table 6.3 presents the maximum and minimum stresses in the spiral reinforcement at Δ_1, Δ_{spall}, and Δ_2. Also included in the table are single value approximations for the spiral stresses at these three key stages in the pile response. These approximate values are based upon the strain values given in Table 6.2. Two of these single value approximations of the spiral stress, f_{sp1} and f_{sp2}, are also noted on Figures 6.4 through 6.8 for each individual pile specimen. Finally, Table 6.4 presents the single value approximations of f_{sp} at the same three key stages, along with the volumetric ratio of spiral steel present in each specimen. Also provided for each stage in the specimen responses are the values of confining pressure f_2, calculated from Equation 2.4.

The stress in the spiral reinforcement, and therefore the confining pressure applied to the concrete core, increased approximately two-fold between Δ_1 and Δ_{spall}. This is attributed to the elimination of the load path through the concrete cover. As the cover concrete failed, the core concrete picked up additional load, causing increased dilation of the core. At this stage in the pile behavior, the spiral reinforcement is providing sufficient confining pressure to maintain the integrity of the core concrete.

The spiral values reported for Δ_2 are based on fewer strain gage readings than were available for the values at Δ_1. At Δ_2, few strain gages remained functional, which made it necessary to approximate several values. As shown in Table 6.3, for a given pile the range of spiral stress at Δ_2 is as large as 40 ksi (276 MPa). However, based on the trends shown in the spiral strain versus axial shortening plots in Chapter 4, an approximation of the spiral stress, f_{sp2}, was made.

Table 6.2 shows for each pile the value of $R(\epsilon_{sp2})_{exp/dsgn}$, which is the ratio of the experimental to design (useable) strain at Δ_2. These ratios are plotted against the design useable spiral stress in Figure 6.9. Table 6.2 and Figure 6.9 show that, in all cases, the measured strains were equal to or greater than the design values. This was expected, since as explained in Chapter 2, the design values of spiral strains are based in part upon the values of longitudinal strain estimated using Equation 2.9, proposed by Richart et al. As stated in Chapter 2, and shown again in the preceding section, Equation 2.9 provides a conservative estimate of longitudinal strain, particularly for the higher strength spiral reinforcement.

Table 6.3 and Table 6.4 show similar trends for the stress values and values of confining pressure at Δ_2. It is noted that the ratios of experimental to design values were always higher when comparing strains as opposed to stresses; however, in every case the design value of f_{sp2} was either achieved or exceeded. The ratio of experimental to design useable stress, $R(f_{sp2})_{exp/dsgn}$ is plotted in Figure 6.10.

From the discussion presented above, it is clear that the proposed design method provides a reasonable to conservative estimate of the values of the spiral strains and stresses, and thus a reasonable to conservative estimate of the confining pressure provided by the spiral reinforcement.

6.4 COVER BEHAVIOR

As previously discussed in Chapter 4, the concrete cover generally failed in what can be characterized as a sudden manner when the first peak in the load-shortening response was achieved. In Specimens 14-B', 14-C', and 14-D', cover failure was sudden and complete. In Specimens 14-A', 14-E', and14- F', the cover failed suddenly, though perhaps more gradually than in Specimens 14-B', 14-C', and 14-D'. In the cases when the failure was more gradual, initial cover failure was characterized by an initial sudden large drop in load, followed then by failure of the remaining cover. Prior to P_1, few, if any, cracks were observed in the concrete cover. Upon reaching P_1, damage to the cover was evidenced by the formation of both longitudinal and circumferential cracking, located primarily within the test region of the pile specimens.

6.5 PILE FAILURE MECHANISMS

Failure in five of the six spirally-reinforced pile specimens (excluding Specimen 14-B') was defined by rupture of one or more turns of the spiral reinforcing wires and a subsequent loss of confining pressure on the concrete core. The result was a significant reduction in the load-carrying capacity of the pile. However, the test data suggests that the pile failures did not result from the spiral steel reaching their ultimate strains due to lateral expansion of the core concrete. The maximum strains in the spiral reinforcement as recorded by the spiral strain gages were well less than the ultimate

strains of the spiral wires. In fact, typical values of strain at the just prior to failure of the piles were less than one-third of the ultimate strains of the steels. Instead, pile failures can be attributed to failure of the concrete core, resulting in subsequent fracture of spiral wires.

The test summaries presented in Chapter 4 include the identification of all spiral fractures and occurrences of necking, as well as any indication of possible failure planes in the core concrete. Pile 14-F' was the only specimen found to exhibit a distinct failure plane in the concrete core, occurring at approximately 46 degrees of inclination from the horizontal. The pattern of fractures and necking in the spiral reinforcement in Pile 14-A' seemed to indicate a possible failure plane at about 43 degrees of inclination from the horizontal; however, no evidence of a failure plane was found in the core concrete. In two of the piles (14-D' and 14-E'), fracture of only one spiral wire was detected, with no necking evident at any other locations in the spiral reinforcement.

Graybeal et al. (1998) present a discussion on the failure mechanisms in spirally reinforced piles containing high strength concrete. Graybeal et al. concluded, based upon their research and previous work (Martinez, Nilson, and Slate (1984)), that high levels of lateral confinement of a high strength concrete (unconfined compressive strength greater than 8 ksi (55.2 MPa)) core may inhibit the formation of an inclined failure plane in the core concrete. If a failure plane should exist, the angle of inclination would be smaller than that for a moderately confined concrete core. The results of this research substantiate these claims, as only one failure plane was clearly observed in the core concrete, and it was found to have a relatively low angle of inclination.

6.6 COMPARISON OF EXPERIMENTAL AND PREDICTED INCREASES IN CONFINED CONCRETE STRENGTH

The magnitude of axial stress in the confined concrete core is determined from the axial force carried by the pile. To determine the stress in the core, the force carried by the longitudinal reinforcement is subtracted from the total force carried by the pile. The force in the longitudinal reinforcement is calculated from the average longitudinal strain gage strain in conjunction with the material properties given in Section 3.8.2. Since the spiral reinforcement carries no axial load, only the force carried by the concrete remains. Then, throughout the initial portion of the pile response from load initiation to P_1, the confined concrete stress, f_c, is determined by dividing the force carried by the concrete by the net concrete cross-sectional area of the pile. This is shown in Equation 6.2.

$$f_c = \frac{P - A_{lg} f_{lg}}{A_{c,total}} \quad \text{for } 0 \le P \le P_1 \tag{6.2}$$

After P_1 and until failure, f_c is determined by dividing the force carried by the concrete by the area of the concrete core, $A_{c,o\text{-}o}$. This core area is computed using the outside diameter of the spiral, which is the same definition used by Richart et al. (1928, 1929, 1934). This relationship is given by Equation 6.3.

$$f_c = \frac{P - A_{lg} f_{lg}}{A_{c,o-o}} \text{ for } P_{spall} \le P \le P_{fracture} \tag{6.3}$$

This method of calculating the core concrete stress assumes that the cover concrete is equally as effective in carrying axial load as the core concrete prior to cover failure, and that the cover carries no load after cover failure has occurred. As discussed in Section 6.4, for some of the piles, the cover concrete did not completely unload at cover failure, but instead failed in multiple stages until P_{spall} was achieved. However, this does not affect the discussions or conclusions that follow.

The experimentally determined increase in the strength of the confined concrete core, $\Delta f_{c12,exp}$, is computed as the stress in the confined core at the second peak, f_{c2}, minus the unconfined compressive strength, f_{co}. This is given as Equation 6.4.

$$\Delta f_{c12,exp} = f_{c2} - f_{co} \tag{6.4}$$

The remainder of this section compares this experimental increase in strength of the confined core to the design value of the increase in strength of the confined core, $\Delta f_{c12,dsgn}$ and to the value of the increase in strength of the confined core calculated from the stress in the spiral reinforcement, $\Delta f_{c12,rich}$.

The value of $\Delta f_{c12,dsgn}$ is calculated from Equation 6.5, which is a combination of Equations 2.4 and 2.8.

$$\Delta f_{c12,dsgn} = 2.05 \rho_{sp} f_{sp2,dsgn} \tag{6.5}$$

The value of $\Delta f_{c12,rich}$ is computed from Equation 6.6, which is a combination of Equations 2.4 and 2.8, along with the stress in the spiral steel at Δ_2, $f_{sp2,exp}$, as shown in Table 6.2.

$$\Delta f_{c12,rich} = 2.05 \rho_{sp} f_{sp,exp} \tag{6.6}$$

Table 6.5 shows the experimental and design values for Δf_{c12}. The last column in the table shows the value of $R(\Delta f_{c12})_{exp/dsgn}$, which is the ratio of $\Delta f_{c12,exp}$ to $\Delta f_{c12,dsgn}$. This ratio is plotted versus the design value of useable stress of the spiral reinforcement for each pile in Figure 6.11. Table 6.5 and Figure 6.11 show that Specimens 14-A', 14-C', and 14-D' either achieved or exceeded the predictions of core strength enhancement based on the spiral design useable stress. For these piles, $R(\Delta f_{c12})_{exp/dsgn}$ ranged from 1.00 to 1.14. In contrast, Specimens 14-E' and 14-F' fell approximately 20 percent below the predicted values.

Table 6.6 shows the experimental and Richart et al. predicted values of Δf_{c12}. The last column in the table shows the value of $R(\Delta f_{c12})_{exp/rich}$, which is the ratio of $\Delta f_{c12,exp}$ to $\Delta f_{c12,rich}$. This ratio is also plotted versus the design value of useable stress of the spiral reinforcement for each pile in Figure 6.12. Table 6.6 and Figure 6.12 show that Specimens 14-A' and 14-C' satisfied the Richart et al. prediction of increased compressive strength of the concrete core. Specimen 14-D' nearly satisfied the prediction, falling short by only 5 percent. However, Specimens 14-E' and 14-F' achieved only

67 percent and 69 percent of the Richart et al. predictions. These ratios show that the first three piles exhibited experimental core strength increases consistent with the stresses observed in the spiral steel, but the last two piles did not. Therefore, from the results of this study presented thus far, the Richart et al. prediction may have a limit on its range of applicability for higher strength steels. The Richart et al. prediction is given by Equation 6.7, which is Equation 2.8, rewritten to solve for f_{c2}.

$$f_{c2} = f_{co} + 4.1 f_{2-2} \tag{6.7}$$

Equation 6.7 is a well-tested and widely accepted relationship between the confining pressure and increased core strength in laterally confined members. Therefore, its inadequacy to predict the behavior of the piles with the higher strength spiral reinforcement (Specimens 14-E' and 14-F') is somewhat surprising. Thus, a further examination of the specimen parameters and test data is necessary in order to understand the behavior of these members. This is treated further in Section 6.9.

6.7 DILATION RATIO RELATIONSHIPS

As part of the procedure for the design of high strength spiral reinforcement for concrete piles proposed by Graybeal et al., Equation 2.9 is used to estimate the longitudinal strain in the concrete core at Δ_2. Also needed in the design procedure is a means to estimate the transverse strain from the longitudinal strain. The dilation ratio is used for that purpose. Much of the background information related to this discussion was presented in Section 2.3.5. Therefore, only brief descriptions of the relationships are provided here.

6.7.1 Definitions

The dilation ratio is a general means to describe the relationship between transverse strain and longitudinal strain of the concrete core. More specifically, the secant dilation ratio, η_{sec}, is defined as the ratio between transverse and longitudinal strain at any point in the response of the core. This relationship is represented by Equation 2.14.

$$\eta_{sec} = \frac{\varepsilon_{ct}}{\varepsilon_c} \tag{2.14}$$

If known, the secant dilation ratio can be used to compute the transverse strain at any point based on the value of the longitudinal strain. If η_{sec} and the longitudinal strain are known at a point, the transverse strain can be calculated directly.

The tangent dilation ratio, η_{tan}, is defined as the slope of the curve of the transverse strain versus longitudinal strain at any point along the curve. Equation 2.15 defines the tangent dilation ratio at any point.

$$\eta_{tan} = \frac{d\varepsilon_{ct}}{d\varepsilon_c} \tag{2.15}$$

In order to calculate the transverse strain in the concrete which corresponds to any longitudinal strain, the relationship between transverse strains and longitudinal strains is needed for all values of longitudinal strain prior to that point. Equation 6.8 defines the total transverse strain as a function of the total longitudinal strain and η_{tan}.

$$\varepsilon_{ct} = \int_{\varepsilon_c=0}^{\varepsilon_c} \eta_{tan} d\varepsilon_c \tag{6.8}$$

Equation 6.8 shows that the area under the η_{tan} curve between $\epsilon_c = 0$ and ϵ_c is ϵ_{ct}.

6.7.2 Experimentally Determined Dilation Ratios

Part (a) of Figures 6.13 through 6.17 shows the experimentally determined strain in the spiral reinforcement for each of the spiral strain gages, versus the average longitudinal strain in the concrete for each specimen. The strains in the spiral reinforcement are assumed to be equal to the strains in the concrete. Also, the average strain in the longitudinal reinforcement is assumed to be equal to the longitudinal strain in the concrete. The results are shown for each pile from $\epsilon_c = 0$ to ϵ_{c2}. Also, the average longitudinal strains at two key points in the response, ϵ_{c1} and ϵ_{c2}, are noted on the figures.

Part (b) of Figures 6.13 through 6.17 shows the experimentally determined secant dilation ratio for each of the spiral strain gages throughout the tests for each pile. The secant dilation ratio for each spiral gage was calculated as the spiral strain divided by the average longitudinal strain gage strain. The approximated secant dilation ratio at the second peak, η_{sec2}, is also noted on these plots. These values are approximated based on the trends observed in the individual η_{sec} curves for each pile. For each pile, this is the value which directly relates ϵ_{c2} to ϵ_{ct2} as is shown in Equation 2.16.

$$\varepsilon_{ct2} = \eta_{sec2} \varepsilon_{c2} \tag{2.16}$$

In general, these plots show that the secant dilation behavior of the pile specimens was either constant or decreasing until ϵ_{c1} was approached. This was expected, as confined concrete under low axial compressive stresses exhibits a nearly constant relationship between longitudinal and transverse strains. (MacGregor, 1992) Between ϵ_{c1} and ϵ_{c2}, the plots show that the general trend was a slight increase in η_{sec}. This also was expected as confined concrete under higher axial loads normally exhibits larger transverse strains per longitudinal strain than it did under lower axial loads. (MacGregor, 1992) The approximated values of η_{sec2}, denoted on each figure, ranged from 0.35 to 0.55. It is noted from the plots that the piles comprised of the higher strength spiral steels experienced greater dilation as the lower volumetric quantities of the spiral reinforcement permitted greater expansion of the core.

Part (c) of Figures 6.13 through 6.17 shows the experimentally determined tangent dilation ratio for each pile. For each pile, the curve, which is a plot of tangent dilation ratio versus average longitudinal strain (the heavier line in the figures), was determined as follows. First, the increment of transverse strain was calculated for each increment of longitudinal strain throughout the response of the pile. This calculation was performed for each of the spiral strain gages for each increment of longitudinal strain. The result was a plot of tangent dilation ratio versus average longitudinal

strain for each of the spiral strain gages. These individual curves were then averaged to generate the thinner curve shown in the figures. The somewhat erratic oscillations of the curve are attributed to the incremental approach used to determine the curve. Because of the frequency of data points taken, the value of average longitudinal strain may not have increased very much, if at all, between successive readings, causing large changes in the tangent dilation ratio at specific points. Finally, to reduce these erratic oscillations, this average curve was smoothed by taking a moving average of the ten values of η_{tan} closest to each value of η_{tan} for each longitudinal strain increment. This smoothed average curve is the heavier curve shown in the figures.

As was discussed in Section 6.7.1, the area under the η_{tan} curve up to any longitudinal strain is equal to the transverse strain at that longitudinal strain. Therefore, the area under the smoothed η_{tan} curve between $\epsilon_c = 0$ and ϵ_{c2} was calculated using Equation 6.8 and is shown on each of the figures, denoted as $A_{\eta tan2}$. This area is equal to the transverse strain ϵ_{ct2}. This is expressed in equation form in Equation 2.17.

$$\varepsilon_{ct2} = A_{\eta tan2} \tag{2.17}$$

The area under the smoothed η_{tan} curve is shown on each figure, denoted as $A\eta_{tan2}$. The plots show that η_{tan} is approximately constant from $\epsilon_c = 0$ to nearly ϵ_{c1}. This was expected as the concrete in this range of the response is behaving more or less as if it were unconfined with a constant Poisson's ratio. (MacGregor, 1992) The plots show that the concrete exhibits a higher dilation ratio after cover spalling. This was also expected as the confined concrete under high axial compressive stresses should exhibit increased dilation due to the microcracking and microcracking. (MacGregor, 1992) Finally, the figures show that the tangent dilation ratio is nearly constant around ϵ_{c2}. It is possible that the confining stresses produced by the spirals limited the dilation of the core to a certain value.

6.7.3 Evaluation of Secant and Tangent Dilation Ratios

Table 6.7 compares the experimentally determined values of transverse strain at $\Delta_2, \epsilon_{ct2,exp}$ with the values of transverse strain obtained using the experimentally determined secant and tangent dilation ratios ($\epsilon_{ct2,sec}$ and $\epsilon_{ct2,tan}$). In the table, the experimental value of $\epsilon_{ct2,exp}$ was determined from the spiral strain gage measurements at Δ_2, ϵ_{sp2}, shown in Table 6.2. $\epsilon_{ct2,sec}$ was computed from Equation 2.16 and the experimental value of ϵ_{c2} (listed in Table 6.7). The approximated values of η_{sec2} for each pile are shown in part (b) of Figures 6.13 through 6.17, as well as in Table 6.7. $\epsilon_{ct2,tan}$ was computed from Equation 2.17. The area under the η_{tan} curve at ϵ_{c2}, $A_{\eta tan2}$, is shown in part (c) of Figures 6.13 through 6.17 as well as in Table 6.7.

Listed in Table 6.7 is the value of $R(\epsilon_{ct2})_{exp/sec}$, which is the ratio of the experimental value of $\epsilon_{ct2,exp}$ determined from the spiral strain gage measurements, to $\epsilon_{ct2,sec}$, the experimentally determined value of transverse strain obtained using the secant dilation ratio. The table shows that in every case except one (Specimen 14-A'), $\epsilon_{ct2,sec}$ was greater than the experimentally obtained value. The disagreement between $\epsilon_{ct2,exp}$ and $\epsilon_{ct2,sec}$ was limited to 18 percent for four of the five piles, but for Specimen 14-D', $\epsilon_{ct2,sec}$ exceeded $\epsilon_{ct2,exp}$ by 41 percent.

Also listed in Table 6.7 is the value of $R(\epsilon_{ct2})_{exp/tan}$, which is the ratio of the experimental value of $\epsilon_{ct2,exp}$ determined from the spiral strain gage measurements, to $\epsilon_{ct2,tan}$, the experimentally determined value of transverse strain obtained using the tangent dilation ratio. The table shows that the tangent dilation ratio values of the transverse strain, $\epsilon_{ct2,tan}$ are generally consistent with the experimentally determined values, $\epsilon_{ct2,exp}$. However, it is noted that for Specimens 14-C', 14-D', and 14-E', all of the spiral gages failed prior to ϵ_{c2}. This led to an artificially low value of $A_{\eta tan2}$. To gain an approximation of the value of $A_{\eta tan2}$ that may have been obtained had all of the spiral gages not failed, the curves were extended by a constant value, equal to the last value just prior to failure of all spiral gages, up to $\epsilon_{c2,}$ and new values of $A_{\eta tan2}$ were computed. The extensions of the curves are shown as heavy dashed lines in part (c) of Figures 6.13 through 6.17. These estimated areas and the corresponding ratios are also shown in Table 6.7, enclosed in parentheses. After extending the η_{tan} curves to ϵ_{c2}, for the most part, the values of $\epsilon_{ct2,tan}$ slightly exceed the experimentally observed values, $\epsilon_{ct2,exp}$.

In summary, in most cases, the estimates of ϵ_{ct2} using the secant and tangent dilation ratios provide reasonable estimates of the transverse strain as measured by the strain gages in the spiral reinforcement. For all of the piles treated in this study, the average values of $R(\epsilon_{ct2})_{exp/sec}$ and $R(\epsilon_{ct2})_{exp/tan}$ were both found to be 0.86. However the values of $R(\epsilon_{ct2})_{exp/sec}$ ranged from 0.59 to 1.03, while the values of $R(\epsilon_{ct2})_{exp/tan}$ ranged from 0.78 to 0.97, based on the extended curves. Therefore, because of the smaller range, the tangent dilation ratio approximation provides a slightly better estimation of the experimental values of ϵ_{ct2}.

6.7.4 Comparison of Proposed and Experimental Tangent Dilation Ratio Relationships

As stated in Chapter 2, as part of their proposed design procedure, Graybeal et al. needed a means to calculate the transverse strain in the concrete core from the longitudinal strain. After examination of the test data and previous work of other researchers, Graybeal et al. developed a tangent dilation ratio relationship for this purpose. The proposed tangent dilation ratio relationship was reviewed in Section 2.3.5 and is expressed as Equation 2.21.

$$A_{\eta tan2} = \varepsilon_{co}(m(0.41) - 0.105) \tag{2.21}$$

Recalling that $A_{\eta tan2}$ equals ϵ_{ct2} and $m = \epsilon_{c2}/\epsilon_{co}$, this equation is rewritten as Equation 2.10.

$$\varepsilon_{ct2} = 0.41\varepsilon_{c2} - 0.105\varepsilon_{co} \tag{2.10}$$

For their work, Graybeal et al. found that this relationship provided conservative predictions of the transverse strain.

The proposed tangent dilation ratio relationship was also evaluated in this work. Figure 6.18 shows the experimentally determined tangent dilation ratio curves with the longitudinal strains normalized by ϵ_{co}. Also shown on each plot is the proposed tangent dilation relationship for the respective specimen. A comparison of the curves reveals the following. The initial portion of the proposed curve models the data well, providing a slightly conservative estimate of the actual behavior. In the second part of the curve, the data becomes erratic. However, it appears that the proposed curve

provides a reasonable approximation of the experimental data. The third part of the curve appears to have provided a satisfactory model of the limited experimental data.

Table 6.8 provides a numerical comparison between the proposed and experimental tangent dilation ratio relationships. Included in the table are experimental values for m, which is given by Equation 2.18 as the ratio of the longitudinal strain at Δ_2, ϵ_{c2}, to the strain corresponding to the unconfined compressive strength of the concrete, ϵ_{co}. Also included are values of $\bar{A}_{\eta tan2,exp}$ and $\bar{A}_{\eta tan2,prpsd}$, which represent the areas under the experimental and proposed normalized tangent dilation ratio curves, respectively. For Specimens 14-C', 14-D', and 14-E', two values of $\bar{A}_{\eta tan2,exp}$ are given, with the value in parentheses determined using the dashed line extension of the dilation ratio plots in Figures 6.18 (b), (c), and (d).

Table 6.8 also provides values for $\epsilon_{ct2,exp}$ and $\epsilon_{ct2,prpsd}$, which are the experimentally determined values of transverse strain as obtained from strain gages readings on the spirals and the predicted values of transverse strain from the proposed tangent dilation ratio relationship given by Equation 2.10.

6.8 APPLICABILITY OF THE PROPOSED DESIGN PROCEDURE

The primary objective of this research was to evaluate the validity of the design procedure proposed by Graybeal et al. for the design of high strength spiral reinforcement for prestressed concrete piles under concentric axial compression. From the results of the research it is concluded that the proposed design procedure provides satisfactory spiral designs for the piles made of the steels studied by Graybeal et al. The useable stresses of these steels ranged from 79 ksi (545 MPa) to 110 ksi (758 MPa).

The piles made with the two higher strength steels, whose useable stresses were 164 ksi (1131 MPa) and 161 ksi (1110 MPa), did not achieve their design capacities. Therefore, based upon the results of this research, it is concluded that the proposed design procedure can be used for spiral steels with useable stress values up to 110 ksi (758 MPa). This conclusion is applicable to the pile geometries (i.e. including the 24 in. (610 mm) diameter piles) and material strengths treated in this study and the earlier study by Graybeal et al.

It is concluded that the proposed design procedure is also applicable to the larger diameter (24 in. (610 mm) diameter piles) piles because the core strength of these piles could be predicted using Equation 6.7 and the actual stress in the spiral at Δ_2. Redesign of these piles using the proposed design procedure would result in an increase in the amount of spiral reinforcement in the piles. This will result in an increase in the stiffness and confining stress at any value of spiral strain (and hence at any value of transverse strain in the core) in these redesigned piles. As a result, as shown in Section 6.9, the proposed design approach is therefore expected to be applicable in this case, too.

Three key relationships used in the design procedure were demonstrated to provide acceptable results for design purposes for spiral steels with useable stress values up to 110 ksi (758 MPa). First, the Richart et al. (1928, 1929, 1934) estimate of longitudinal strain (Equation 2.9) provides

reasonable to conservative estimates of longitudinal strain at Δ_2, with the more conservative estimates made for the higher useable stress spirals. Second, the tangent dilation ratio relationship proposed by Graybeal et al. (Equation 2.10) was found to slightly underestimate the value of transverse strain at peak concrete core strength. The result of these first two relationships is that the proposed design procedure provides conservative estimates of strains and stresses in the spiral reinforcement at Δ_2, and thus conservative estimates of the confining stress on the core concrete at Δ_2. Finally, the Richart et al. estimate of increase in concrete core strength due to spiral confinement (Equation 6.7) was found to be valid for the piles made with useable stress values up to 110 ksi (758 MPa).

6.9 LIMITATIONS OF THE PROPOSED DESIGN PROCEDURE

The findings discussed earlier in this chapter indicate that there are limitations on the range of applicability of the design procedure proposed by Graybeal et al. Earlier in this chapter it was noted that: (1) The Richart et al. prediction of longitudinal strain (Equation 2.9) provides reasonable to conservative estimates of longitudinal strain at Δ_2, with the more conservative estimates made for the higher useable stress spirals; (2) The proposed design procedure provides conservative estimates of strains and stresses in the spiral reinforcement at Δ_2, and thus conservative estimates of the confining stress on the core concrete at Δ_2. Despite these findings, it was also found that for Specimens 14-E' and 14-F', the experimentally observed increase in compressive strength of the core concrete at Δ_2 was less than the increase that is predicted using Richart et al. Equation 6.7. This last finding indicates that there is a limit to the range applicability of the design procedure proposed by Graybeal et al.

Four factors may contribute to the finding that the Richart et al. equation fails to accurately estimate the strength increase in the confined core of Specimens 14-E' and 14-F'. These factors are: (1) the area of the effectively confined core; (2) the in-situ stress-strain curve for the spiral reinforcement; (3) the stiffness of the spiral reinforcement at any value of spiral strain; and (4) the confining stress created by the spiral reinforcement at any value of spiral strain. Each of these factors is discussed further in the sections that follow.

6.9.1 Effective Core Area

Mander, Priestley and Park (1988) proposed a correction factor to compute the effectively confined core area as a fraction of the total core area. The effectively confined core area can be less than the total core area because confinement is actually provided to the core at the discrete locations of the spiral. Regions of the core away from the location of the spiral are therefore confined less effectively. Using the Mander et al. model, the values of confining pressure for Specimens 14-E' and 14-F' should be reduced the most (6-9 percent for 14-E' and 14-F', 3-4 percent for 14-A', 14-C', and 14-D'), since the clear spacing between the spirals is the greatest for these piles. Clearly, the issue of the effectively confined core area can explain at most only a small part of the observation that the experimentally observed increase in compressive strength of the core concrete at Δ_2 was less than the increase that is predicted using Richart et al. Equation 6.7.

6.9.2 In-Situ Stress-Strain Curve of the Spiral Reinforcement

A second possible factor contributing to the deviation between the experimental and design results for Specimens 14-E' and 14-F' was the selection of the stress-strain curve of the spiral steel used in the design of each pile. As mentioned before, the design of Specimens 14-A' through 14-D' was based upon useable stresses determined from stress-strain curves from tension tests on straightened segments of the respective spiral wires. For Specimens 14-E' and 14-F', the design was based on useable stresses obtained from the stress-strain curves from unspiraled wires.

Section 2.3.4, as well as Chapter 5, presented discussions of the impact of using these particular curves in design. The numerical analyses performed showed significant rounding or softening of the stress-strain curves at strain values near where the useable stress values were extracted. Thus the actual useable stress values were overestimated, and, as a consequence, the piles may have been under-designed. The analyses presented in Chapter 5 showed that an error of about 15 percent may have been incurred by basing the useable stress values on curves from tests on unspiraled wires as opposed to wires in their in-situ spiraled state. Had spiraled-straightened wires been used in the design, the analyses showed that the design error could have been reduced to about 10 percent.

6.9.3 Stiffness of the Spiral Reinforcement

A third possible factor contributing to the deviation between the experimental and design results for Specimens 14-E' and 14-F' is the differences in stiffnesses of the spiral reinforcement. Because the spirals for each pile were designed to provide equal confining pressures, a smaller volumetric ratio of spiral steel was used for Specimens 14-E' and 14-F' as compared to the remainder of the specimens.

The stiffness of the spiral reinforcement was calculated for each pile as the product of the area of the spiral reinforcement and the elastic modulus of the steel, divided by the pitch of the spiral reinforcement. For Specimen 14-A', the area of a wire is doubled due to the bundled bars. Plots were created of the stiffness of the spiral reinforcement versus spiral strain (hence versus transverse strain in the core) for each pile, taking into account the changing elastic modulus of the spiral steel. The results are presented in Figure 6.19 as curves of spiral stiffness versus spiral strain. The curves are plotted for each specimen up to the value of spiral strain exhibited at Δ_2. These figures clearly show large differences in the initial stiffnesses of the spirals in the different specimens, with the smallest stiffnesses exhibited by the spirals with the highest useable stresses. For example, the value of initial stiffness of the spiral of Specimen 14-F' was 45 percent of that of Specimen 14-A'.

Finally, it is noted in Figure 6.19 that the general appearance of the curves of Specimens A', C' and D' differ from the general appearance of the curves of Specimens E' and F'. This is a result of differences in how the curves were fitted to the experimental stress-strain data. Stress-strain curves A', C' and D' were fit using smooth curves for their entire response. The initial portion of the stress-strain curves for E' and F' were much more linear than the other wires. Thus the initial stress-strain curve was fitted as a straight line for these two wires.

6.9.4 Variable Confining Stress Provided by the Spiral Reinforcement

The Richart et al. prediction of confined strength of core concrete is based in large part on tests of piles with relatively low strength (mild steel) spiral reinforcement, and on tests of cylinders where a constant lateral pressure was applied using a pressurized fluid. In both instances, the confining pressure is approximately constant (for a mild steel, the lateral confining stress is constant once the spiral yields). A different situation is obtained where confinement is provided by high strength spiral reinforcement. When high strength spirals are used, the confining pressure varies throughout the axial load response of the core. In such situations, a variable confinement model must be used to attempt to predict the response of the core (Kestner 1997).

Plots were created of the confining stress provided by the spiral reinforcement versus spiral strain (hence versus transverse strain in the core) for each pile. The results are presented in Figure 6.20 as curves of confining stress versus spiral strain. The curves are plotted for each specimen up to the value of spiral strain exhibited at Δ_2. These figures clearly show that, at values of strain below ϵ_{sp2}, there are large differences in the value of confining stress generated by the spirals in the different specimens, with the smallest confining stresses exhibited by the spirals with the highest useable stresses.

Based on the discussion presented above, it is clear that further research is needed to understand and explain the influences of spiral stiffness and variable confining pressures throughout the response of a pile on the resulting strength enhancement of the concrete core.

Pile	Experimental					Design		Richart et al.		Cusson and Paultre	
	ε_{co}	f_{co} (ksi)	f_{c2} (ksi)	$f_{2\text{-}2}$ (ksi)	$\varepsilon_{c2,exp}$	$\varepsilon_{c2,dsgn}$	$R(\varepsilon_{c2})_{exp/dsgn}$	$\varepsilon_{c2,rich}$	$R(\varepsilon_{c2})_{exp/rich}$	$\varepsilon_{c2,cus}$	$R(\varepsilon_{c2})_{exp/cus}$
14-A'	0.0027	7.55	15.29	1.88	0.0153	0.0158	0.97	0.0165	0.93	0.0225	0.68
14-C'	0.0027	7.55	15.36	1.90	0.0219	0.0158	0.39	0.0167	1.31	0.0228	0.96
14-D'	0.0027	7.55	16.36	2.27	0.0344	0.0158	2.18	0.0185	1.86	0.0299	1.15
14-E'	0.0027	7.55	13.65	2.22	0.0231	0.0158	1.46	0.0136	1.70	0.0289	0.80
14-F'	0.0027	7.55	13.83	2.22	0.0206	0.0158	1.30	0.0139	1.48	0.0289	0.71

1 ksi = 6.895 MPa

Table 6.1 Comparison of experimental longitudinal strain at Δ_2 to values predicted by Richart et al. (1928, 1929, 1934) and Cusson and Paultre (1995).

Pile	$\varepsilon_{sp2,dsgn}$	Δ_1	Δ_{spall}	Δ_2	$R(\varepsilon_{sp2})_{exp/dsgn}$
		Approximate Spiral Strain, ε_{sp1}	Approximate Spiral Strain, $\varepsilon_{sp,spall}$	Approximate Spiral Strain, ε_{sp2}	
14-A'	0.0062	0.00061	0.0012	0.0063†	1.02
14-B'	0.0062	0.00071	0.0014	-	-
14-C'	0.0062	0.00140	0.0020	0.0063†	1.02
14-D'	0.0062	0.00096	0.0018	0.0091†	1.47
14-E'	0.0062	0.00156	0.0031	0.0122†	1.97
14-F'	0.0062	0.00091	0.0022	0.0086†	1.39

† indicates an approximation based on trends observed in the spiral strain vs. axial shortening plots in Chapter 4.

Table 6.2 Approximate strains in the spiral reinforcement at Δ_1, Δ_{spall}, and Δ_2.

Pile	Design Useable Stress $f_{sp2,dsgn}$ (ksi)	Δ_1			Δ_{spall}			Δ_2			
		Spiral Stress		Approximate Spiral Stress, f_{sp1} (ksi)	Spiral Stress		Approximate Spiral Stress, $f_{sp,spall}$ (ksi)	Spiral Stress		Approximate Spiral Stress, $f_{sp2,exp}$ (ksi)	$R(f_{sp2})_{exp/dsgn}$
		Min. (ksi)	Max. (ksi)		Min. (ksi)	Max. (ksi)		Min. (ksi)	Max. (ksi)		
14-A'	79	13.4	21.4	17	27.5	38.4	34	77.7	81†	79	1.00
14-B'	104	16.1	28.4	22	37.3	43.5	41	-	-	-	-
14-C'	108	33.5	52.0	40	47.0	61.4	55	101†	113†	109	1.01
14-D'	110	17.7	31.5	25	33.1	65.4	48	127†	138†	133	1.21
14-E'	164	34.5	48.4	42	62.6	117.8	82	192†	197†	194	1.18
14-F'	161	18.0	30.6	24	42.3	83.4	58	182.5	223†	190	1.18

† indicates an approximation of the minimum or maximum value based on trends observed in spiral strain vs. axial shortening plots in Chapter 4
1 ksi = 6.895 MPa

Table 6.3 Minimum, maximum, and approximate stresses in the spiral reinforcement at Δ_1, Δ_{spall}, and Δ_2.

Pile	ρ_{sp} %	Δ_1		Δ_{spall}		Δ_2	
		f_{sp1} (ksi)	$f_{2\text{-}1}$ (ksi)	$f_{sp,spall}$ (ksi)	$f_{2\text{-}spall}$ (ksi)	f_{sp2} (ksi)	$f_{2\text{-}2}$ (ksi)
14-A'	4.76	17	0.40	34	0.81	79	1.88
14-B'	3.62	22	0.40	41	0.74	-	-
14-C'	3.48	40	0.71	55	0.96	109	1.90
14-D'	3.42	25	0.44	48	0.82	133	2.27
14-E'	2.29	42	0.48	82	0.94	194	2.22
14-F'	2.34	24	0.28	58	0.68	190	2.22

1 ksi = 6.895 MPa

Table 6.4 Confining pressure on concrete core at Δ_1, Δ_{spall}, and Δ_2.

Pile	Experimental			Design			$R(\Delta f_{c12})_{exp/dsgn}$
	P_2 (kips)	f_{c2} (ksi)	$\Delta f_{c12,exp}$ (ksi)	$f_{sp2,dsgn}$ (ksi)	$f_{2\text{-}2}$ (ksi)	$\Delta f_{c12,dsgn}$ (ksi)	
14-A'	1245	15.29	7.74	79	1.88	7.71	1.00
14-C'	1250	15.36	7.81	108	1.88	7.70	1.01
14-D'	1328	16.36	8.81	110	1.88	7.71	1.14
14-E'	1117	13.65	6.10	164	1.88	7.70	0.79
14-F'	1131	13.83	6.28	161	1.88	7.72	0.81

1 kip = 4.448 kN
1 ksi = 6.895 MPa

Table 6.5 Comparison of experimental peak core concrete strength increase to design value of core concrete strength increase.

Pile	Experimental			Richart et al.			$R(\Delta f_{c12})_{exp/rich}$
	P_2 (kips)	f_{c2} (ksi)	Δf_{c12} (ksi)	$f_{sp2,exp}$ (ksi)	$f_{2\text{-}2}$ (ksi)	$\Delta f_{c12,rich}$ (ksi)	
14-A'	1245	15.29	7.74	79	1.88	7.71	1.00
14-C'	1250	15.36	7.81	109	1.90	7.78	1.00
14-D'	1328	16.36	8.81	133	2.27	9.32	0.95
14-E'	1117	13.65	6.10	194	2.22	9.11	0.67
14-F'	1131	13.83	6.28	190	2.22	9.11	0.69

1 kip = 4.448 kN
1 ksi = 6.895 MPa

Table 6.6 Comparison of experimental peak core concrete strength increase to strength increase based on Richart et al. (1928, 1929, 1934) prediction.

Pile	Experimental		Secant Dilation Ratio		Tangent Dilation Ratio	$R(\varepsilon_{ct2})_{exp/sec}$	$R(\varepsilon_{ct2})_{exp/tan}$
	$\varepsilon_{c2,exp}$	$\varepsilon_{ct2,exp}$	η_{sec2}	$\varepsilon_{ct2,sec}$	$\varepsilon_{ct2,tan} = A_{\eta tan2}$		
14-A'	0.0153	0.0063	0.40	0.0061	0.0067	1.03	0.94
14-C'	0.0219	0.0063	0.35	0.0077	0.0054 (0.0066)	0.82	1.17 (0.97)
14-D'	0.0344	0.0091	0.45	0.0155	0.0079 (0.0108)	0.59	1.15 (0.84)
14-E'	0.0231	0.0122	0.55	0.0127	0.0105 (0.0157)	0.96	1.16 (0.78)
14-F'	0.0206	0.0086	0.45	0.0093	0.0109	0.92	0.79

NOTE: For Specimens 14-C', 14-D', and 14-E', values in parentheses represent projected areas of the total area under the η_{tan} vs. average longitudinal strain curves from $\varepsilon_c = 0$ to ε_{c2}. These values are necessary due to failure of all spiral strain gages before ε_{c2} in these specimens.

Table 6.7 Comparison of experimentally determined values of transverse strain at Δ_2 with the values obtained using the secant and tangent dilation ratios.

Pile	Experimental			Proposed Tangent Dilation Ratio	
	m	$\bar{A}_{\eta tan2,exp}$	$\varepsilon_{ct2,exp}$	$\bar{A}_{\eta tan2,prpsd}$	$\varepsilon_{ct2,prpsd}$
14-A'	5.66	2.50	0.0063	2.22	0.0060
14-C'	8.10	1.99 (2.44)	0.0063	3.22	0.0087
14-D'	12.74	2.94 (4.01)	0.0091	5.12	0.0138
14-E'	8.55	3.88 (5.80)	0.0122	3.40	0.0092
14-F'	7.64	4.02	0.0086	3.03	0.0082

NOTE: For Specimens 14-C', 14-D', and 14-E', values in parentheses represent projections of the total area under the η_{tan} vs. normalized average longitudinal strain curves from $\varepsilon_c = 0$ to ε_{c2}. These values are necessary due to failure of all spiral strain gages before ε_{c2} for these specimens.

Table 6.8 Comparison of experimental values of tangent dilation ratio relationships to values obtained from the relationship proposed by Graybeal et al. (1998).

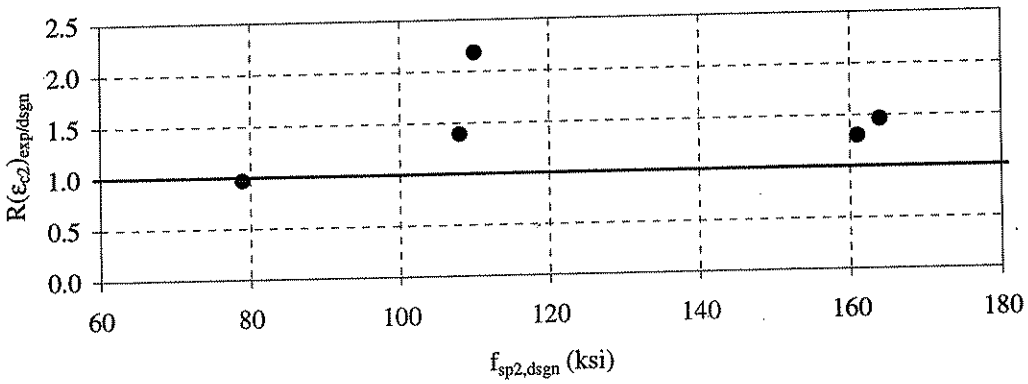

Figure 6.1 Ratio of experimental to design ε_{c2}.

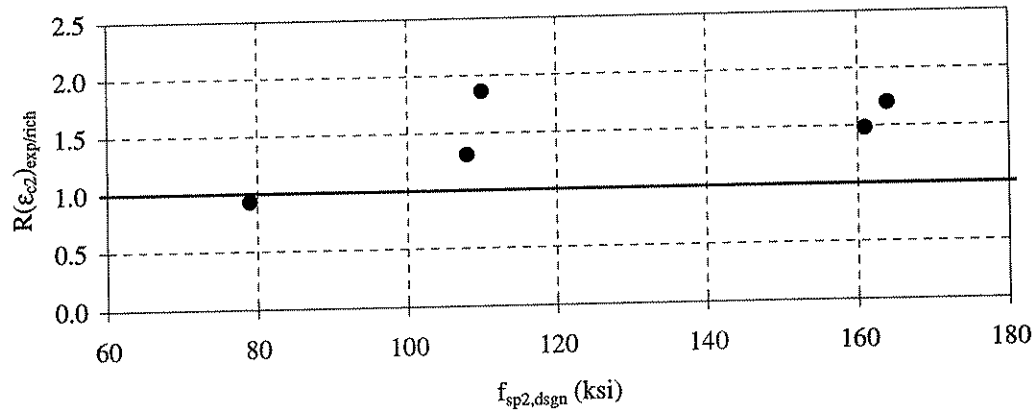

Figure 6.2 Ratio of experimental to Richart et al. ε_{c2}.

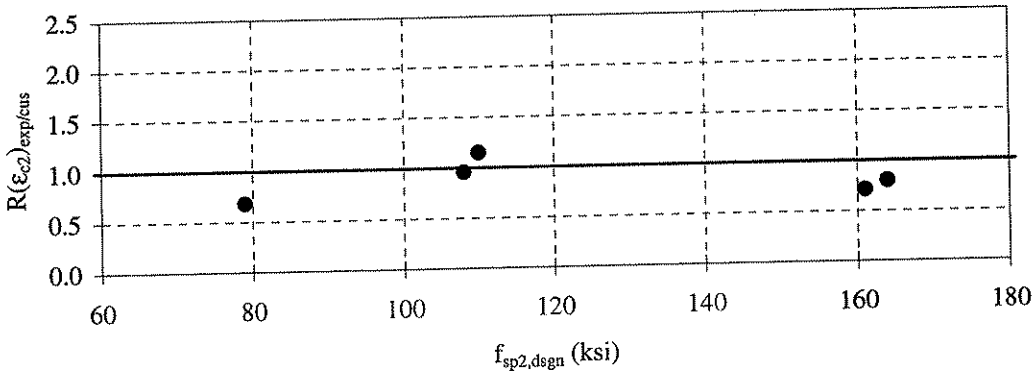

Figure 6.3 Ratio of experimental to Cusson et al. ε_{c2}.

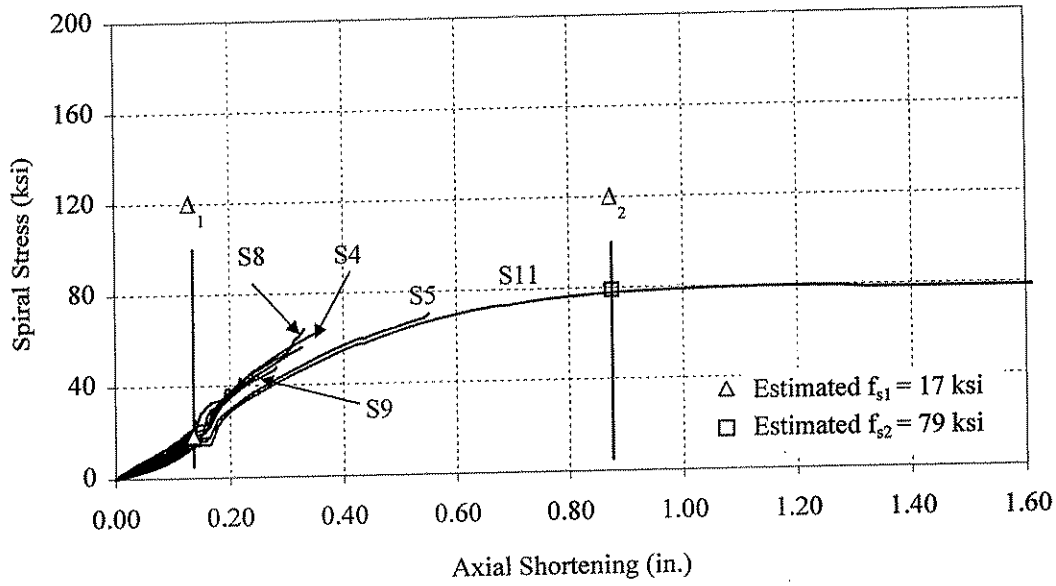

Figure 6.4 Plot of spiral stress versus axial shortening for Specimen 14-A'.

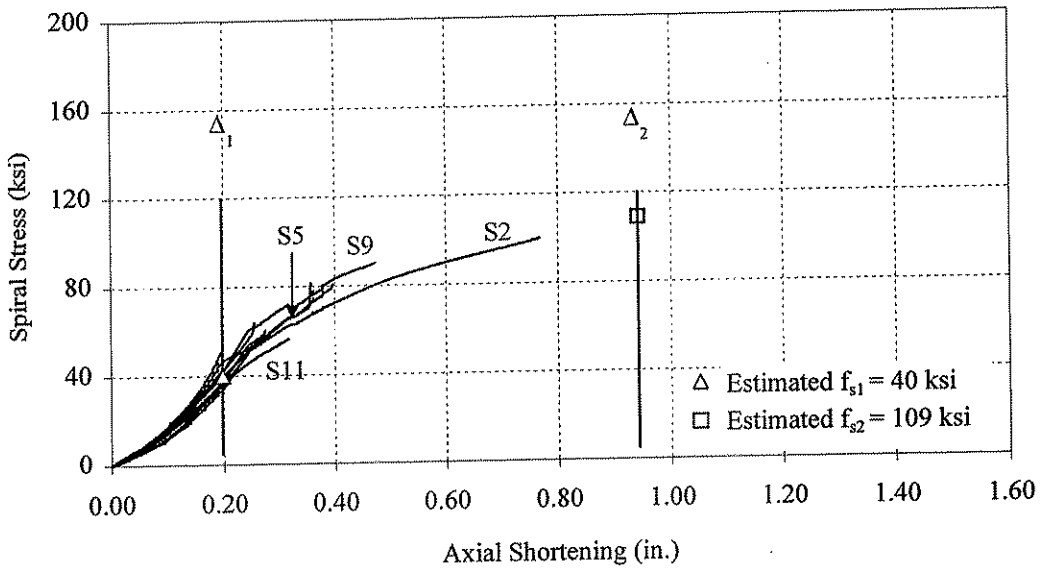

Figure 6.5 Plot of spiral stress versus axial shortening for Specimen 14-C'.

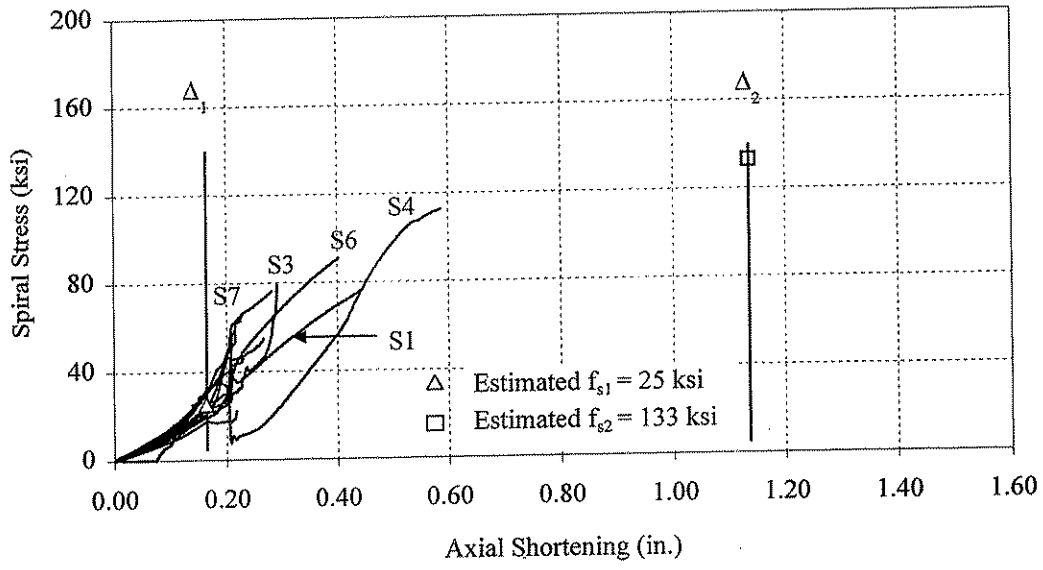

Figure 6.6 Plot of spiral stress versus axial shortening for Specimen 14-D'.

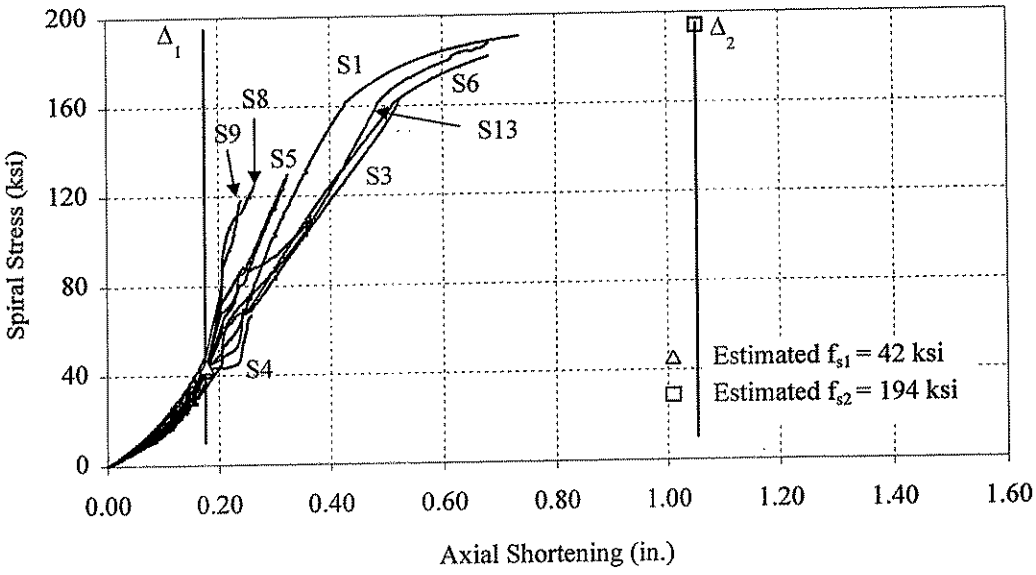

Figure 6.7 Plot of spiral stress versus axial shortening for Specimen 14-E'.

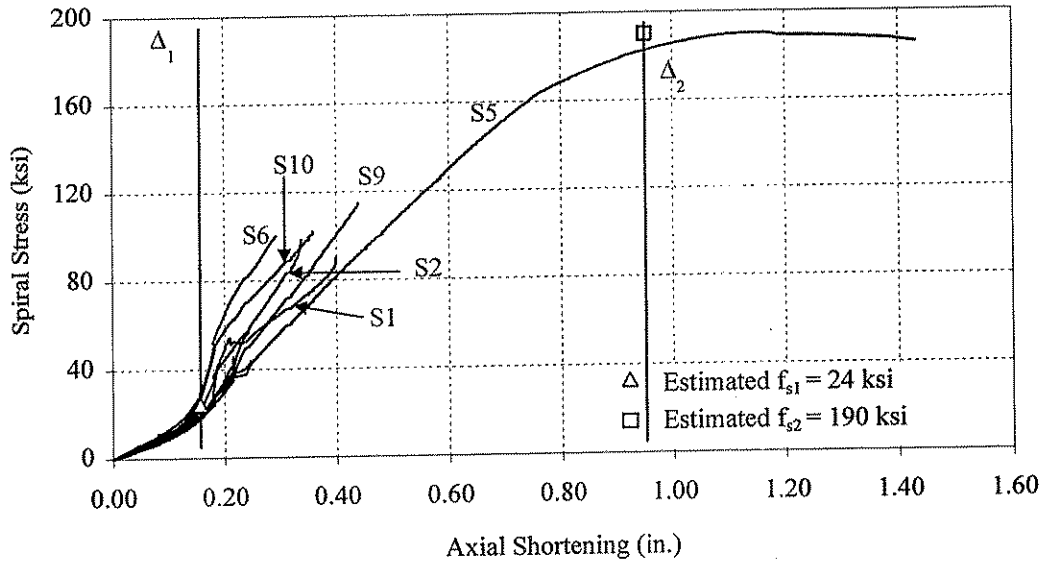

Figure 6.8 Plot of spiral stress versus axial shortening for Specimen 14-F'.

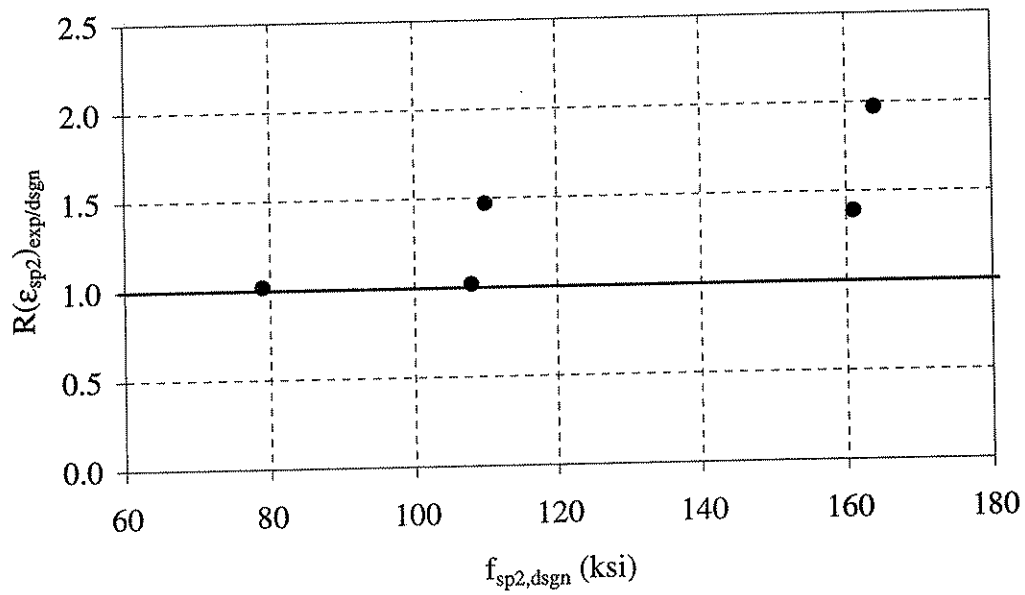

Figure 6.9 Ratio of experimentally determined spiral strain at Δ_2, $\varepsilon_{sp2,exp}$, to the design useable strain, $\varepsilon_{sp2,dsgn}$.

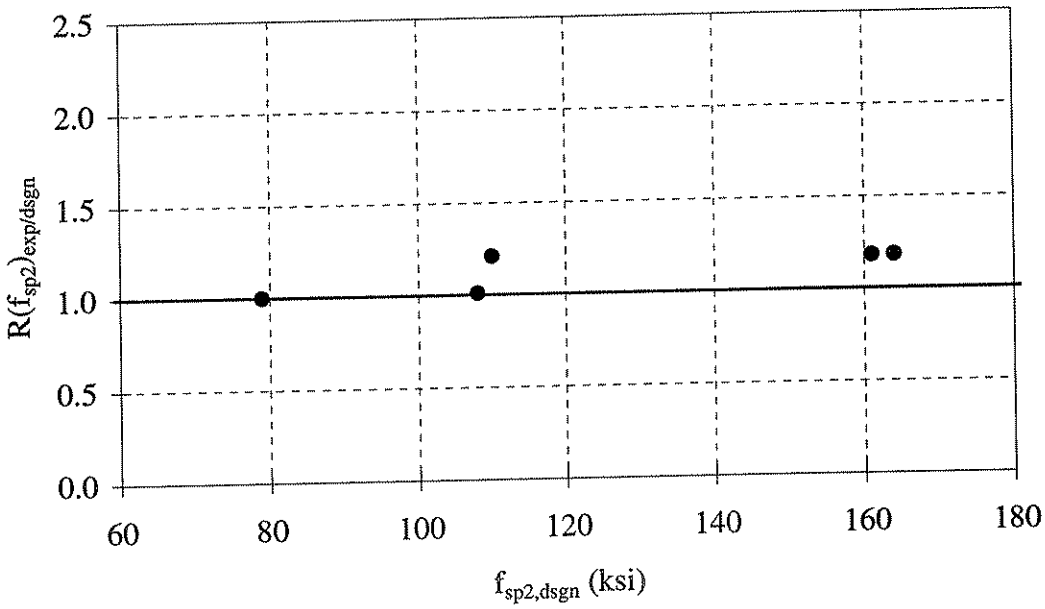

Figure 6.10 Ratio of experimentally determined spiral stress at Δ_2, $f_{sp2,exp}$, to the design useable stress, $f_{sp2,dsgn}$.

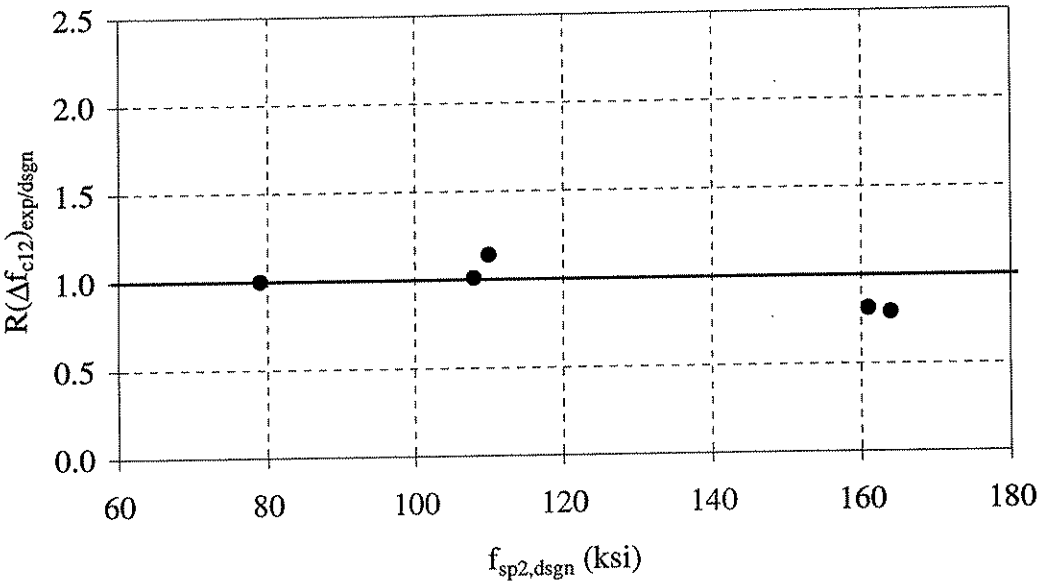

Figure 6.11 Ratio of experimental to design Δf_{c12}.

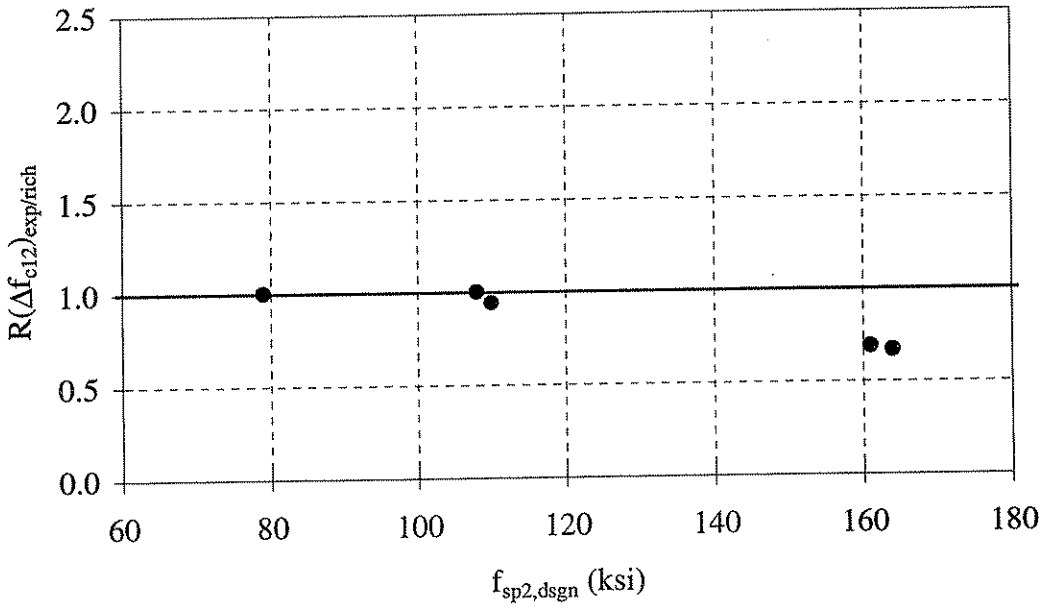

Figure 6.12 Ratio of experimental to Richart et al. Δf_{c12}.

(a)

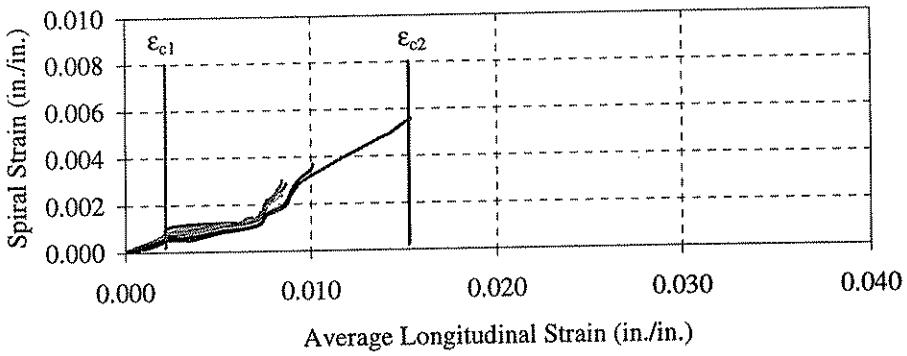

(b)

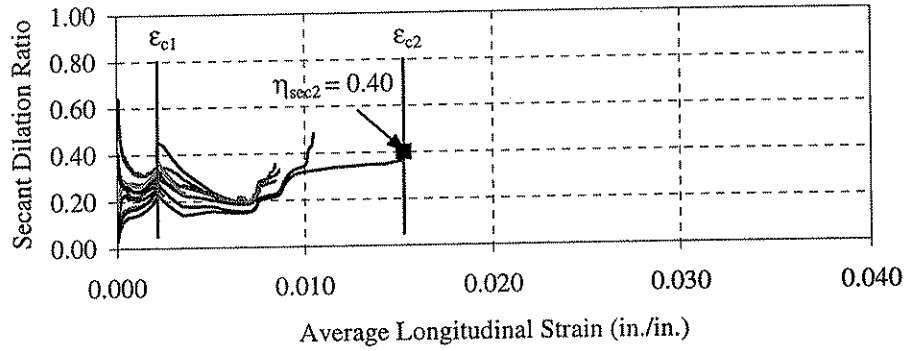

(c)

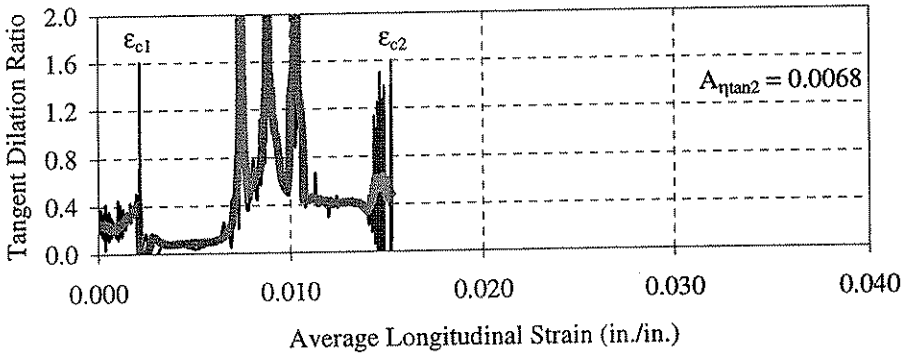

Figure 6.13 Specimen 14-A' experimentally determined dilation ratio parameters: (a) spiral versus longitudinal strain; (b) secant dilation ratio; (c) tangent dilation ratio.

(a)

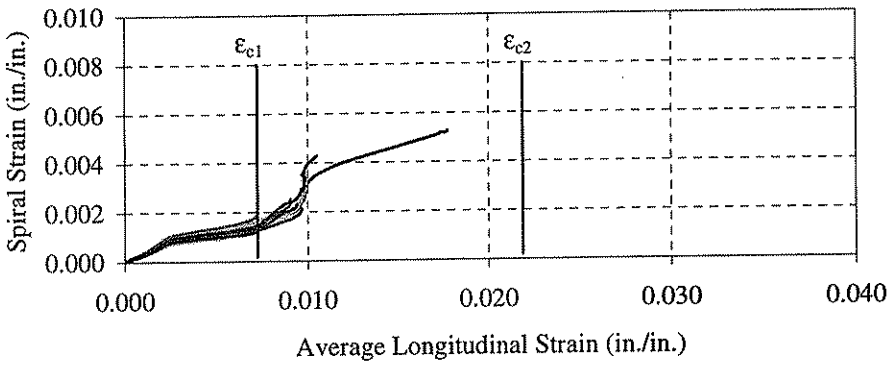

(b)

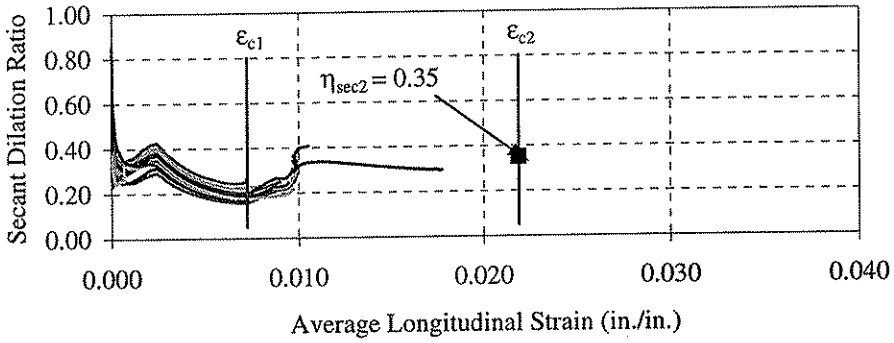

(c)

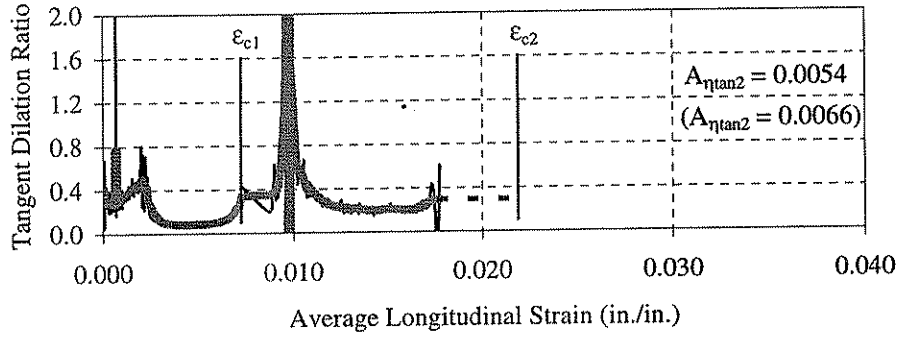

Figure 6.14 Specimen 14-C' experimentally determined dilation ratio parameters: (a) spiral versus longitudinal strain; (b) secant dialtion ratio; (c) tangent dilation ratio.

(a)

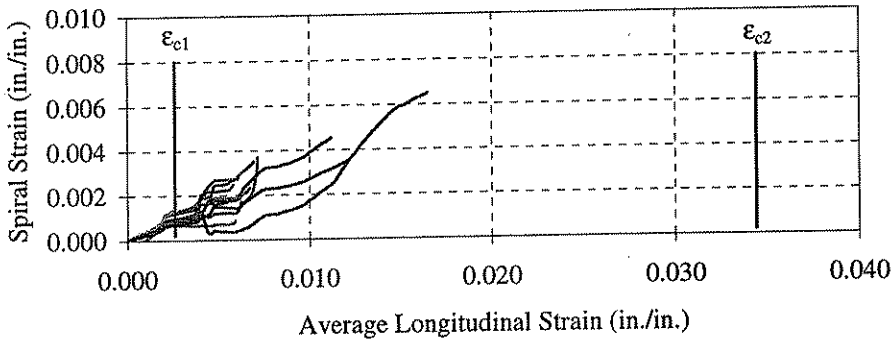

(b)

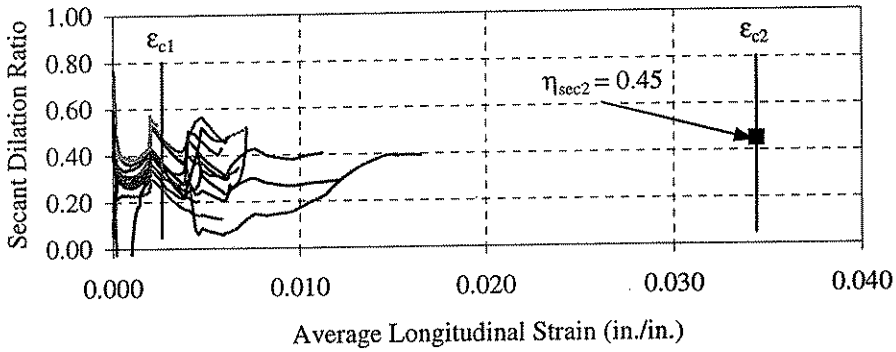

(c)

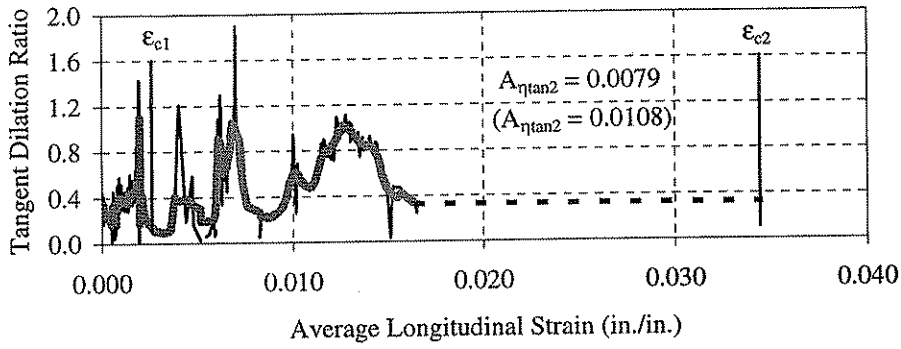

Figure 6.15 Specimen 14-D' experimentally determined dilation ratio parameters: (a) spiral versus longitudinal strain; (b) secant dilation ratio; (c) tangent diation ratio.

(a)

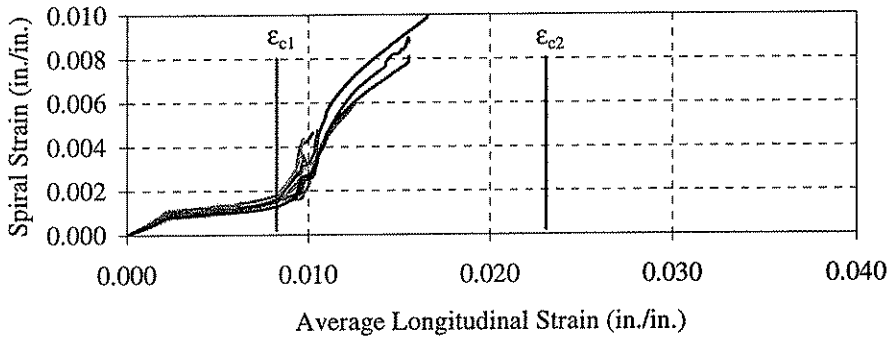

(b)

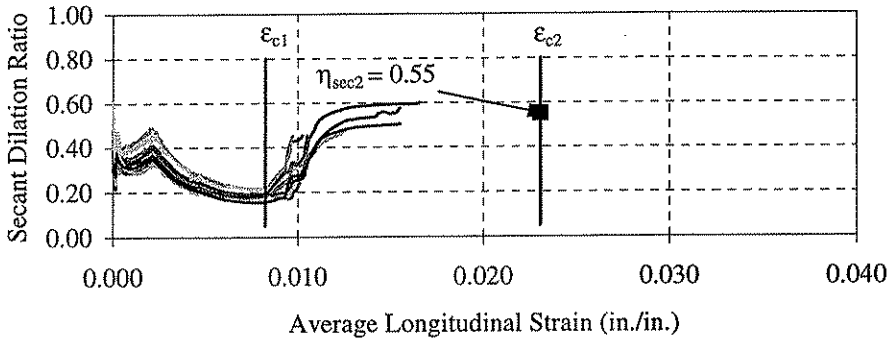

(c)

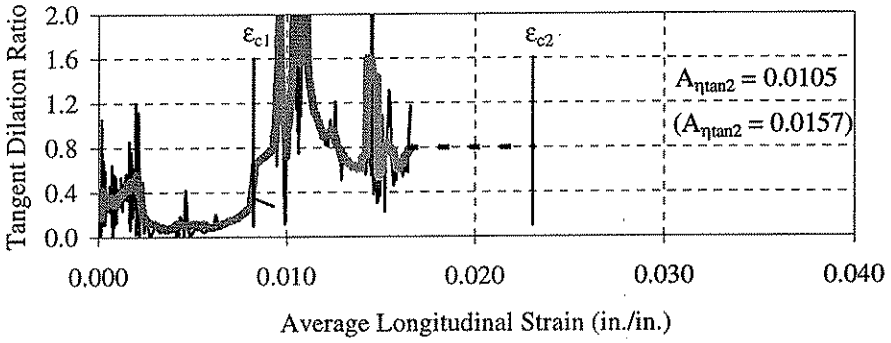

Figure 6.16 Specimen 14-E' experimentally determined dilation ratio parameters: (a) spiral versus longitudinal strain; (b) secant dilation ratio; (c) tangent dilation ratio.

(a)

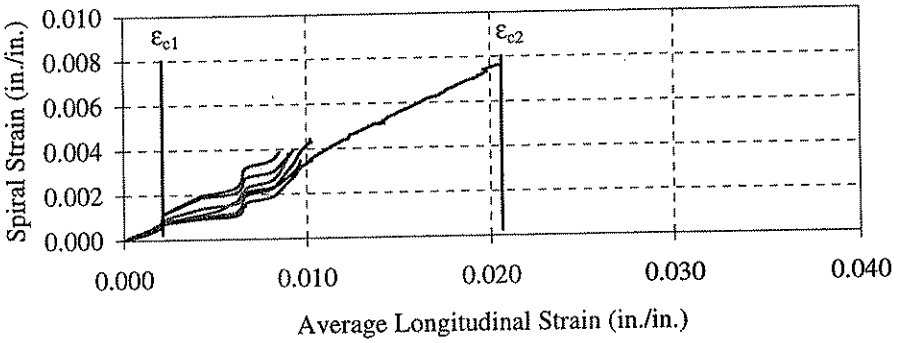

(b)

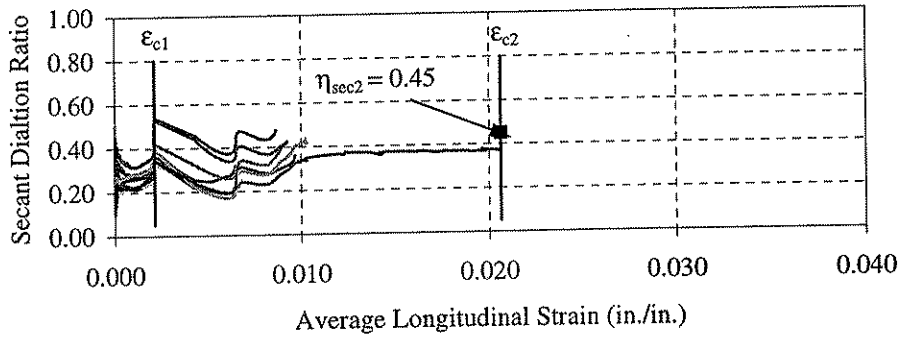

(c)

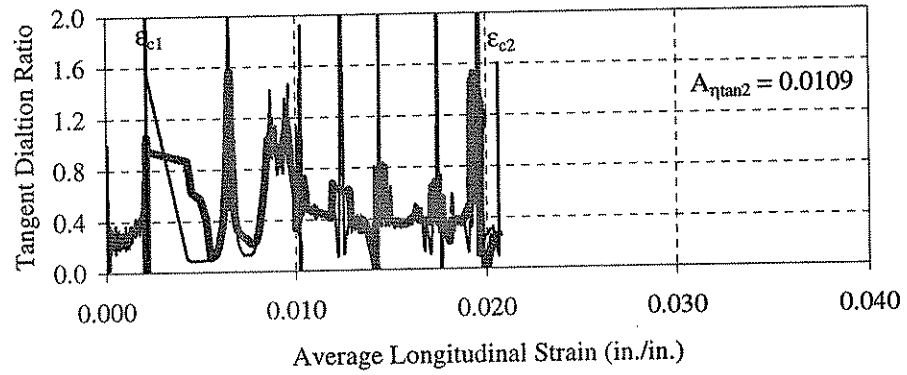

Figure 6.17 Specimen 14-F' experimentally determined dilation ratio parameters: (a) spiral versus longitudinal strain; (b) secant dilation ratio; (c) tangent dilation ratio.

(a)

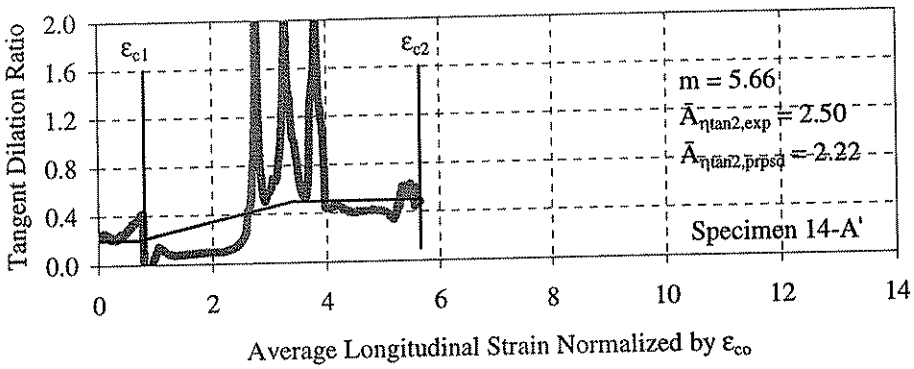

(b)

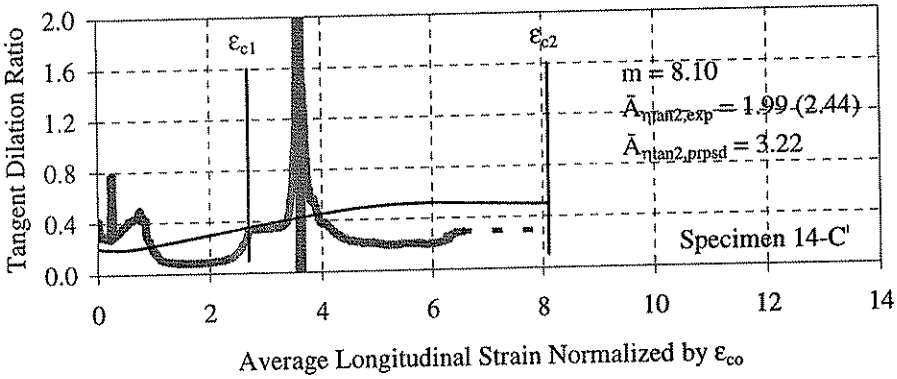

Figure 6.18 Plot of experimental and proposed tangent dilation ratios for (a) Specimen 14-A'; (b) Specimen 14-C'.

(c)

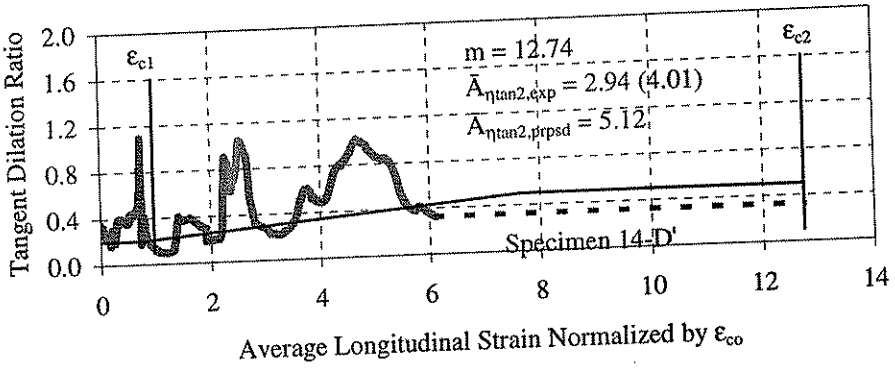

(d)

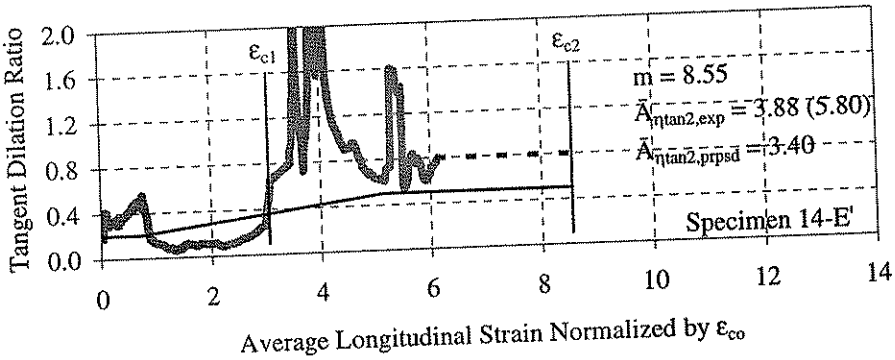

(e)

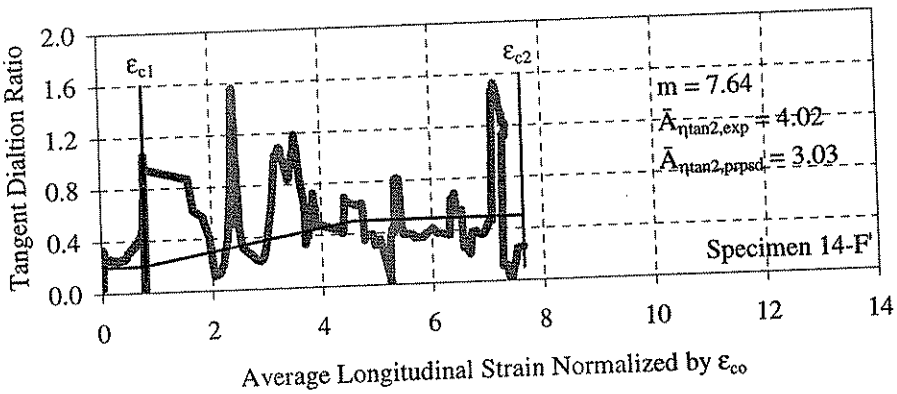

Figure 6.18 (continued) Plot of experimental and proposed tangent dilation ratios for (c) Specimen 14-D'; (d) Specimen 14-E'; (e) Specimen 14-F'.

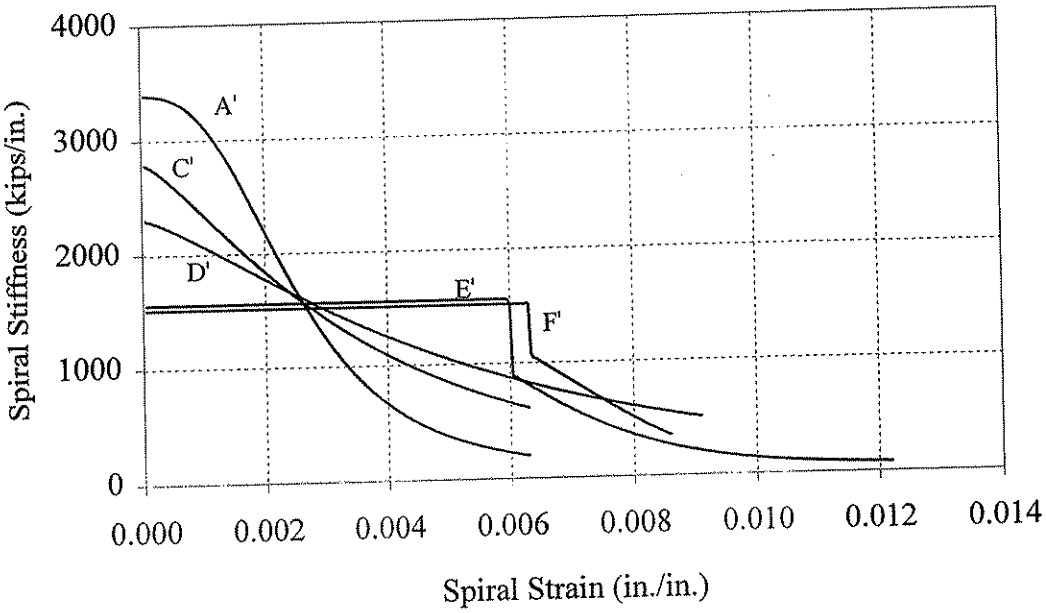

Figure 6.19 Comparison of spiral stiffnesses for each pile.

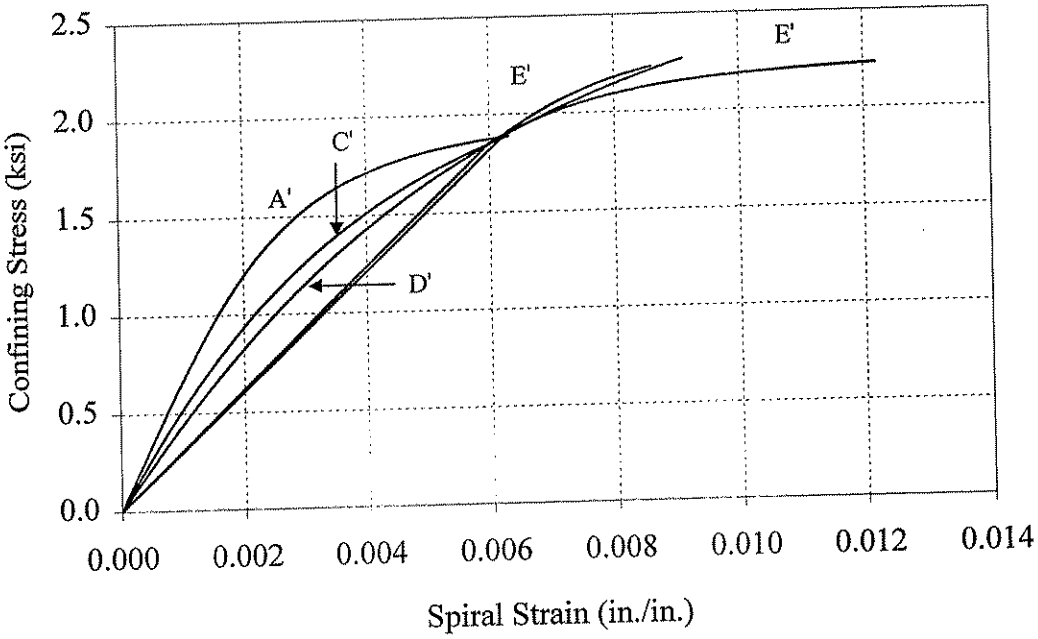

Figure 6.20 Comparison of confining stresses provided in each pile.

CHAPTER 7
CONCLUSIONS AND FUTURE RESEARCH

7.1 INTRODUCTION

This research is a follow-up to the work conducted by Graybeal et al. on the confinement effectiveness of high strength spiral reinforcement in prestressed concrete piles. The primary objective of this research was to evaluate the validity of the design procedure proposed by Graybeal et al. for the design of high strength spiral reinforcement for prestressed concrete piles under concentric axial compression.

This research involved two phases of work. The first phase involved the design and testing of six large-scale high strength spirally reinforced concrete piles in concentric axial compression. The piles were designed according to the procedure developed by Graybeal et al. The second phase of the research focused on a study of the stress-strain properties of the spiral reinforcement. Tension tests were performed on unspiraled specimens of spiral reinforcement in order to determine stress-strain relationships. Then, fiber model analyses were performed to evaluate the effects of spiraling on the tension stress-strain behavior of the spiral reinforcement.

The conclusions of the study are presented below. Following the conclusions, recommendations for future research are presented.

7.2 CONCLUSIONS

The major conclusions based on the research presented in this report are as follows:

1. The design procedure for high strength spiral reinforcement in prestressed concrete piles proposed by Graybeal et al. was found to provide satisfactory spiral designs for the piles made of the steels studied by Graybeal et al. The useable stresses of these steels ranged from 79 ksi (545 MPa) to 110 ksi (758 MPa). The piles made with the two higher strength steels, whose useable stresses were 164 ksi (1131 MPa) and 161 ksi (1110 MPa), did not achieve their design capacities. Therefore, based upon the results of this research, the proposed design procedure can be used for spiral steels with useable stress values up to 110 ksi (758 MPa). This conclusion is applicable to the pile geometries and material strengths treated in this study and the earlier study by Graybeal et al.
2. From the conclusion above, it follows that current code provisions that limit the design yield stress of spiral reinforcement in piles to 60 ksi (414 MPa) are overly conservative. Spiral steel stresses in excess of 60 ksi (414 MPa) can be used to design spiral reinforcement in piles similar to the piles treated in this study and in the earlier study by Graybeal et al.
3. The Richart et al. (1928, 1929, 1934) estimate of longitudinal strain, computed from Equation 2.9, provides reasonable to conservative estimates of longitudinal strain at Δ_2, with the more conservative estimates made for the higher useable stress spirals.

4. The tangent dilation ratio relationship proposed by Graybeal et al. (Equation 2.10) was found to slightly underestimate the value of transverse strain at peak concrete core strength.
5. From Conclusions 3 and 4 it is concluded that the proposed design procedure provides conservative estimates of strains and stresses in the spiral reinforcement at Δ_2, and thus conservative estimates of the confining stress on the core at Δ_2.
6. The equation developed by Richart et al. to predict the increase in concrete core strength due to spiral confinement was found to be valid only for the piles made of spiral steels whose useable stress values did not exceed 110 ksi (758 MPa). The piles made with spiral steels with useable stresses in excess of 110 ksi (758 MPa) did not achieve their desired level of core strength.
7. In general, as the volumetric ratio of spiral reinforcement decreased, the value of confining pressure and the peak concrete core strength decreased.

7.3 FUTURE RESEARCH

The results presented in this report suggest a number of topics for future research:

1. Further research is needed to quantify the effect of the spiraling process on the in-situ tension stress strain behavior of high strength spiral reinforcement. This research is needed because, as a practical matter, only the unspiraled tension stress-strain curve may be available for the design of a given high strength spiral wire. Therefore, there is a need for research to develop a simplified way to predict the in-situ stress-strain curve of the spiraled wire from the unspiraled stress-strain curve and the dimensions of the spiral. A parametric study of the influence of the spiraling process on the in-situ stress-strain curve is therefore needed. The study should include a range of spiral design parameters, including spiral diameter, wire diameter, and unspiraled stress-strain properties. Analytical studies similar to those presented in this report and by Graybeal et al. should be supplemented with tension tests of spiral wire in its unspiraled, spiraled, and spiraled-straightened states to fully explain and quantify the effects of spiraling.
2. Further research is also needed to fully explain the behavior exhibited by Specimens 14-E' and 14-F', where the observed increases in core strength were below the strength increases that were expected for the level of lateral confining pressure that was developed. This future research may focus on the role of spiral stiffness and variable confining pressures throughout the response of a pile on the resulting strength enhancement of the concrete core. In addition to providing a better fundamental understanding of the behavior of spirally-confined concrete, this research is needed if it is desired to obtain even higher useable spiral stresses than those which can be achieved using the Graybeal et al. design procedure.
3. Perhaps as a final demonstration of the validity of the proposed design procedure, axial load tests should be performed on actual precast prestressed concrete piles produced under plant conditions. The tests should include piles with a range of sizes and spiral wire stress-strain characteristics.

REFERENCES

AASHTO, *AASHTO LRFD Bridge Design Specifications*, American Association of State Highway and Transportation Officials, Washington, D.C., First Edition, 1994.

ACI Committee 318, "Building Code Requirements for Structural Concrete (ACI 318-95) and Commentary (ACI 318R-95)," American Concrete Institute, Farmington Hills, MI, 1995.

Cusson, D., and Paultre, P., "Stress-Strain Model for Confined High-Strength Concrete," Journal of Structural Engineering, ASCE, Vol. 121, No. 3, March 1995, pp. 468-477.

Graybeal, B. A., "Confinement Effectiveness of High Strength Spiral Reinforcement in Prestressed Concrete Piles," M. S. Thesis, Department of Civil and Environmental Engineering, Lehigh University, Bethlehem, Pennsylvania, 1997, 228 pp.

Graybeal, B. A., and Pessiki, S. P., "Confinement Effectiveness of High Strength Spiral Reinforcement in Prestressed Concrete Piles," Report No. 98-01, Center for Advanced Technology for Large Structural Systems, April 1998, 164 pp.

Kestner, J. T., "Rehabilitation of Reinforced Concrete Columns Using Fiber Reinforced Polymer Composite Jackets," M. S. Thesis, Department of Civil and Environmental Engineering, Lehigh University, Bethlehem, Pennsylvania, 1997, 232 pp.

MacGregor, J. G., *Reinforced Concrete Mechanics and Design*, Prentice-Hall, Inc., 1992, 848 pp.

Mander, J. B., Priestley, M. J. N., and Park, P., "Theoretical Stress-Strain Model for Confined Concrete," *Journal of Structural Engineering*, ASCE Vol. 114, No. 8, August 1988, pp. 1804-1826.

Martinez, S., Nilson, A. H., and Slate, F. O., "Spirally Reinforced High-Strength Concrete Columns," Journal of the American Concrete Institute, Vol. 81, No. 5, September-October 1984, pp. 431-442.

Nilson, A. N., and Winter, G., *Design of Concrete Structures*, Eleventh Edition, McGraw-Hill, Inc., 1991, 904 pp.

PCI Design Handbook - Precast and Prestressed Concrete, Fourth Edition, Precast/Prestressed Concrete Institute, Chicago, IL, 1992.

Prakash, V., Powell, G., and Campbell, S., "DRAIN-2DX Base Program Description and User Guide; Version 1.10," Report No. UCB/SEMM-93/17&18, Structural Engineering Mechanics and Materials, Department of Civil Engineering, University of California, Berkeley, CA, December 1993.

Richart, F. E., Brandzaeg, A., and Brown, R. L., "A Study of the Failure of Concrete Under Combined Compressive Stresses," University of Illinois Bulletin, Vol. XXVI, No. 12, Nov. 20, 1928, 104 pp.

Richart, F. E., Brandzaeg, A., and Brown, R. L., "The Failure of Plain and Spirally Reinforced Concrete in Compression," University of Illinois Bulletin, Vol. XXVI, No. 31, April 2, 1929, 74 pp.

Richart, F. E., and Brown, R. L., "An Investigation of Reinforced Concrete Columns," University of Illinois Bulletin, Vol. XXVI, No. 40, June 5, 1934, 94 pp.